Stellingen

behorende bij het proefschrift
Transport of interacting electrons in mesoscopic systems
van T. H. Stoof

---

1. De elektrostatische potentiaalverdeling in een diffuse Aharonov-Bohmring die in contact staat met een supergeleider, is een periodieke funktie van de flux door de ring met periode $h/2e$.

   This thesis, Chapter 7.

2. De formule die door Van der Vaart *et al.* wordt gebruikt om hun experimentele data te fitten is onjuist, maar de fout in de fitparameters is in de beschouwde limiet verwaarloosbaar klein.

   N. C. van der Vaart et al., Phys. Rev. Lett. 74, 4702 (1995).

3. Het is waarschijnlijker dat de halve-fluxquantumperiodiciteit in de magnetoweerstand van ladingsdichtheidsgolven met zuilvormige defecten haar oorsprong vindt in ensemblemiddeling dan in macroscopische quantumtunneling.

   M. I. Visscher and B. Rejaei, submitted to Phys. Rev. Lett.

4. Uit numerieke berekeningen volgen sterke aanwijzingen voor het universele karakter van de overgang van moleculair-veld gedrag naar Ising kritiek gedrag bij nadering van het kritieke punt.

   E. Luijten et al., Phys. Rev. Lett. 79, 561 (1997).

5. Het is onwaarschijnlijk dat er ooit een deeltjesversneller zal worden gebouwd die enige afwijking van het standaardmodel te zien zal geven.

6. In de recente literatuur wordt de inhomogeniteit van Bose-Einstein gecondenseerde gassen veel te sterk benadrukt, gezien het feit dat atomair ^{7}Li het enige systeem is waarin zij een wezenlijke rol speelt.

7. Gezien het belang voor een kind om "gewenst" te zijn en gelet op de strenge eisen die aan adoptieouders worden gesteld, verdient het aanbeveling ook homosexuele paren voor adoptie van kinderen in aanmerking te laten komen.

8. Het grootste bezwaar tegen het creationisme als wetenschappelijke theorie voor het ontstaan van de aarde; namelijk dat ze niet falsifieerbaar is, wordt niet weggenomen door een visje op de achterkant van je auto te plakken.

9. Een voordracht op een werkbesprekingsbijeenkomst is meer geschikt om te testen of een student zijn theorievakken begrepen heeft dan een tentamen.

10. Het recente besluit van het College van Dekanen om universitaire docenten zonder enige vorm van kwaliteitsoverwegingen uit te sluiten voor de positie van toegevoegd promotor, druist niet alleen in tegen de hedendaagse tijdsgeest, maar getuigt tevens van onbegrip inzake de rol van universitaire docenten bij het begeleiden van promovendi.

# Transport of interacting electrons in mesoscopic systems

Transport of interacting electrons in mesoscopic systems

PROEFSCHRIFT

ter verkrijging van de graad van doctor
aan de Technische Universiteit Delft,
op gezag van de Rector Magnificus, Prof. dr. ir. J. Blaauwendraad,
in het openbaar te verdedigen ten overstaan van een commissie,
door het College van Dekanen aangewezen,
op dinsdag 2 september 1997 te 16.00 uur
door

Theodorus Henricus STOOF

natuurkundig ingenieur,
geboren te Eindhoven
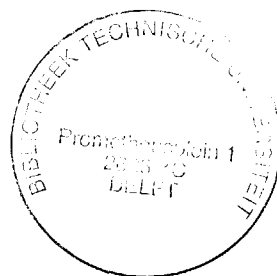
Dit proefschrift is goedgekeurd door de promotor:

Prof. dr. ir. G. E. W. Bauer

Samenstelling promotiecommissie:

Rector Magnificus, voorzitter
Prof. dr. ir. G. E. W. Bauer, Technische Universiteit Delft, promotor
Prof. dr. ir. J. E. Mooij, Technische Universiteit Delft
Prof. dr. C. W. J. Beenakker, Rijksuniversiteit Leiden
Prof. dr. ir. T. M. Klapwijk, Rijksuniversiteit Groningen
Prof. dr. V. T. Petrashov, Holloway University London
Dr. ir. H. T. C. Stoof, Universiteit Utrecht
Dr. Yu. V. Nazarov, Technische Universiteit Delft
Prof. dr. ir. J. J. J. Kokkedee, Technische Universiteit Delft

Dr. Yu. V. Nazarov heeft als begeleider in belangrijke mate aan de totstandkoming van dit proefschrift bijgedragen.

It is a profound and necessary truth that the deep things in science are not found because they are useful; they are found because it was possible to find them.

Robert Oppenheimer

PREFACE

This thesis contains an account of my scientific activities in the Theoretical Physics group of the Department of Physics at Delft University of Technology, in the period between September 1993 and July 1997. It consists of a number of theoretical studies in *mesoscopic physics*. This name refers to the size of the systems that are studied, which is somewhere between microscopically small and macroscopically large.

Practically everything we experience in our everyday lives is governed by macroscopic or classical physics. One example is the force of gravitation, which keeps us attached to the face of the earth and which rules the motion of stellar bodies. This force is described by Newton's theory of gravitation and Einstein's theory of relativity. Other important examples are the electric and magnetic forces. They govern the behavior of voltages and currents in electrical circuits and are responsible for the electromagnetic waves needed for TV sets and microwave ovens. These phenomena are described by Maxwell's theory of electromagnetism. The macroscopic length scales on which these forces play a role vary from fractions of millimeters to billions of light years.

Microscopic physics describes such processes as radioactive decay, nuclear fusion and fission, and the interaction of matter and light. Here, the relevant length scale is the atomic length scale, which is ten times smaller than a nanometer. On these extremely small length scales, a radically different theory is needed to describe physical phenomena correctly. This theory is known as *Quantum Mechanics*, and it is unlike anything we are accustomed to in the macroscopic world. Its basic feature is the absence of the strict distinction between particles and waves. As a result, electrons or light are neither particles nor waves, but sometimes behave like the former while under different conditions they behave like the latter. A consequence of this dual nature is that an electron can interfere like light and that it can "jump" (or *tunnel*, as it is called) through barriers.

Systems with intermediate sizes, roughly between ten nanometers and ten micrometers, can show both classical and quantum mechanical behavior, depending on the circumstances. This is the domain of mesoscopic physics. Because in this case the electron wave length is comparable to the system size, it is possible to constrain the electron motion in a certain direction. In this direction, the electron state then corresponds to a standing wave. When electrons are confined to a thin slab, their motion is restricted to the two-dimensional (2D) plane of the slab, which is known as a *two-dimensional electron gas*. Analogously they can also be confined to a narrow pillar, resulting in one-dimensional (1D) motion along the length of the pillar, which is called a *quantum wire*. It is even possible to remove all of the electron's degrees of freedom by putting it in a tiny box called a *quantum dot*. The electron is then in what is called a zero-dimensional (0D) state.

The development of mesoscopic physics in the past fifteen years has been stimulated to a large extent by rapid advances in the miniaturization and fabrication techniques of electronic circuits. These improvements have enabled the realization of superior model systems for studying the physics of few-electron systems in low dimensions. A striking

example is the abovementioned quantum dot, which is essentially a puddle of electrons kept together by some external force. In this and many other respects a quantum dot can thus be seen as an *artificial atom*, the properties of which can be studied in a controlled way. Another example is a structure, with a typical size of a few micrometers, in which normal metal wires are connected to one or more pieces of superconducting metal. Although the normal metal wires do not become superonducting themselves, the electrons in the wires "sense" the presence of the superconductors. This *proximity effect* causes a change in the resistance of the wires, which can be measured accurately.

Besides being of fundamental interest, mesoscopic physics is also relevant for the development of new electronic devices. Several applications have already been realized, like an extremely sensitive electrometer known as a *single-electron tunneling transistor* and a device to transfer electrons one by one called a *single-electron turnstile*. In the future, devices like these will enable sophisticated electronic circuits that may be used for e.g. advanced telecommunication systems. Another interesting possibility is a *quantum bit* or *qubit* stored by solid state devices. Contrary to an ordinary bit, which is either zero or one, a qubit can, roughly speaking, be both at the same time. Qubits open the way for faster computer algorithms and may ultimately lead to *quantum computing* in the distant future.

All these concepts above will come back in the body this thesis, which can crudely be divided in two parts. The first part, consisting of chapters 2, 3, and 4, deals with electron transport in semiconductor nanostructures like quantum dots and wires. The second part, chapters 5, 6, and 7, concerns the electronic properties of small hybrid normal metal-superconducting devices.

Because electrons all have the same negative charge, they repel each other. This repulsion is known as *electron-electron interaction*. In chapter 2 we investigate how the interaction influences the electronic properties of quantum wires and dots that are placed in a high magnetic field. In the remainder of the first part we examine electron transport through a system in which two quantum dots are placed in line. For a current to flow, an electron has to tunnel onto the first dot, then tunnel to the second one, and finally leave the system again. When the system is irradiated with electromagnetic waves, the electrons can interact with light particles or *photons*. A photon can help an electron to tunnel through a barrier by giving the electron its energy, which is called *photon-assisted tunneling*. In chapters 3 and 4 we investigate how photon-assisted tunneling modifies the current through double-dot systems.

As mentioned above, the behavior of electrons in a piece of normal metal is influenced by the proximity of a superconductor, which has a characteristic property called the *macroscopic phase*. The resistance of the normal metal with two superconducting contacts depends on the *macroscopic phase difference* between the two superconductors. In chapters 5 and 6 we calculate how the resistance of the normal metal depends on this phase difference and on the temperature. We also consider the influence of electron-electron interaction in the normal metal on the resistance. In chapter 7, we examine the effect of a small magnetic field on the resistance of structures that contain closed loops, called *Aharonov-Bohm rings*.

Throughout the years, I noticed that most nonscientists I encountered (and even some experimentalists!) were under the impression that doing theoretical physics is a rather solitary occupation, preferably performed in some far-away place. The reality is different, however. Theoreticians are actually much like ordinary people and contrary to common wisdom, they can even be quite sociable. Speaking for myself, I could not have done the

work presented here without the collaboration, support or even mere presence of quite a few people.

First of all, I would like to thank my promotor and collaborator; Gerrit Bauer. With characteristic enthusiasm and good humor he taught me a lot more than just physics (refereeing dull articles he did not find interesting himself and which new computer games are cool, to name but a few). He is the only person I know who has to play computer games under the guise of entertaining foreign guests and I hope his wife will never find out. Thanks a lot, Gerrit. Working with you has been a great pleasure.

Secondly, my thank goes out to my other teacher and collaborator; Yuli Nazarov, a.k.a "The Oracle of Delft". He sometimes entertains guests by letting them watch him play *Civilization II* the entire afternoon and he has the habit of leaving somewhere in the middle of a talk to have a smoke. This latter behavior was, however, at times not unwelcome as many students with ill-prepared presentations can attest. Although he was disgracefully deprived of the right to be"toegevoegd promotor", I nevertheless consider myself very privileged to have been his student. Spasiba, Yuli.

I am also grateful to the other group members for creating an excellent working environment. Most importantly, I would like to mention the two other members of the first generation "Bauer Boys", Kees Schep and in particular Mark Visscher, who introduced me to student life in Delft and who succeeded in completely removing my initial distrust of "Corpsballen" (well almost completely, at least). I vividly recall our many nightly sessions in the bars of respectively Delft and The Hague, where we discussed physics, life, and his girlfriend. I sincerely hope there will be many more, or, in my native tongue: "Da we d'r nog moar veul maggû vattû!"

Other (ex) group members that I would like to thank include Titus Tielens, Lex Rijkels, Jeroen Struben, Uli Geigenmüller, Sasha Khaetskii, Sasha Dzyubenko, Arkadi Odintsov, Behzad Rejaei, Masahiko Hayashi, Maarten Wegewijs (cartoon genius and *Maple* maniac), Erik Luijten (the local LATEXwizard, whose direct remarks during coffee breaks were always highly amusing, in particular because he was usually the only one taking them seriously), Jaap Kokkedee, Rini Renne, Henk Blöte, Kok Bruin, and last but not least Yvonne Zwang, who has been holder of the title "World's Best Secretary" for at least five consecutive years now. It will definitely not be easy to leave such an interesting and pleasant group of people.

I would also like to mention a few experimentalists here: Luuk Mur, with whom I had many lively discussions on Friday afternoons. I look forward to remaining his colleague. Another TeePeeKaffee hero is Sander "Nanobuisje" Tans, whose integrity and good wits I like. I also had many interesting discussions with Tjerk Oosterkamp, who changes diamonds into fish, and Leo Kouwenhoven, who makes conferences more lively by, among other things, initiating psychological question rounds at two in the morning.

Of course I would also like to thank my parents here for their continued support throughout the years. Furthermore my sister Winy, who applied for the job of "paranymph" three years ago to make sure she'd be the first, and naturally my brother Henk: We continue to get on people's nerves with our endless conversations about either music or physics. I also want to thank him for carefully reading the manuscript. Finally, I want to mention the many friends I made over the years. Their contributions are hidden, but nevertheless very important.

Until now, I have not mentioned the most important person in my life; Heli Penz. At times, she nearly drove me insane by asking me questions like "When is your thesis go-

ing to be finished?", "When is your promotion date?", and "Can I read your preface?" at least three times a day. But then again, it most be hard living with a mad scientist, particularly around the time he's writing his thesis. The truth is that I'm very happy and proud to have her and I want to thank her for her endless support. Heli, I hope we will stay together for a long time and that your taste for cars will remain at its current level.

Delft, July 1997   Theo Stoof

CONTENTS

1

INTRODUCTION

Mesoscopic physics entails the study of systems with typical sizes of somewhere between 10 nm and 10 μm. Because the Fermi wave length of electrons in mesoscopic structures can be 10 nm, i.e. of the order of the sample size, the system's behavior is often determined by a mixture of classical and quantum physics. In the last fifteen years, technological advances have enabled the fabrication of structures in this regime, thus opening the way for the fabrication of electronical devices like the single-electron tunneling transistor and the single-electron turnstile. More interesting from a fundamental point of view, however, is the possibility of constructing test systems for studying few-electron physics in a controlled manner. Examples of model systems in which mesoscopic effects are intensely studied both experimentally and theoretically, are quantum wires and dots, quantum Hall devices, normal metal-superconductor hybrid structures, magnetic multilayer heterostructures, and more recently also charge density wave systems and carbon nanotubes. The electronic properties of mesoscopic systems are usually investigated by means of a transport experiment, i.e. by measuring the current through a sample.

In this introductory chapter we summarize the miscellaneous aspects of electron transport that are relevant for the research presented in this thesis. We start by discussing electronic properties of semiconductor devices like quantum wires and dots in a strong magnetic field, concentrating on the effects of electron-electron interaction in the integer quantum Hall regime. We then proceed to show how resonant tunneling of electrons is affected by interaction with photons. As a model system we use a double quantum dot, where photon-assisted tunneling occurs between discrete states. The final part of this chapter deals with hybrid normal metal-superconducting devices known as Andreev interferometers. We review the nonequilibrium Green function formalism used to describe diffusive transport in superconductors and introduce an application of this theory to electrical circuits containing superconducting elements.

1.1 EDGE CHANNELS IN THE INTEGER QUANTUM HALL REGIME

Since the Nobel prize winning discovery of the integer quantum Hall effect (IQHE) by Klitzing, Dorda, and Pepper in 1980 [1] and the subsequent discovery of the fractional quantum Hall effect (FQHE) by Tsui, Störmer, and Gossard in 1982 [2], the two-dimensional electron gas (2DEG) in a magnetic field is one of the most investigated topics in the field of condensed matter physics.

In the quantum Hall regime the applied magnetic field is so strong that the mixing of Landau levels by either disorder or electron-electron interactions can be considered a weak perturbation. It is then possible to discern two different limits in the physics of the quantum Hall effect. In the integer quantum Hall regime several Landau levels are filled and gaps in the energy spectrum are formed due to the quantization of kinetic energy caused by the applied magnetic field. In the fractional quantum Hall regime, only the lowest Landau level is partially occupied and gaps in the energy spectrum are present because of electron-electron interaction effects.

It is beyond the scope of this thesis to give an overview of the phenomena in these two regimes. There are a number of good books and review articles on this subject [3, 4, 5, 6, 7] to which we refer the interested reader. Henceforth, we will only address those features of the *integer* quantum Hall regime that are relevant for the research presented in chapter 2.

1.1.1 THE TWO-DIMENSIONAL ELECTRON GAS

The most common experimental realization of the so-called two-dimensional electron gas is composed of the semiconductor materials GaAs and $Al_xGa_{1-x}As$. Fig. 1.1 shows a schematic layout of such a heterostructure, which consists of a nominally doped GaAs layer and a silicon doped (n-type) $Al_xGa_{1-x}As$ layer. The mobile electrons in the conduction band of the latter layer migrate to states near the bottom of the conduction band in the GaAs layer. The positive charge of the donor ions attract the electrons to the interface and bends the energy bands. This process continues until the Fermi level is constant throughout the different layers. An inversion layer of electrons is formed, with the top of the valence band above the bottom of the conduction band.

The result is a nearly triangular potential well, which traps the electrons near the interface of the GaAs-$Al_xGa_{1-x}As$ heterostructure. The motion of these electrons is confined to the plane parallel to this interface. In order to increase the mobility of the 2DEG formed in this way, a spacer layer of undoped $Al_xGa_{1-x}As$ is grown between the GaAs and Si-doped $Al_xGa_{1-x}As$ layers. This layer reduces the scattering between the electrons and their parent donors. Finally, the entire structure is capped with another GaAs layer to prevent the $Al_xGa_{1-x}As$ layer from oxidizing. Although the motion of electrons in the 2DEG is restricted to two dimensions, the electron wave functions have a finite extent in the direction perpendicular to the plane of motion. As a result, electron-electron interaction in a 2DEG is in reality not strictly two dimensional. This effect can be taken into account theoretically by a so-called form factor. This does not change the essential physics but causes significant quantitative modifications. In chapter 2 we will use a form factor to compare our calculations with experiments but in the remainder of this introduction we will ignore this deviation.
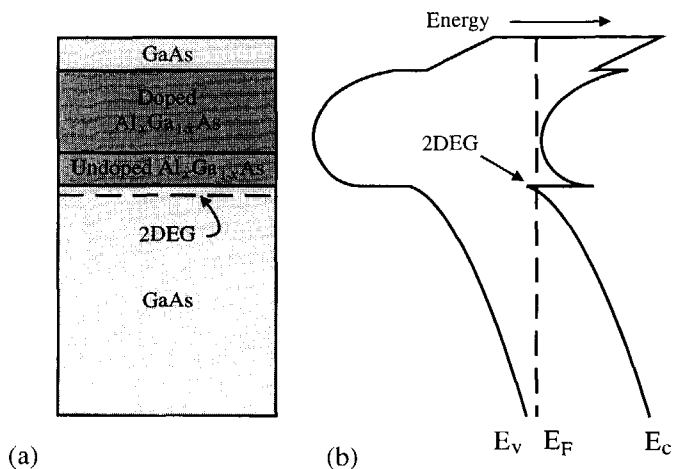
Figure 1.1: *(a) Schematic layout of a GaAs-$Al_xGa_{1-x}As$ heterostructure in which a 2DEG is formed. (b) Corresponding energy diagram. E_v, E_c, and E_F denote the top of the valence band, the bottom of the conductance band, and the Fermi level, respectively.*

1.1.2 THE HOMOGENEOUS TWO-DIMENSIONAL ELECTRON GAS IN A MAGNETIC FIELD

Consider an unbounded, non-interacting two-dimensional electron gas subject to a magnetic field that is applied in the z-direction, perpendicular to the xy-plane of the 2DEG, $\mathbf{B} = (0, 0, B_0)$. The system is depicted schematically in Fig. 1.2. Due to the presence of the magnetic field, the kinetic energy of the electrons is quantized into so called Landau levels [8].

To see how this comes about, we will for the moment neglect the small Zeeman energy term, $\varepsilon_Z^\sigma = \sigma g \mu_B B_0$. The Hamiltonian of the system then becomes:

$$\mathcal{H} = \frac{1}{2m} \left(i\hbar \nabla + e\mathbf{A} \right)^2, \tag{1.1}$$

where m is the electron mass and the vector potential $\mathbf{A}$, with $\mathbf{B} = \nabla \times \mathbf{A}$. The vector potential is not unique because any gauge transformation $\mathbf{A} \to \mathbf{A} + \nabla \phi$ leaves the magnetic field invariant. Convenient choices for $\mathbf{A}$ are the Landau gauge, $\mathbf{A} = (0, B_0 x, 0)$, for systems with periodic boundary conditions in the y-direction, and the symmetric gauge, $\mathbf{A} = (-B_0 y/2, B_0 x/2, 0)$, for systems possessing circular symmetry.

We consider a 2DEG with length L and periodic boundary conditions in the y-direction. If we adopt the Landau gauge, the Schrödinger equation becomes:

$$-\frac{\hbar^2}{2m} \left[\frac{\partial^2}{\partial x^2} - \left(i\frac{\partial}{\partial y} + \frac{eB_0}{\hbar} \right)^2 \right] \psi_i(x, y) = \varepsilon_i \psi_i(x, y). \tag{1.2}$$

Because of the periodic boundary conditions, the wave functions can be written as $\psi_i(x, y) =$
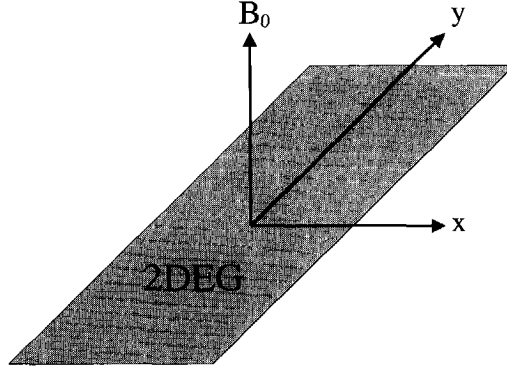
Figure 1.2: *Schematic picture of the 2DEG in a uniform magnetic field.*

$\frac{1}{\sqrt{L}}e^{-iky}\phi_i(x)$, where $k = n\frac{2\pi}{L}$. The equation for $\phi_i(x)$ now becomes:

$$\left[-\frac{\hbar^2}{2m}\frac{\partial^2}{\partial x^2} + \frac{1}{2}m\omega_c^2\left(x - x_0\right)^2\right]\phi_i(x) = \varepsilon_i\phi_i(x), \tag{1.3}$$

where we have introduced the cyclotron frequency $\omega_c = \frac{eB_0}{m}$ and $x_0 = kl_B^2$, where $l_B = \sqrt{\frac{\hbar}{eB_0}}$ is the magnetic length. Eq. (1.3) is the equation for a harmonic oscillator with a shifted equilibrium position x_0. The eigenfunctions $\phi_N(x - x_0)$ of Eq. (1.3) are the harmonic oscillator wave functions:

$$\phi_N(x) = \frac{1}{(2^N N!\sqrt{\pi}l_B)^{\frac{1}{2}}}e^{-\frac{1}{2}(\frac{x}{l_B})^2}H_N(x), \tag{1.4}$$

where $H_N(x)$ are Hermite polynomials and N is the Landau level index. The Landau level wave functions are thus plane waves in the y-direction and harmonic oscillator solutions in the x-direction and have energies

$$\varepsilon_N = \left(N + \frac{1}{2}\right)\hbar\omega_c. \tag{1.5}$$

The Landau levels are highly degenerate because the energy does not depend on the wave number k, or equivalently, on the position x_0. Let the 2DEG be confined to a width W in the x-direction. It then follows that $0 < k < W/l_B^2$. Together with the restriction on the allowed values for the wave number, $k = n\frac{2\pi}{L}$, where n is an integer, we find that the total number of states in the area WL is $\frac{WL}{2\pi l_B^2}$. The number of electron states per unit area in a Landau level is thus given by:

$$n_0 = \frac{1}{2\pi l_B^2}, \tag{1.6}$$

which is proportional to the applied magnetic field. It is convenient to introduce the filling factor ν which is the ratio of the total number of occupied states and the number of states

in a single Landau level:

$$\nu = \frac{n}{n_0}, \tag{1.7}$$

where n is the electron sheet density. If we include spin into the description, the Landau level energies become:

$$\varepsilon_N^\sigma = \left(N + \frac{1}{2}\right)\hbar\omega_c + \sigma g\mu_B B_0, \tag{1.8}$$

where $\sigma = \pm\frac{1}{2}$, depending on the spin of the electron. The number of electrons that can occupy a Landau level is then doubled and each filled Landau level contributes a term of 2 to the filling factor. Although the energy splitting ε_Z between two spin split levels and $\hbar\omega_c$ between two Landau levels are both proportional to B, the former splitting is typically much smaller than the latter ($g = -0.44$ in GaAs).

Semiclassically, electrons rotate in a cyclotron orbit around a "guiding center" x_0. The minimum distance between guiding centers in x-direction is $\Delta x = \frac{2\pi l_B^2}{L}$. For large system sizes the wave number k and the guiding center position x_0 are quasi continuous. We will make use of this property in chapter 2.

1.1.3 CONFINEMENT AND EDGE CHANNELS

A real sample of a heterostructure containing a 2DEG has a finite size. One of the possible ways to define a certain sample lay-out is etching. Using this technique, the conducting structure can be molded into any desired shape. Alternatively, metallic gates can be fabricated on top of the heterostructure, thus avoiding the damage done by etching. By applying a negative voltage to these gates, the electron gas below is depleted and it is possible to deform the conducting region in a controlled way. By tuning the voltage on the gates one can alter the height of the barriers confining the 2DEG. Descriptions of various confinement techniques can be found in e.g. Refs. [9, 10, 11]. In magnetic fields the sample edges have interesting consequences on the electronic structure. We will first discuss them in the non-interacting, single-particle picture of the previous section.

To take into account the finite extent of the sample an external confinement potential is added to the Hamiltonian (1.1). In principle, this potential can have any shape, but commonly used forms are the square-well potential:

$$V_c(x) = \begin{cases} 0 & |x| < W/2, \\ V_0 & |x| \geq W/2, \end{cases} \tag{1.9}$$

and the parabolic potential:

$$V_c(x) = \frac{1}{2}m\omega_0^2 x^2. \tag{1.10}$$

We prefer the latter here because it gives a more realistic description of the external potential of a quantum wire. By focusing on energies close to the Fermi energy, this potential can also be used for a description of edges in wide samples. Moreover, the problem of a

non-interacting 2DEG in a magnetic field confined by a parabolic potential can be solved analytically. The Hamiltonian for a state with wave number k in the y-direction is:

$$\mathcal{H} = -\frac{\hbar^2}{2m}\frac{\partial^2}{\partial x^2} + \frac{1}{2}m\omega_c^2\left(x - x_0\right)^2 + \frac{1}{2}m\omega_0^2 x^2, \tag{1.11}$$

which can be rewritten as:

$$\mathcal{H} = -\frac{\hbar^2}{2m}\frac{\partial^2}{\partial x^2} + \frac{1}{2}m\omega^2\left(x - \overline{x}_0\right)^2 + \frac{\hbar^2 k^2}{2M}. \tag{1.12}$$

The first two terms of Eq. (1.12) describe the motion in the x-direction, which is again that of a shifted harmonic oscillator but now with hybrid frequency

$$\omega = \sqrt{\omega_c^2 + \omega_0^2}, \tag{1.13}$$

and center coordinate

$$\overline{x}_0 = x_0 \frac{\omega_c^2}{\omega^2}. \tag{1.14}$$

The third term describes free motion in the y-direction with an effective mass

$$M = m\frac{\omega^2}{\omega_0^2}. \tag{1.15}$$

Eq. (1.14) can be used to define an effective magnetic length:

$$\overline{l}_B = l_B \frac{\omega_c}{\omega}. \tag{1.16}$$

This solution clearly displays the correct behavior in the two limiting cases of zero and large magnetic field. If $B = 0$ then $\omega = \omega_0$, $\overline{x}_0 = 0$, and $M = m$ so that we recover the motion of an electron in an external parabolic potential. In the case of large magnetic field the third term in Eq. (1.12) vanishes, $\omega \to \omega_c$, and $\overline{x}_0 \to x_0$ and hence the Landau level structure is regained.

The external confinement thus removes the degeneracy of the Landau levels because the energy in this case depends on the momentum $\hbar k$. The system now exhibits 1D subbands with energy dispersion:

$$E_N(k) = \left(N + \frac{1}{2}\right)\hbar\omega + \frac{\hbar^2 k^2}{2M}. \tag{1.17}$$

The subband bottoms are separated an energy $\hbar\omega$. Fig. 1.3 shows a situation in which only two subbands are filled, up to the Fermi energy E_F. The filling factor is plotted as a continuous function because we assume the length L of the sample to be very large. The states at the intersections of the subbands and the Fermi energy have equal but opposite momenta $\hbar k = \pm\sqrt{2M[E_F - (N + \frac{1}{2})\hbar\omega]}$ and thus propagate in opposite directions. The magnetic field spatially separates the edge states by shifting them towards opposite boundaries. These so-called edge channels were first introduced by Halperin [12] adapting an original argument by Laughlin [13] concerning the quantized Hall conductance. Since then
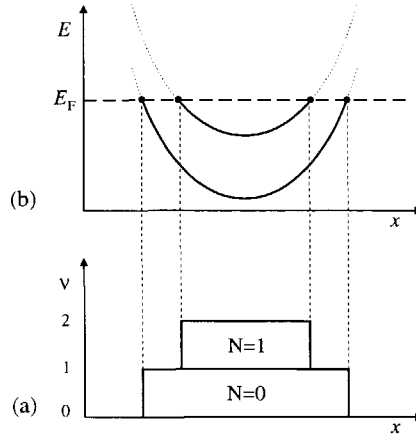
Figure 1.3: *Single-electron picture of edge channels. (a) Electronic filling factors in the wire. (b) Corresponding energy levels. The dashed line is the Fermi energy level and the dots indicate the position of the edge channels.*

a considerable amount of effort has been devoted to elucidate the physics of edge channels in various circumstances, resulting in a number of controversies which even now have only partially been resolved. The effect of electron-electron interactions on the spatial structure of the edge channels is one of these open problems, and it is the subject of the next section.

We end the present section by briefly elaborating on the relevance of edge channels for transport through the wire. If a small voltage V is applied between two reservoirs located at either end of the wire, the electrochemical potential difference between both ends is $\mu_1 - \mu_2 = eV$. The density of states for the Nth subband reads:

$$\rho_N(E) = \frac{1}{2\pi}\frac{dk}{dE} = \frac{1}{2\pi}\left.\frac{dE_N(k)}{dk}\right|_E^{-1}, \tag{1.18}$$

and the group velocity is given by:

$$v_N(E) = \left.\frac{dE_N(k)}{\hbar dk}\right|_E. \tag{1.19}$$

The current carried by subband N from one side to the other is

$$i_{N,\to}(E) = ef_{\to}(E)\rho_N(E)v_N(E) = \frac{e}{h}f_{\to}(E), \tag{1.20}$$

where f denotes the Fermi-Dirac distribution function. This result is independent of the subband index N because the density of states and the group velocity cancel. Therefore all subbands carry the same current. However, in a real sample this need not be the case. Due to scattering events in the wire, caused by impurities or by the geometry of the structure, only a fraction $T_N(E)$ of the current will be transmitted through subband N, resulting in a

current $I_{N,\rightarrow}(E) = T_N(E)i_{N,\rightarrow}(E)$. The total current at zero temperature is then given by:

$$
\begin{aligned}
I &= \int_{E_{\rm F}-\frac{1}{2}eV}^{E_{\rm F}+\frac{1}{2}eV} dE \sum_N \left[I_{N,\rightarrow}(E) - I_{N,\leftarrow}(E)\right] \\
&= \frac{e}{h} \int_{E_{\rm F}-\frac{1}{2}eV}^{E_{\rm F}+\frac{1}{2}eV} dE \sum_N T_N(E) \left[f_\rightarrow(E) - f_\leftarrow(E)\right] \\
&= \frac{e^2}{h} V \sum_N T_N(E_{\rm F}).
\end{aligned}
\tag{1.21}
$$

Taking spin into account the conductance becomes:

$$
G = 2\frac{e^2}{h} \sum_N T_N(E_{\rm F}).
\tag{1.22}
$$

This is the Landauer formula for a two terminal geometry [14], which was generalized to multiple-reservoir conductors by Büttiker [15]. Eq. (1.22) clarifies the importance of edge channels for transport in the quantum wire, since it shows that the conductance is determined by the transmission coefficients of the subbands at the Fermi energy, i.e. the transmission coefficients of the edge channels. At high magnetic fields the edge channels become spatially separated and back scattering between those with opposite momentum is suppressed. In that limit the conductance equals e^2/h times the number of occupied Landau levels.

1.1.4 Interaction effects

The effect of the Coulomb interaction between 2D electrons in the presence of a magnetic field was first considered in the qualitative pictures of screening of Refs. [16, 17], in which the 2DEG was divided into alternating strips of so-called compressible and incompressible liquids. The incompressible strips are caused by the discontinuity of the chemical potential for filling factors which correspond to gaps in the electronic excitation spectrum. The screening properties of these insulating strips are very poor, whereas the compressible liquid behaves like a metal and screens well. In Refs. [18, 19], a quantitative description in terms of classical electrostatics leads to estimates for the widths of the compressible and incompressible regions. Surprisingly, the width of the incompressible strips turned out to be much smaller than the width of the compressible ones, in sharp contrast to the noninteracting picture.

In Fig. 1.4 the relevant results of Ref. [19] are compared with the single-particle picture of edge states. In the figure two distinct ground states are shown, which are labeled I and C, depending on whether the bulk of the wire consists of incompressible or compressible liquid. Whereas the one-electron description simply shows adiabatic bending of the Landau levels by the external potential and an oversimplified density profile, the electrostatic picture is clearly more sophisticated.

The sharp density profiles of the non-interacting picture are very unfavorable from an electrostatic point of view. Therefore the solutions of figures Fig. 1.4 (f) and (i) are close to the electrostatic solution *in the absence* of a magnetic field. In the case of a parabolic confinement potential this zero-field density distribution is a semi-circle which screens the
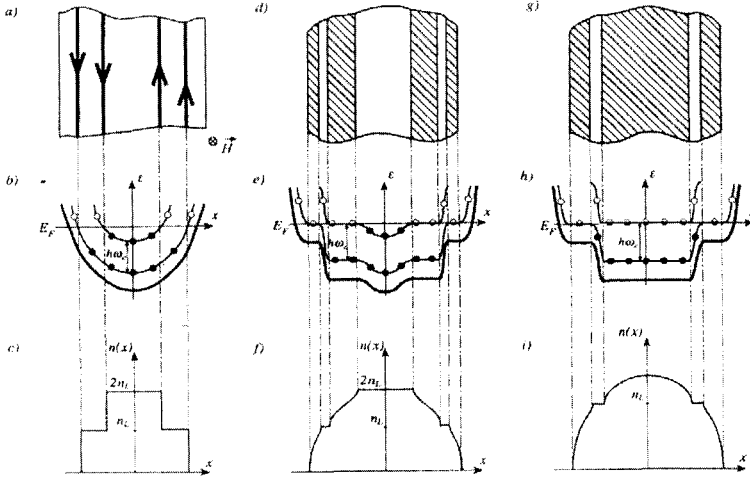
Figure 1.4: *(a)-(c) Non-interacting picture of edge channels. (d)-(f) I state of the quantum wire. (g)-(i) C state of the quantum wire. The top row of figures shows a top view of the strip of 2DEG, where the shaded strips represent the compressible regions and the unshaded strips the incompressible regions. The second row shows the bending of the electrostatic potential and the Landau levels. The circles represent the local filling factor; •, filled; and ○, empty. The bottom row shows the density profiles in the channel. The figure is taken from Ref. [19].*

external potential in the wire completely. However, because of the cyclotron gaps that occur in a magnetic field, the solution is altered. Now the electrons in the vicinity of the $n = n_{\mathrm{L}}$ line are kept at a constant density because of the gap in the electron spectrum, which we referred to as an incompressible strip above. These incompressible strips are separated by regions of electron liquid in which the electrons are free to move and hence screen the external potential. In these regions the electron density varies and the electrostatic potential energy is constant. These regions are the compressible strips.

Essentially, the interaction between electrons in the above description is taken into account classically. As a consequence, the exchange interaction is not accounted for. This quantum mechanical effect, which opposes the electrostatic forces, is accounted for by the Hartree-Fock approximation. Whereas the direct, long-range Coulomb repulsion favors a large-sized wire or dot, the attractive and short-range exchange interaction allows the system to lower its energy again by holding the electrons together. We therefore have to deal with two competing forces, the interplay of which results in some interesting features near the system boundaries.

In the Hartree-Fock approximation at zero temperature the total ground state wave function of the system is a Slater determinant of single-particle orbitals which are either empty or occupied. The ground state density is:

$$n(\mathbf{r}) = \sum_{Nk\sigma} \nu_{Nk}^{\sigma} |\psi_{Nk}^{\sigma}(x)|^2, \tag{1.23}$$

where the filling factor ν_{Nk}^{σ} is given by:

$$\nu_{Nk}^{\sigma} = f(\varepsilon_{Nk}^{\sigma}),\tag{1.24}$$

with $f(\varepsilon)$ the Fermi-Dirac distribution function and $\varepsilon_{Nk}^{\sigma}$ the electron energies. Because the Fermi-Dirac distribution function is either zero or one at $T = 0$, the filling factors are restricted to integer values.

Recently, a number of Hartree-Fock calculations have been carried out on quantum wires and dots [20, 21, 22]. In these papers the stability of the Hartree-Fock ground state against bulk and edge excitations was studied. Two important possible edge reconstructions are plotted in Fig. 1.5. These edge reconstructions are induced by a decrease in confinement
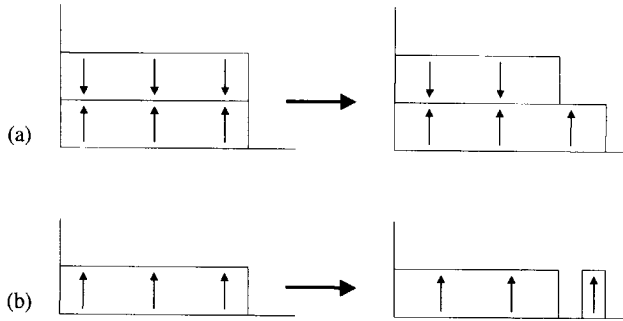
Figure 1.5: *Two different edge reconstructions that are possible when the confinement is decreased or, alternatively, the magnetic field is increased. Plotted are the filling factors before and after some critical confinement strength. (a) The spontaneous separation of edge channels as discussed in Ref. [20]. (b) The edge reconstruction of Ref. [22].*

strength, or, alternatively, by an increase in applied magnetic field. Fig. 1.5 (a) shows a spontaneous transition from a spin-unpolarized to a spin polarized ground state in the absence of Zeeman splitting. In the presence of Zeeman splitting there is always a small but finite splitting between the edge channels, irrespective of the strength of the confinement. Interestingly, the actual size of the splitting between the edge channels is determined by the *direct* interaction only, because for any solution with integral filling, the total exchange energy is the same [20]. In Fig. 1.5 (b) we have plotted the transition from a fully spin polarized ground state (called a maximum density droplet) of minimal width to a ground state where a narrow strip has moved away from the edge of the system. This edge reconstruction can happen even though exchange favors a compact wire. At a critical confinement strength it becomes energetically favorable to make the transition to a more extended configuration favored by the direct interaction at the cost of exchange energy [22]. This transition has been measured in lateral quantum dots [23] and more recently also in a vertical quantum dot [24].

The two descriptions that we have discussed above both have their merits and weaknesses. The electrostatic picture of Ref. [18] neglects the influence of the exchange interaction and the Hartree-Fock calculation is restricted to configurations of (electrostatically

unfavorable) integer fillings. An alternative way to incorporate electron-electron interaction is by means of density-functional theory. Recently, several independent applications of density-functional theory of the two-dimensional electron gas in high magnetic fields have been reported [25, 26, 27], thus establishing the method as a useful and accurate tool. In chapter 2 we develop a relatively simple numerical scheme based on density-functional theory that takes into account exchange in a local density approximation and that moreover allows for fractional filling [27]. We find that the shape of the density distribution depends sensitively on the strength of the confinement potential, the electrostatic description being valid for weak and the Hartree-Fock picture for strong confinement strengths.

1.2   Time-dependent electrical transport in a double quantum dot

Although its name suggests otherwise, a quantum dot is not an infinitesimally small entity. On the contrary, solid state quantum dots are actually quite large compared to atomic dimensions because they are made of roughly a few million atoms. Virtually all electrons in the dot, however, are bound to the nuclei of these atoms and the number of free electrons can be very small, varying from one to several hundreds. Because the wave length of the electrons is comparable to the size of the dot, its properties are in general governed by quantum mechanics: The electrons occupy discrete energy levels and have a discrete excitation spectrum (see Fig. 1.6). Because the capacitance of the dot to the external environment is very small, the energy to add an electron to the dot is usually much larger than the average energy level spacing Δ in the dot. This addition energy is called the charging energy E_c because its magnitude is dominated by the electrostatic energy needed to add an extra electron. If the charging energy is too large, extra electrons are prevented from entering the dot. In a transport experiment this results in a vanishing current through the dot, a phenomenon known as the Coulomb blockade (see Fig. 1.6). It is possible to lift the blockade by applying a voltage to a gate electrode in the vicinity of the dot. The energy levels in the dot are then shifted downwards, until it is again possible to add an extra electron.

Because of their likeness of real atoms, quantum dots are often referred to as artificial atoms. The discrete energy spectrum in the dot corresponds to atomic orbitals and the charging energy is analogous to the ionization energy of an atom. The Coulomb potential, which in atoms is responsible for keeping the electrons bound to the nucleus, is in quantum
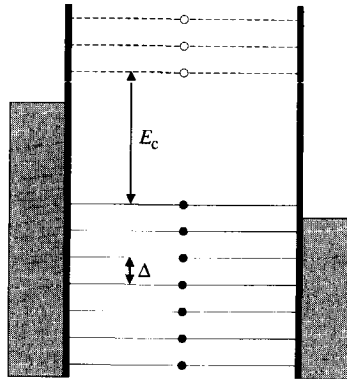
Figure 1.6: *Potential landscape of a quantum dot. The states in the reservoirs are filled up to their respective electrochemical potentials. The filled circles indicate the N discrete occupied states in the dot. The unoccupied states are indicated by empty circles. Also shown are the average level spacing Δ and the charging energy E_c. The transport through the quantum dot is blocked because the energy of the N + 1 state is higher than the electrochemical potentials of the reservoirs.*

dots replaced by an external confinement potential. In contrast to its atomic counterpart this confinement potential can be tuned at will. Quantum dots are thus superior model systems for studying the behavior of few-electron systems. But whereas the properties of an atom are usually determined by studying its interaction with light, quantum dots are generally studied with transport and capacitance measurements. However, as we shall see below, it is also possible to perform spectroscopy on quantum dots with electromagnetic radiation. The rich field of quantum dot physics is thus determined by the interplay of a number of internal factors, such as charge and size quantization, charging effects, and electron-electron interactions in the dot, and a number of external ones, like the application of magnetic fields or electromagnetic radiation. For an overview of the work done on quantum dots we refer here to Refs. [28, 29]. We now turn to a discussion of a relatively new topic in this field; double quantum dots.

1.2.1 DOUBLE QUANTUM DOTS

As we have seen, a single quantum dot can be looked upon as an artificial atom in which the Coulombic nuclear potential has been replaced by an external confinement potential. But whereas in a real atom all properties are fixed, in a quantum dot several parameters, e.g. the confinement potential and the number of electrons, can be easily tuned. It is also possible to create artificial molecules in the form of multiple dots. Two mechanisms cause coupling between two dots. Via the Coulomb interaction the charge on one dot influences the electrostatic potential of the other. More interesting, however, is the quantum mechanical effect of an electron that coherently tunnels back and forth between the dots, thus forming the analogue of a covalent bond between the artificial atoms.

In metallic systems quantum size effects are in general insignificant because the Fermi wavelength is typically much smaller than the sample size ($\lambda_F \approx 0.1$ nm). However, in semiconductor dots these effects can be appreciable because the much lower electron density results in a characteristic Fermi wavelength of $\lambda_F \approx 20$ nm, comparable to the system size.

Fig. 1.7 shows the gate configuration that was used in Ref. [30] to define two semiconductor quantum dots in series. Applying a negative voltage to the gates depletes the 2DEG

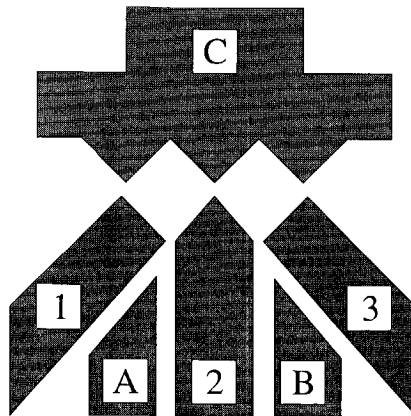Figure 1.7: *Gate configuration for the double quantum dot used in Ref. [30].*

underneath them and thus two weakly coupled quantum dots are formed. A current can flow from the reservoir on the left to the reservoir on the right via three tunnel barriers. These tunnel barriers are induced by the gate pairs 1-C, 2-C, and 3-C and their heights can be tuned separately by the voltages on gates 1, 2, and 3. The gates A and B are used to define single dots that are characterized individually before the actual double-dot measurements are performed [30].

In a single quantum dot which is coupled weakly to two reservoirs, the confinement of electrons in all three spatial dimensions causes a completely discrete spectrum of 0D states. By measuring the resonant tunneling peaks that occur each time a 0D state lines up with the Fermi level in the reservoir, it is possible to characterize this 0D spectrum accurately. However, it is almost impossible to determine the intrinsic width (or life time) of these 0D states because the temperature of the reservoirs is responsible for thermally broadening the resonant peaks. In a double dot this complication does not occur because the resonant tunneling occurs between two discrete states without involving the thermally smeared continuum of the reservoirs, allowing accurate spectroscopy of the 0D spectrum.

Let us consider a double dot like the one used in Ref. [30], which is depicted in Fig. 1.7. We assume that there are two (full many-body) states, $|a\rangle$ and $|b\rangle$, with a small energy difference ε_0. In state $|a\rangle$ there is an extra electron in the left dot and in state $|b\rangle$ there is an extra electron in the right one. The probabilities to be in one of the states is denoted by ρ_{aa} and ρ_{bb}, respectively. We assume now that the Coulomb blockade is strong enough to make it impossible for an electron to enter the double-dot system when an extra electron is already present in either one of the dots. We eliminate the degrees of freedom of the reservoirs so that the only diagonal density matrix element left is $\rho_0 = 1 - \rho_{aa} - \rho_{bb}$, i.e. the probability that the system is in the state without any extra electron in the double dot. In principle, it is also possible to account for a second electron entering the dot. However, the energy of this state with two electrons in the double-dot system would be much higher than that of the resonant states and it would therefore not contribute to the *resonant* current, but only to a featureless background current. We therefore disregard all states other that the resonant ones from now on. This is called the two-state approximation, which is valid near resonance. Additionally, we assume a sufficiently large bias voltage, such that electrons must tunnel from the left lead to the left dot to enter the system, and must tunnel from the right dot to the right lead to leave it again. We account for mixing between the resonant states $|a\rangle$ and $|b\rangle$ quantum mechanically using the tunneling Hamiltonian:

$$\mathcal{H}_{\mathrm{T}} = T|a\rangle\langle b| + T|b\rangle\langle a|, \qquad (1.25)$$

where T is the overlap matrix element between the resonant states.

It is possible to rigorously derive rate equations for the dynamics of the reduced density matrix elements of the system [31, 32]. In the reduced density matrix the reservoir degrees of freedom are integrated out and one is left with the relevant matrix elements that pertain to the discrete states in the double-dot system. Besides its mathematical simplicity, the big advantage of this approach is the fact that Coulomb blockade effects can be taken into account in a straightforward manner. For more information about the density matrix in

quantum mechanics and its properties see e.g. Ref. [33]. The final set of equations reads:

$$\frac{\partial \rho_{aa}}{\partial t} = +\Gamma_{\mathrm{L}} \, \rho_0 + iT \, (\rho_{ba} - \rho_{ab}) \tag{1.26}$$

$$\frac{\partial \rho_{bb}}{\partial t} = -\Gamma_{\mathrm{R}} \, \rho_{bb} - iT \, (\rho_{ba} - \rho_{ab}) \tag{1.27}$$

$$\frac{\partial \rho_{ab}}{\partial t} = -\frac{1}{2}\Gamma_{\mathrm{R}} \, \rho_{ab} + i\varepsilon_0 \, \rho_{ab} + iT \, (\rho_{bb} - \rho_{aa}) \tag{1.28}$$

$$\frac{\partial \rho_{ba}}{\partial t} = -\frac{1}{2}\Gamma_{\mathrm{R}} \, \rho_{ba} - i\varepsilon_0 \, \rho_{ba} - iT \, (\rho_{bb} - \rho_{aa}), \tag{1.29}$$

where Γ_{L} is the tunnel rate from left reservoir to left dot and Γ_{R} is the tunnel rate from right dot to right reservoir. In the absence of coherent transport between the dots, the equations for the off-diagonal elements ρ_{ab} and ρ_{ba} would not be present and the rate equations would assume the form of a classical master equation. Solving for the stationary solution it is easy to derive an expression for the shape of a resonant tunneling peak [31, 30]:

$$I_{\mathrm{peak}}(\varepsilon_0) = \frac{T^2 \Gamma_{\mathrm{R}}}{T^2 (2 + \Gamma_{\mathrm{R}}/\Gamma_{\mathrm{L}}) + \Gamma_{\mathrm{R}}^2/4 + \varepsilon_0^2}. \tag{1.30}$$

Clearly, the line shape is determined by intrinsic parameters only. Van der Vaart *et al.* indeed observed the Lorentzian line shape of Eq. (1.30) independent of reservoir temperature [30].

1.2.2 TIME-DEPENDENT TRANSPORT

Recently, a number of transport experiments have been performed that involved subjecting mesoscopic structures to electromagnetic irradiation [34, 35, 36, 37, 38, 39, 40]. Besides these experimental advances, a number of theoretical efforts have been reported over the years [41, 42, 43, 44, 45, 46, 47, 48, 49, 50]. Due to the irradiation, or equivalently, the application of ac voltages, electrons can absorb or emit a number of photons during a tunneling process. This is known as photon-assisted tunneling.

Consider a single tunnel junction with conductivity G_{T} between two metal reservoirs biased at a voltage V. The "orthodox" theory of single-electron tunneling then predicts a tunnel rate through the junction [51]:

$$\Gamma(\varepsilon) = \frac{G_{\mathrm{T}}}{e^2} \frac{\varepsilon}{1 - \exp(-\varepsilon/kT)}, \tag{1.31}$$

where $\varepsilon = \varepsilon_{\mathrm{i}} - \varepsilon_{\mathrm{f}}$ is the energy difference between the initial and final many-body state, including the work done by the voltage source. In the presence of an alternating voltage $\tilde{V} \cos \omega t$ across the junction, this tunnel rate is modified as follows [41]:

$$\tilde{\Gamma}\left(\varepsilon, \frac{e\tilde{V}}{\hbar\omega}\right) = \sum_{n=-\infty}^{\infty} J_n^2\left(\frac{e\tilde{V}}{\hbar\omega}\right) \Gamma(\varepsilon + n\hbar\omega), \tag{1.32}$$

where J_n are nth order Bessel functions. Eq. (1.32) thus shows that the weight for an electron tunneling through the junction by absorbing or emitting n photons is $J_n^2\left(\frac{e\tilde{V}}{\hbar\omega}\right)$.

The total current is independent of the power and frequency of the applied ac voltage since

$$\sum_{n=-\infty}^{\infty} J_n^2 \left(\frac{e\tilde{V}}{\hbar\omega} \right) = 1. \tag{1.33}$$

For a single junction, the I-V curve for the irradiated system can be calculated immediately using Eq. (1.32). However, for multi-junction systems, like single or double quantum dots, electron transfer is correlated and a more careful analysis is required.

Fig. 1.8 shows how the electron transfer through a double quantum dot is affected by photon-assisted tunneling. In the absence of irradiation, transport is only possible when
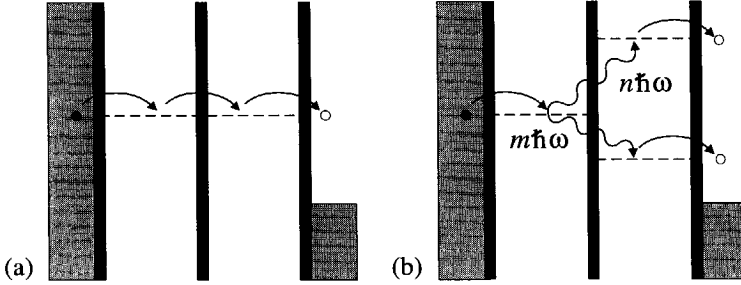
Figure 1.8: *Electron transport through a double quantum dot (a) without irradiation, and (b) in the presence of photon-assisted tunneling.*

the two resonant energy levels of the dots line up. These energy levels are the energies of the full many-body states with one extra electron in the left and one extra electron in the right dot, respectively. In the presence of photon-assisted tunneling, however, an electron can traverse the dots by e.g. absorbing n quanta $\hbar\omega$ or emitting m quanta, as shown in Fig. 1.8.

In chapter 3 we consider a double-dot system subject to irradiation [49]. Using the formalism of Ref. [31], we derive equations for the reduced density-matrix elements in the presence of radiation. These equations bear strong resemblance to the optical Bloch equations for atoms interacting with electromagnetic radiation [52], proving once more the appropriateness of the denomination "artificial atom". In the limit of weak irradiation power, we find satellite peaks in the photoresponse of the dot when the frequency of the applied irradiation matches the renormalized energy difference of the resonant states, $\omega \approx \sqrt{\varepsilon_0^2 + 4T^2}$. In this limit of large inter-dot coupling, an electron coherently tunnels a few times between the dots before leaving the system, a phenomenon sometimes referred to as *spatial Rabi oscillations*. In the limit of strong irradiation amplitude we calculate the magnitude of the various satellite peaks corresponding to multiple photon absorption and emission processes as a function of the applied irradiation power, finding a $J_n^2(\frac{e\tilde{V}}{\hbar\omega})$ dependence.

In chapter 4 we present an electron pump based on photon-assisted tunneling through a double-dot system. Depending on the energies of the intermediate states of the pumping cycle, the pump can transfer electrons incoherently, via sequential tunneling, or coherently, via co-tunneling. We derive equations for the density-matrix elements in the limit of weak irradiation and calculate the current for both mechanisms. In both cases the pumping

current is a Lorentzian, but whereas the width of the incoherent peak is relatively large, it is very narrow in the coherent regime. Moreover, its width changes nonmonotonically as a function of the co-tunnel rate in the latter regime.

1.3 NONEQUILIBRIUM SUPERCONDUCTIVITY

In 1957 Bardeen, Cooper and Schrieffer published their famous pairing theory of supercon-
ductivity [53], thus providing a microscopic description of this phenomenon that had been
eluding a satisfactory explanation since its discovery in 1911 by Kamerlingh Onnes [54].
Initially, mainly bulk properties of superconductors were studied, soon followed by the
properties of bulk normal metal-bulk superconductor interfaces. Electron wave functions
in the normal metal are distorted by the penetrating superconductivity in the vicinity of
the superconductor, a phenomenon known as the proximity effect. The implications of this
effect for the transport properties of mesoscopic devices, in which the superconducting co-
herence length in the normal metal is of the order of the sample size, are in general not *a
priori* evident, hence the activity in this field. Moreover, owing to technological progress, it
has recently become possible to fabricate normal metal-superconducting hybrid structures
with the desired characteristic size of a few micrometers. It is to a large extent due to
these technological advances that today, forty years after the formulation of BCS theory,
the field of mesoscopic superconductivity is still thriving. In this third and final part of
the introduction we will briefly introduce some relevant concepts of transport in hybrid
superconducting structures.

1.3.1 ANDREEV INTERFEROMETRY

An important physical process responsible for the transport of charge through a N-S in-
terface is called Andreev reflection and is depicted in Fig. 1.9. It was first described by
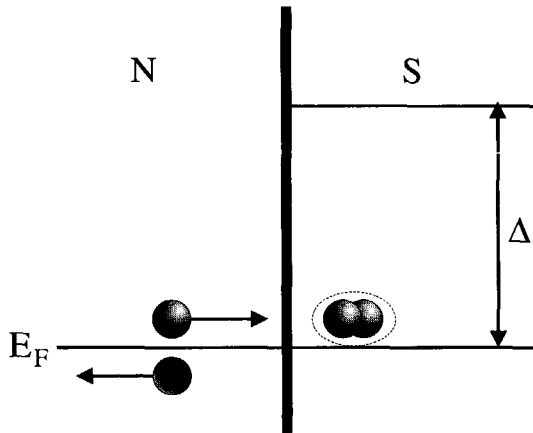
Figure 1.9: *Andreev reflection: An electron impinges on the normal metal-
superconductor interface and is reflected as a hole, leaving behind an extra Cooper
pair in the superconductor.*

Andreev in order to compute the thermal resistance of an N-S interface [55]. It was elabo-
rated and formulated in the now well known form in Refs. [56, 57]. Normal electrons with
energy $\varepsilon < \Delta$ incident on the N-S interface are not able to penetrate the superconductor
as quasiparticles, because there are no quasiparticle states available in the superconducting

gap. Instead, they are reflected as holes, thus transferring a charge $2e$ across the interface. The Andreev reflected hole travels along the time-reversed path of the electron and its phase has picked up the macroscopic phase of the superconductor. If the energies of the impinging normal electrons are much smaller than the superconducting gap, $\varepsilon \ll \Delta$, practically all electrons are Andreev reflected, resulting in a differential conductance that is twice as large as in the normal state. The theory of transport through an N-S interface was refined in several papers [58, 59, 60] and is nowadays generally accepted.

An interesting application of the phenomenon of Andreev reflection is realized when two superconductors are connected to a normal metal structure, e.g. like in the lay-out shown in Fig. 1.10. This device, which was first described in Ref. [61], consists of a normal metal
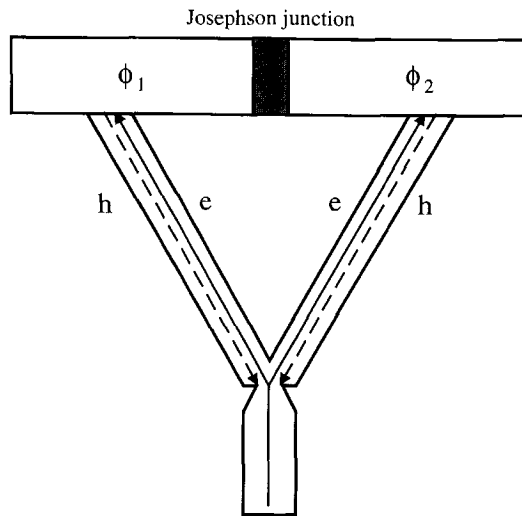
Figure 1.10: *The Andreev interferometer of Ref. [61].*

fork connected to a Josephson junction. The superconductors on either side of the junction have different macroscopic phases ϕ_1 and ϕ_2. The wave function of an electron coming from below is split into two by a constriction in the middle of the fork. One part travels to the left side of the junction and the other to the right. At the superconducting interface, both parts are Andreev reflected, pick up the phase of the superconductor, and travel back to the constriction. Because the hole wave function follows the time-reversed path of the electron, the phase gained by the electron traversing the left and right branches is exactly canceled again by the phase gained by the returning hole. When the two hole parts meet again in the middle of the structure, they interfere having a phase difference equal to the macroscopic phase difference of the superconductors, $\phi_1 - \phi_2$. By now, a large number of these "Andreev interferometers" have been studied theoretically [61, 62, 63, 64, 65, 66, 67, 68] and realized experimentally [69, 70, 71, 72, 73, 74].

1.3.2 THE QUASICLASSICAL GREEN FUNCTION IN DIFFUSIVE SUPERCONDUCTORS

Roughly speaking, two different sorts of Andreev interferometer have been fabricated to date. One can either use a metal or a two-dimensional electron gas for the normal part. In the former the mean free path is usually much smaller than the sample size and the transport is therefore diffusive, whereas the latter can be very clean, thus enabling ballistic transport. In all cases of practical interest the metallic superconducting hybrid structures are in the diffusive regime. However, very often transport in the 2DEG is also diffusive and we will therefore only consider the dirty limit here.

For our present purposes, the transport properties are most suitably formulated in terms of quasi-classical Green functions, which capture the essential physics. Furthermore, the Green functions become local in the diffusive limit, resulting in equations that can be solved relatively easily. The quasi-classical approximation was first introduced independently by Eilenberger [75] and by Larkin and Ovchinnikov [76]. Because we are concerned with nonequilibrium properties of the superconductor, it is necessary to use a generalized set of Green functions due to Keldysh [77]. The Keldysh formalism was applied to superconductivity by Larkin and Ovchinnikov [78]. This section is not intended to give an extensive overview of the many aspects of the quasi-classical theory of superconductivity (they can be found in e.g. Refs. [79, 80]). Instead we show how the equations used in chapters 5 to 7 are related to the more familiar BCS theory. In doing so we will follow Ref. [78].

We start with the Gorkov equations [81] for the Green function G and the "anomalous" Green function F, which are equivalent to the conventional Bogoliubov-De Gennes equations:

$$\left[i \frac{\partial}{\partial t_1} + \frac{(\nabla - ie\mathbf{A})^2}{2m} - e\varphi - \mu \right] G(x_1, x_2) + \Delta F^\dagger(x_1, x_2) = \delta(x_1 - x_2), \tag{1.34}$$

$$\left[-i \frac{\partial}{\partial t_1} + \frac{(\nabla + ie\mathbf{A})^2}{2m} - e\varphi - \mu \right] F^\dagger(x_1, x_2) - \Delta^* G(x_1, x_2) = \delta(x_1 - x_2), \tag{1.35}$$

where $x_1 = (\mathbf{r}_1, t_1)$, φ is the scalar potential, $\mathbf{A}$ the vector potential, μ the chemical potential, Δ the pair potential, and we have used units such that $\hbar = 1$. In Keldysh notation the generalized Gorkov equation reads:

$$\left[i\breve{\sigma}_z \frac{\partial}{\partial t_1} + \breve{1} \left(\frac{\breve{\partial}^2}{2m} - e\varphi + \mu \right) + \breve{\Delta} - \breve{\Sigma} \right] \breve{G}(x_1, x_2) = \breve{1}\delta(x_1 - x_2), \tag{1.36}$$

where $\breve{\partial} = \breve{1}\frac{\partial}{\partial \mathbf{r}_1} - ie\breve{\sigma}_z \mathbf{A}$. Now the Green function $\breve{G}$ and self energy $\breve{\Sigma}$ are (4×4) matrices that are of the form:

$$\breve{G} = \begin{pmatrix} \hat{G}^{\mathrm{R}} & \hat{G}^{\mathrm{K}} \\ 0 & \hat{G}^{\mathrm{A}} \end{pmatrix} ; \breve{\Sigma} = \begin{pmatrix} \hat{\Sigma}^{\mathrm{R}} & \hat{\Sigma}^{\mathrm{K}} \\ 0 & \hat{\Sigma}^{\mathrm{A}} \end{pmatrix}, \tag{1.37}$$

where the superscripts A, R, and K stand for advanced, retarded, and Keldysh, respectively. The Green functions $\hat{G}$ are the usual (2×2) matrices in Nambu space [82]:

$$\hat{G}^{\mathrm{A}}(x_1, x_2) = \begin{pmatrix} G^{\mathrm{A}}(x_1, x_2) & F^{\mathrm{A}}(x_1, x_2) \\ F^{\mathrm{A}\dagger}(x_1, x_2) & -G^{\mathrm{A}}(x_2, x_1) \end{pmatrix}, \tag{1.38}$$

and analogous equations for $\hat{G}^{\mathrm{R}}$ and $\hat{G}^{\mathrm{K}}$. The self energy term takes into account the interaction of electrons with phonons and (magnetic) impurities. $\check{\Delta}$ and $\check{\sigma}_z$ are given by:

$$\check{\Delta} = \begin{pmatrix} \hat{\Delta} & 0 \\ 0 & \hat{\Delta} \end{pmatrix}, \hat{\Delta} = \begin{pmatrix} 0 & \Delta \\ -\Delta^\star & 0 \end{pmatrix}, \tag{1.39}$$

where Δ is again the pair potential in the metal and

$$\check{\sigma}_z = \begin{pmatrix} \hat{\sigma}_z & 0 \\ 0 & \hat{\sigma}_z \end{pmatrix}, \hat{\sigma}_z = \begin{pmatrix} 1 & 0 \\ 0 & -1 \end{pmatrix}. \tag{1.40}$$

The necessity of three Green functions in the theory is a consequence of the fact that it describes nonequilibrium phenomena. Like in equilibrium theory, the advanced and retarded Green functions determine the dispersion of the quasiparticles in the structure. However, to describe nonequilibrium properties it is also necessary to know how the states are occupied when the system is driven out of equilibrium. As we will see below, the Keldysh Green function can be expressed in terms of the advanced and retarded ones and a distribution function which describes how the energy spectrum is filled by the quasiparticles.

For the further development of the theory it is advantageous to introduce the Wigner or mixed representation. The first step is a shift of the frame of reference to center-of-mass coordinates $\mathbf{r}$ and the introduction of relative coordinates $\mathbf{r}'$:

$$\mathbf{r} = \frac{\mathbf{r}_1 + \mathbf{r}_2}{2}, \ \mathbf{r}' = \mathbf{r}_1 - \mathbf{r}_2. \tag{1.41}$$

Secondly, we Fourier transform with respect to $\mathbf{r}'$:

$$\check{G}(\mathbf{p}, \mathbf{r}, t_1, t_2) = \int d^3 \mathbf{r}' e^{-i\mathbf{p}\mathbf{r}'} \check{G}\left(\mathbf{r} + \frac{\mathbf{r}'}{2}, \mathbf{r} - \frac{\mathbf{r}'}{2}, t_1, t_2\right) \tag{1.42}$$

In a degenerate Fermi system all physical quantities vary on length scales much larger than the Fermi wave length and as a result the quasiclassical approximation is often allowed. We may then approximate $|\mathbf{p}| = p_{\mathrm{F}}$ and introduce the quasiclassical Green function $\check{g}$:

$$\check{g}(\hat{p}, \mathbf{r}, t_1, t_2) = \frac{i}{\pi} \int d\xi_{\mathbf{p}} \check{G}(\mathbf{p}, \mathbf{r}, t_1, t_2), \tag{1.43}$$

where $\xi_{\mathbf{p}} = \frac{\mathbf{p}^2}{2m} - \mu$ and the $\hat{p}$ in the argument of the quasiclassical Green function denotes the fact that the momentum dependence is restricted to a dependence on the direction of the momentum only, since its magnitude is fixed at $|\mathbf{p}| = p_{\mathrm{F}}$.

The equation of motion for the quasiclassical Green function is found by first noting that Eq. (1.36), which has the structure $\check{G}^{-1}\check{G} = \check{1}$, can be rewritten in the adjoint form $\check{G}\check{G}^{-1} = \check{1}$. In the latter relation, $\check{G}^{-1}$ operates on the variables $\mathbf{r}_2$ and t_2. We subtract Eq. (1.36) from its adjoint and transform to the momentum representation. Integrating the resulting equation over $\xi_{\mathbf{p}}$ leads to an equation of motion for the quasiclassical Green function Eq. (1.43):

$$\frac{\mathbf{p}}{m}\frac{\partial \check{g}}{\partial \mathbf{r}} + \check{\sigma}_z \frac{\partial \check{g}}{\partial t_1} + \frac{\partial \check{g}}{\partial t_2}\check{\sigma}_z + i\check{H}(t_1)\check{g} - i\check{g}\check{H}(t_2) \ +$$
$$i \int dt_3 \left\{ \check{\Sigma}(t_1, t_3)\check{g}(t_3, t_2) - \check{g}(t_1, t_3)\check{\Sigma}(t_3, t_2) \right\} \ = \ 0, \tag{1.44}$$

where $\check{H}(t) = -\frac{e}{m}\mathbf{p}\mathbf{A}(t)\check{\sigma}_z - \check{\Delta}(t) + e\varphi(t)\check{1}$. These equations were first derived by Eliashberg [83]. Because Eq. (1.44) is homogeneous, an extra constraint is necessary to determine the Green function uniquely. This extra information is enclosed in the normalization condition on $\check{g}$:

$$\int dt_3 \check{g}(t_1, t_3)\check{g}(t_3, t_2) = \check{1}\delta(t_1 - t_2). \tag{1.45}$$

The argument for this normalization is as follows: In thermal equilibrium and for a spatially homogeneous state, explicit calculation shows that Eq. (1.45) holds. For the general case it is possible to derive an equation of motion for the function $\int dt_3 \check{g}(t_1, t_3)\check{g}(t_3, t_2)$ from Eq. (1.44). This equation of motion has exactly the same form as Eq. (1.44), but with $\check{g}$ replaced by $\int dt_3 \check{g}(t_1, t_3)\check{g}(t_3, t_2)$. Clearly this equation is solved by Ansatz (1.45), and since this solution joins up to the equilibrium solution, one concludes that it is the only one [79, 84]. This normalization condition is a very powerful tool, since the right hand side does not depend on the coordinates.

The normalization condition Eq. (1.45) enables us to write the Keldysh component $\hat{g}^{\mathrm{K}}$ of $\check{g}$ in terms of the advanced and retarded Green functions. Recalling the structure of the total Green function, we see that the normalization implies that:

$$\int dt_3 \hat{g}^{\mathrm{A(R)}}(t_1, t_3)\hat{g}^{\mathrm{A(R)}}(t_3, t_2) = \hat{1}\delta(t_1 - t_2), \tag{1.46}$$

and

$$\int dt_3 \left\{ \hat{g}^{\mathrm{R}}(t_1, t_3)\hat{g}^{\mathrm{K}}(t_3, t_2) + \hat{g}^{\mathrm{K}}(t_1, t_3)\hat{g}^{\mathrm{A}}(t_3, t_2) \right\} = 0. \tag{1.47}$$

According to Eq. (1.46), both the advanced and retarded Green functions are independently normalized. The second relation, Eq. (1.47), is satisfied by the Ansatz:

$$\hat{g}^{\mathrm{K}}(t_1, t_2) = \int dt_3 \left\{ \hat{g}^{\mathrm{R}}(t_1, t_3)\hat{f}(t_3, t_2) - \hat{f}(t_1, t_3)\hat{g}^{\mathrm{A}}(t_3, t_2) \right\}, \tag{1.48}$$

where the distribution function $\hat{f}$ is given by:

$$\hat{f} = f_{\mathrm{L}}\hat{1} + f_{\mathrm{T}}\hat{\sigma}_z. \tag{1.49}$$

In equilibrium, the distribution functions are given by:

$$f_{\mathrm{L}}^{\mathrm{eq}} = \tanh\left(\frac{\varepsilon}{2k_{\mathrm{B}}T}\right) \ ; \ f_{\mathrm{T}}^{\mathrm{eq}} = 0, \tag{1.50}$$

which simply corresponds to the Fermi-Dirac distribution, $f = 1 - 2f_{\mathrm{L}}^{\mathrm{eq}}$.

In the case of a superconductor with short mean free path $l = v_{\mathrm{F}}\tau$, i.e. in the diffusive regime, it is possible to get rid of the remaining momentum dependence of the Green function. Assuming a homogeneous distribution of scatterers, we can integrate over all directions of the momentum vector. Because the Green function will be almost isotropic in the dirty limit, we make an expansion in spherical harmonics, keeping only the s- and p-wave parts [85]:

$$\check{g} = \check{g}_s + \mathbf{p}\check{g}_p, \ \mathbf{p}\check{g}_p \ll \check{g}_s, \tag{1.51}$$

where the functions $\check{g}_s$ and $\check{\mathbf{g}}_p$ do no longer depend on $\mathbf{p}$. Using the normalization condition and the equation of motion Eq. (1.44), where at this point only elastic non-spin-flip scattering has been taken into account in a single-site approximation, we find an expression for $\check{\mathbf{g}}_p$:

$$\check{\mathbf{g}}_p = -\frac{\tau}{m}\left\{ie\mathbf{A}\check{\sigma}_{\mathbf{z}}\delta(t_1 - t_2) + \check{g}_s\check{\partial}\check{g}_s\right\}, \tag{1.52}$$

where $\check{\partial} = \check{1}\frac{\partial}{\partial\mathbf{r}_1} - ie\check{\sigma}_z\mathbf{A}$ and $\check{g}_s\check{\partial}\check{g}_s$ denotes $\int dt_3\check{g}_s(t_1,t_3)\check{\partial}\check{g}_s(t_3,t_2)$. Substituting Eq. (1.51) with Eq. (1.52) into Eq. (1.44), neglecting all further scattering processes that contribute to the self energy $\check{\Sigma}$, and averaging over all angles of $\mathbf{p}$, we obtain the final equation of motion for $\check{g}_s$ (we drop the subscript "s" hereafter):

$$\begin{aligned}
-\mathcal{D}\frac{\partial}{\partial\mathbf{r}}\left\{ie\mathbf{A}\check{\sigma}_{\mathbf{z}}\delta(t_1-t_2) + \check{g}\check{\partial}\check{g}\right\} + \check{\sigma}_z\frac{\partial\check{g}}{\partial t_1} + \frac{\partial\check{g}}{\partial t_2}\check{\sigma}_z &+ \\
\left\{ie\varphi(t_1)\check{1} - i\check{\Delta}(t_1)\right\}\check{g} - \check{g}\left\{ie\varphi(t_2)\check{1} - i\check{\Delta}(t_2)\right\} &+ \\
ie\mathcal{D}\left\{\mathbf{A}(t_1)\check{\sigma}_z\check{g}\check{\partial}\check{g} - (\check{g}\check{\partial}\check{g})\mathbf{A}(t_2)\check{\sigma}_z\right\} &= 0
\end{aligned} \tag{1.53}$$

where $\mathcal{D} = \frac{1}{3}v_{\mathrm{F}}l$ is the diffusion constant. In the work presented in chapters 5 to 7, we only consider time-independent problems. As a consequence, the Green function is a function of the time difference $\tau = t_1 - t_2$ only and we can Fourier transform Eq. (1.53) with respect to this time difference. This reduces the internal time integrations in the above discussion to ordinary matrix multiplications and we recover the equations of chapters 5, 6, and 7 for the Green function:

$$\check{g}(\mathbf{r},\varepsilon) = \int d\tau \check{g}(\mathbf{r},\tau)e^{i\varepsilon\tau}. \tag{1.54}$$

By considering the Keldysh component of Eq. (1.53), it is possible to derive equations of motion for the distribution functions f_{L} and f_{T}. However, their general form is quite cumbersome and we will therefore refrain from reproducing them in this introduction. Fortunately they assume a more compact form in the stationary case and when the supercurrent in the structure is negligible. The distribution function f_{L} then reduces to its equilibrium form:

$$f_{\mathrm{L}} = \tanh\left(\frac{\varepsilon}{2k_{\mathrm{B}}T}\right), \tag{1.55}$$

and f_{T} obeys a diffusion equation [68]:

$$\nabla\left(D(\varepsilon,\mathbf{r})\nabla f_{\mathrm{T}}(\varepsilon,\mathbf{r})\right) - \gamma(\varepsilon,\mathbf{r})f_{\mathrm{T}}(\varepsilon,\mathbf{r}) = 0, \tag{1.56}$$

where the first term describes diffusion of quasiparticles with an effective diffusion coefficient:

$$D(\varepsilon,\mathbf{r}) = \frac{\mathcal{D}}{8}\mathrm{Tr}\{(\hat{g}_\varepsilon^{\mathrm{A}} + \hat{g}_{-\varepsilon}^{A\dagger})^2\}, \tag{1.57}$$

that is modified by the penetrating superconductivity. The second term describes absorption of quasiparticles in the superconducting condensate with a coefficient:

$$\gamma(\varepsilon,\mathbf{r}) = \frac{i}{2}\mathrm{Tr}\{(\hat{g}_\varepsilon^{\mathrm{R}} + \hat{g}_\varepsilon^{\mathrm{A}})\hat{\Delta}\}. \tag{1.58}$$

In chapters 5 and 6 we use the quasiclassical theory of the proximity-effect to describe a novel Andreev interferometer based on the pair potential in the normal metal region, which is induced by electron-electron interaction. Fabrication of this device would allow a direct measurement of the interaction parameter of the normal metal. Moreover, we calculate electrical properties of these interferometers, like the temperature-dependent resistance, and the chemical and electrical potential distributions [68].

1.3.3   CIRCUIT THEORY OF ANDREEV CONDUCTANCE

In this final section we want to introduce an interesting application of the quasiclassical theory due to Nazarov [66]. Clearly, the formalism presented above is rather formal and actual calculations can be quite elaborate. In order to overcome this technical difficulty, Nazarov developed a simple-to-use set of rules to calculate the resistance of an arbitrary network of normal metal wires connecting a number of normal and superconducting reservoirs. This theory is valid for sufficiently small systems, $L \ll \xi$, or equivalently, for sufficiently small temperatures and applied voltages, $T, V \ll \Delta, \mathcal{D}/L^2$. Here $\xi = \sqrt{\mathcal{D}/T}$ is the coherence length in the normal metal and Δ the magnitude of the gap in the superconductor.

A key feature of Nazarov's work is the representation of the Green function. At zero temperature, the retarded Green function $\hat{g}^R = s_x \hat{\sigma}_x + s_y \hat{\sigma}_y + s_z \hat{\sigma}_z$ can be represented as a real vector in Pauli-matrix space: $\mathbf{s} = (s_x, s_y, s_z)$. Because the Green function determines the quasiparticle energy spectrum, this vector was dubbed "spectral vector". Like the Green function, a spectral vector $\mathbf{s}$ is normalized, $\mathbf{s}^2 = 1$. The boundary conditions on $\mathbf{s}$ are simple: In a normal reservoir $\mathbf{s} = (0,0,1)$ and in a superconducting terminal with macroscopic phase ϕ, $\mathbf{s} = (\cos\phi, \sin\phi, 0)$. Using these conventions, the theory assumes a form that is very similar to Kirchhoff's network theory for ordinary conductors. However, here the current is not a scalar but a vector in Pauli matrix space. In the following we summarize the network rules, referring to Ref. [66] for the derivations.

In Ref. [66] two sorts of resistive elements are treated; diffusive resistors R_D and tunnel junctions R_T (see Fig. 1.11(a)). The spectral current through these elements in terms of the spectral vectors $\mathbf{s}_1$ and $\mathbf{s}_2$ on either side of the resistive elements is given by:

$$R_D \mathbf{I} = \frac{\mathbf{s}_1 \times \mathbf{s}_2}{\sqrt{1 - (\mathbf{s}_1 \mathbf{s}_2)^2}} \arccos(\mathbf{s}_1 \mathbf{s}_2), \tag{1.59}$$

for a diffusive resistor with resistance R_D and

$$R_T \mathbf{I} = \mathbf{s}_1 \times \mathbf{s}_2, \tag{1.60}$$

for a tunnel junction with resistance R_T.

The circuit theory rules are:

(i) The Andreev conductance of a system is the same as in normal circuit theory except for the fact that the tunnel conductances are renormalized by a factor $\mathbf{s}_1 \mathbf{s}_2$.

(ii) In a normal terminal the spectral vector is the north pole of the hemisphere whereas in a superconducting one it is located on the equator, its longitude ϕ indicating the phase of the superconductor.

(iii) The spectral current is perpendicular to both spectral vectors on either side of the resistive element. For a diffusive conductor the magnitude of the current is $I = G_D \alpha$ and
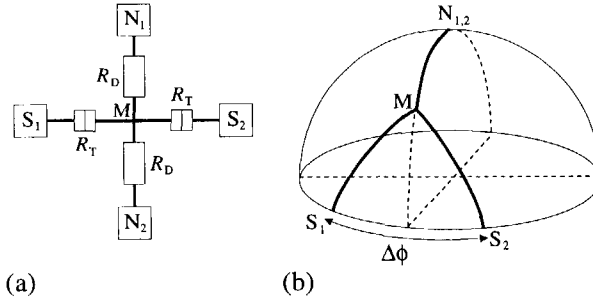
(a)   (b)

Figure 1.11: *(a) An arbitrary network consisting of a cross of normal metal wires connecting two normal reservoirs and two superconducting terminals having phase difference $\Delta\phi$. Two different resistive elements are present, diffusive resistors R_D and tunnel junctions R_T. The superconducting reservoirs are biased at the same voltage. (b) The network mapped onto a hemisphere.*

for a tunnel junction it is $I = G_T \sin\alpha$. Here $\alpha = \arccos(\mathbf{s}_1\mathbf{s}_2)$ is the angle between the two spectral vectors at both ends of the element.
(iv) The *vector* spectral current in all nodal points of the network is conserved.

As an example we calculate the phase-dependent resistance of the structure shown in Fig. 1.11(a), where both tunnel junctions have resistance R_T and both diffusive resistors have resistance R_D. One of the normal terminals is biased at a small voltage V whereas the voltages on all other reservoirs are zero. Using the normalization of the spectral vector it is easy to see that the network can be mapped onto a unit hemisphere as illustrated in Fig. 1.11(b). Without loss of generality we take the phases of the two superconducting terminals $\phi_1 = \frac{\phi}{2}$ and $\phi_2 = -\frac{\phi}{2}$. The spectral vectors of the normal reservoirs are $\mathbf{s}_{N_1} = \mathbf{s}_{N_2} = \mathbf{s}_N = (0,0,1)$ and those of the superconducting terminals are $\mathbf{s}_{S_1} = (\cos\frac{\phi}{2}, \sin\frac{\phi}{2}, 0)$ and $\mathbf{s}_{S_2} = (\cos\frac{\phi}{2}, -\sin\frac{\phi}{2}, 0)$. Because the tunnel junction resistances are equal, the mapped network is symmetric with respect to the $\phi = 0$ axis (see Fig. 1.11). The spectral vector in point M can therefore be written as $\mathbf{s}_M = (\sin\theta_M, 0, \cos\theta_M)$. Spectral current conservation in node M, rule (iv), implies:

$$\sum \mathbf{I} = \mathbf{s}_M \times \left(\frac{2\theta_M}{R_D \sin\theta_M} \mathbf{s}_N + \frac{\mathbf{s}_{S_1} + \mathbf{s}_{S_2}}{R_T} \right) = 0, \qquad (1.61)$$

which leads to a transcendental equation for θ_M:

$$R_D \cos\frac{\phi}{2} \cos\theta_M = R_T \theta_M. \qquad (1.62)$$

This equation, which has a solution for any value of R_D, R_T, and ϕ, determines $\mathbf{s}_M$ and hence also the renormalization factors $\mathbf{s}_M \cdot \mathbf{s}_{S_1} = \mathbf{s}_M \cdot \mathbf{s}_{S_2} = \sin\theta_M \cos\frac{\phi}{2}$. The total resistance of the structure is given by:

$$R_{\text{tot}} = R_D + \frac{R_T R_D}{R_T + 2R_D \mathbf{s}_M \cdot \mathbf{s}_{S_1}}, \qquad (1.63)$$

which is just the normal resistance with R_T replaced by $R_T/(\mathbf{s}_M \cdot \mathbf{s}_{S_1})$, as prescribed by rule (i). Fig. 1.12 shows the resistance of the circuit as a function of the phase difference between the superconductors for different values of $\frac{R_D}{R_T}$ Fig. 1.12 shows that when the tunnel
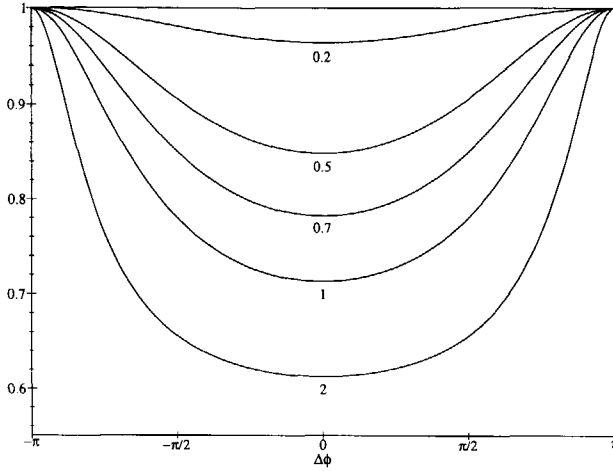
Figure 1.12: *Phase dependence of the scaled resistance $\frac{R_{tot}}{2R_D}$ of the structure shown in Fig. 1.11 for different values of $\frac{R_D}{R_T}$.*

junction resistance is larger then the diffusive resistance, the form of the oscillations reduces to a sinusoidal phase dependence.

In chapter 7 we extend Nazarov's circuit theory to structures that include an Aharonov-Bohm ring, which requires an additional circuit theory rule [86]. Other extensions were discussed recently in Refs. [87, 88], where finite temperatures were also taken into account. An extension of the circuit theory to include semiclassical transport in the ballistic regime was recently given by Argaman [89]. In addition we also predict a flux-dependent electrostatic potential in structures containing Aharonov-Bohm rings.

References

[1] K. v. Klitzing, G. Dorda, and M. Pepper, Phys. Rev. Lett. **45**, 494 (1980).

[2] D. C. Tsui, H. L. Störmer, and A. C. Gossard, Phys. Rev. Lett. **48** 1559 (1982).

[3] *The Quantum Hall Effect*, edited by E. Prange and S. M. Girvin, (Springer Verlag, Berlin 1987).

[4] *Quantum Hall Effect*, edited by M. Stone, (World Scientific, Singapore 1992).

[5] T. Chakraborty and P. Pietiläinen, *The Fractional Quantum Hall Effect*, (Springer Verlag, Berlin 1997).

[6] T. Ando, A. B. Fowler, and F. Stern, Rev. Mod. Phys. **54**, 437 (1982).

[7] C. J. W. Beenakker and H. van Houten, Solid State Phys. **44**, 1 (1991).

[8] L. D. Landau and E. M. Lifshitz, *Quantum Mechanics, Non-Relativistic Theory*, (Pergamon, Oxford 1977).

[9] H. van Houten, B. J. van Wees, M. G. J. Heyman, and J. P. André, Appl. Phys. Lett. **49**, 1781 (1986).

[10] K. K. Choi, D. C. Tsui, and K. Alavi, Phys. Rev. B **36**, 7751 (1987); H. van Houten, C. W. J. Beenakker, B. J. van Wees, and J. E. Mooij, Surf. Sci. **196**, 144 (1988).

[11] H. Z. Zheng, H. P. Wei, D. C. Tsui, and G. Weimann, Phys. Rev. B **34**, 5635 (1986); T. J. Thornton et al., Phys. Rev. Lett. **56**, 1198 (1989).

[12] B. I. Halperin, Phys. Rev. B **25**, 2185 (1982).

[13] R. B. Laughlin, Phys. Rev. B **23**, 5632 (1981).

[14] R. Landauer, IBM J. Res. Dev. **1**, 223 (1957); *ibid* **32**, 306 (1988).

[15] M. Büttiker, Phys. Rev. Lett. **57**, 1761 (1986).

[16] C. W. J. Beenakker, Phys. Rev. Lett. **64**, 216 (1990).

[17] A. M. Chang, Solid State Commun. **74**, 871 (1990).

[18] D. B. Chklovskii, B. I. Shklovskii, and L. I. Glazman, Phys. Rev. B **46**, 4026 (1992).

[19] D. B. Chklovskii, K. A. Matveev, and B. I. Shklovskii, Phys. Rev. B **47**, 12605 (1993).

[20] J. Dempsey, B. Y. Gelfand, and B. I. Halperin, Phys. Rev. Lett. **70**, 3639 (1993).

[21] A. H. MacDonald, S. R. Eric Yang, and M. D. Johnson, Aust. J. Phys. **46**, 345 (1993).

[22] C. de C. Chamon and X. G. Wen, Phys. Rev. B **49**, 8227 (1994).

[23] O. Klein, C. de C. Chamon, D. Tang, D. M. Abusch-Magder, U. Meirav, X. G. Wen, M. A. Kastner, and S. J. Wind, Phys. Rev. Lett **74**, 785 (1995).

[24] T. H. Oosterkamp, J. Jansen, M. Danoesastro, and L. P. Kouwenhoven, preprint (1997).

[25] M. Ferconi and G. Vignale, Phys. Rev. B **50**, 14722 (1994); M. Ferconi, M. R. Geller, and G. Vignale, Phys. Rev. B **52**, 16357 (1995); M. Ferconi and G. Vignale, preprint (1997).

[26] O. Heinonen, M. I. Lubin, and M. D. Johnson Phys. Rev. Lett. **75**, 4110 (1995).

[27] T. H. Stoof and G. E. W. Bauer, Phys. Rev. B **52**, 12143 (1995); Solid State Electronics **40**, 349 (1996).

[28] M. A. Kastner, Rev. Mod. Phys. **64**, 849 (1992), and references therein.

[29] L. P. Kouwenhoven and P. L. McEuen, in *Nano-Science and Technology*, edited by G. Timp, (AIP Press, New York 1996) and references therein.

[30]   N. C. van der Vaart, S. F. Godijn, Yu. V. Nazarov, C. P. J. M. Harmans, J. E. Mooij, L. W. Molenkamp, and C. T. Foxon, Phys. Rev. Lett. **74**, 4702 (1995).

[31]   Yu. V. Nazarov, Physica B **189**, 57 (1993).

[32]   S. A. Gurvitz and Ya. S. Prager, Phys. Rev. B **53**, 15932 (1996).

[33]   A. Messiah, *Quantum mechanics*, (North-Holland, Amsterdam 1961).

[34]   L. P. Kouwenhoven, S. Jauhar, K. McCormick, D. Dixon, P. L. McEuen, Yu. V. Nazarov, N. C. van der Vaart, and C. T. Foxon, Phys. Rev. B **50**, 2019 (1994).

[35]   L. P. Kouwenhoven, S. Jauhar, J. Orenstein, P. L. McEuen, Y. Nagamune, J. Motohisa, and H. Sakaki, Phys. Rev. Lett. **73**, 3443 (1994).

[36]   Y. Nakamura, C. D. Chen, and J. S. Tsai, preprint.

[37]   T. H. Oosterkamp, L. P. Kouwenhoven, A. E. A. Koolen, N. C. van der Vaart, and C. J. P. M. Harmans, Phys. Rev. Lett. **78**, 1536 (1997).

[38]   B. J. Keay, S. J. Allen, Jr., J. Galán, K. L. Campman, A. C. Gossard, U. Bhattacharya, and M. J. W. Rodwell, Phys. Rev. Lett. **75**, 4098 (1995).

[39]   B. J. Keay, S. Zeuner, S. J. Allen, Jr., K. D. Maranowski, A. C. Gossard, U. Bhattacharya, and M. J. W. Rodwell, Phys. Rev. Lett. **75**, 4102 (1995).

[40]   T. Fujisawa and S. Tarucha, preprint.

[41]   P. K. Tien and J. P. Gordon, Phys. Rev. **129**, 647 (1963).

[42]   D. Sokolovski, Phys. Rev. B **37**, 4201 (1988); J. Phys. C: Solid State Phys. **21**, 639 (1988).

[43]   P. Johansson, Phys. Rev. B **41**, 9892 (1990).

[44]   M. Sumetskii, Phys. Lett. A **153**, 149 (1991).

[45]   M. Büttiker, A. Ptrêtre, and H. Thomas, Phys. Rev. Lett. **70** 4114 (1993).

[46]   N. S. Wingreen, A. P. Jauho, and Y. Meir, Phys. Rev. B **48**, 8487 (1993); Phys. Rev. B **50**, 5528 (1994).

[47]   C. Bruder and H. Schoeller, Phys. Rev. Lett. **72**, 1076 (1994).

[48]   Yu. Dakhnovskii and H. Metiu, Phys. Rev. B **4193** (1995).

[49]   T. H. Stoof and Yu. V. Nazarov, Phys. Rev. B **53**, 1050 (1996).

[50]   C. A. Stafford and N. S. Wingreen, Phys. Rev. Lett. **76**, 1916 (1996).

[51]   D. V. Averin and K. K. Likharev, in *Mesoscopic Phenomena in Solids*, edited by B. L. Altshuler, P. A. Lee, and R. A. Webb, (Elsevier, Amsterdam 1991).

[52]   C. Cohen-Tannoudji, J. Dupont-Roc, and G. Grynberg, *Atom-Photon Interactions*, (Wiley, New York 1992).

[53]   J. Bardeen, L. N. Cooper, and J. R. Schrieffer, Phys. Rev. **108**, 1175 (1957).

[54]   H. Kamerlingh Onnes, Leiden Comm. **120b, 122b, 124c** (1991).

[55]   A. F. Andreev, Sov. Phys. JETP **19**, 1228 (1964).

[56]   S. N. Artemenko, A. F. Volkov, and A. V. Zaitsev, JETP Lett. **28**, 589 (1978); Sov. Phys. JETP **49**, 924 (1979); Solid State Commun. **30**, 771 (1979).

[57]   A. V. Zaitsev, Sov. Phys. JETP **51**, 111 (1980).

[58]   G. E. Blonder, M. Tinkham, and T.M. Klapwijk, Phys. Rev. B **25**, 1415 (1982).

[59]   C. J. Lambert, J. Phys.: Condens. Matter, **3**, 6579 (1991).

[60]   C. W. J. Beenakker, Phys. Rev. B **46**, 12841 (1992).

[61]   H. Nakano and H. Takayanagi, Sol. St. Comm. **80**, 997 (1991).

[62]   F. W. J. Hekking and Yu. V. Nazarov, Phys. Rev. Lett. **71**, 1625 (1993).

[63]   A. V. Zaitsev, Phys. Lett. A **194**, 315 (1994).

[64] A. Kadigrobov, A. Zagoskin, R. I. Shekhter, and M. Jonson, Phys. Rev. B **52**, 8662 (1995).

[65] N. K. Allsopp, J. Sanchez Canizares, R. Raimondi, and C. J. Lambert, J. Phys.: Condens. Matter **8**, L377 (1996).

[66] Yu. V. Nazarov, Phys. Rev. Lett. **73**, 1420 (1994).

[67] A. Volkov, N. Allsopp, and C. J. Lambert, J. Phys.: Condens. Matter **8**, L45 (1996).

[68] Yu. V. Nazarov and T. H. Stoof, Phys. Rev. Lett. **76**, 823 (1996). T. H. Stoof and Yu. V. Nazarov, Phys. Rev. B **53**, 14496 (1996).

[69] P. G. N. de Vegvar, T. A. Fulton, W. H. Mallison, and R. E. Miller, Phys. Rev. Lett. **73**, 1416 (1994).

[70] H. Pothier, S. Guéron, D. Estève, and M. H. Devoret, Phys. Rev. Lett. **73**, 2488 (1994).

[71] A. Dimoulas, J. P. Heida, B. J. van Wees, T. M. Klapwijk, W. v.d. Graaf, and G. Borghs, Phys. Rev. Lett. **74**, 602 (1995).

[72] V. T. Petrashov, V. N. Antonov, P. Delsing and T. Claeson, Phys. Rev. Lett. **74**, 5268 (1995).

[73] S. G. den Hartog, C. M. A. Kapteyn, B. J. van Wees, T. M. Klapwijk, W. van de Graaf, and G. Borghs, Phys. Rev. Lett **76**, 4592 (1996).

[74] L. C. Mur, preprint (1997).

[75] G. Eilenberger, Z. Phys. **214**, 195 (1968).

[76] A. I. Larkin and Yu. V. Ovchinnikov, Sov. Phys. JETP **28**, 1200 (1969) [Zh. Eksp. Teor. Fiz. **55**, 2262 (1968)].

[77] L. V. Keldysh, Sov. Phys. JETP **20**, 1018 (1964) [Zh. Eksp. Teor. Fiz. **47**, 1515 (1964)].

[78] A. I. Larkin and Yu. V. Ovchinnikov, Sov. Phys. JETP **41**, 960 (1975) [Zh. Eksp. Teor. Fiz. **68**, 1915 (1975)]; Sov. Phys. JETP **46**, 155 (1977) [Zh. Eksp. Teor. Fiz. **73**, 299 (1977)].

[79] A. Schmid, in *Nonequilibrium Superconductivity, Phonons and Kapitza Boundaries* Proceedings of the NATO Advanced Study Institute, Acquafredda di Marathea, Italy (1980).

[80] J. Rammer and H. Smith, Rev. Mod. Phys. **58**, 323 (1986).

[81] L. P. Gorkov, Sov. Phys. JETP **7**, 505 (1958) [Zh. Eksp. Teor. Fiz. **34**, 735 (1958)].

[82] A. A. Abrikosov, L. P. Gorkov, and I. E. Dzyaloshinski, *Methods of Quantum Field Theory in Statistical Physics*, Dover, New York, (1963).

[83] G. M. Eliashberg, Sov. Phys. JETP **34**, 668 (1972) [Zh. Eksp. Teor. Fiz. **61**, 1254 (1971)].

[84] U. Eckern and A. Schmid, J. Low. Temp. Phys. **45**, 137 (1981).

[85] K. Usadel, Phys. Rev. Lett. **25**, 507 (1970).

[86] T. H. Stoof and Yu. V. Nazarov, Phys. Rev. B **54**, 772 (1996).

[87] D. Estève, H. Pothier, S. Guéron, N. O. Birge, and M. Devoret, in *Correlated Fermions and Transport in Mesoscopic Systems*, edited by T. Martin, G. Montambaux, and J. Trân Thanh Vân (Editions Frontières, Gif-sur-Yvette Cedex, France 1996).

[88] F. K. Wilhelm, A. D. Zaikin, and G. Schön, preprint.

[89] N. Argaman, Europhys. Lett. **38**, 231 (1997).

2

DENSITY-FUNCTIONAL THEORY OF QUANTUM WIRES AND DOTS IN A STRONG MAGNETIC FIELD

T. H. Stoof and G. E. W. Bauer

We study the competition between the exchange and the direct Coulomb interaction near the edge of a two-dimensional electron gas in a strong magnetic field using density-functional theory in a local approximation for the exchange-energy functional. Exchange is shown to play a significant role in reducing the spatial extent of the compressible edge channel regions obtained from an electrostatic description. The transition from the incompressible edge channels of the Hartree-Fock picture to the broad, compressible strips predicted by electrostatics occurs within a narrow and experimentally accessible range of confinement strengths.

2.1 INTRODUCTION

The concept of current-carrying edge channels accounts for the magnetotransport properties of a two-dimensional electron gas (2DEG) in a high magnetic field, both in the integer [1] and fractional [2, 3, 4] quantum Hall regime. Although the initial theoretical studies have used a noninteracting picture of edge channels, a considerable effort has recently been devoted to understand the effects of electron-electron interactions in the *integer* quantum Hall regime [2, 3, 4, 5, 6, 7, 8, 9].

At present there are two incompatible pictures for the electronic ground state of edge channels in the integer quantum Hall regime. In the Hartree-Fock approximation the ground state wave function is a single Slater determinant, which corresponds to occupation numbers zero and one [8]. In this description the edge state is incompressible and the electron density drops rapidly at the edges, on a length scale which is typically of the order of the magnetic length. Although the Hartree-Fock approximation is widely used for the description of quantum dots and wires [5, 8, 9], it has been challenged on the grounds that is does not take the global electrostatics into account properly [6, 7]. In the electrostatic description given in Ref. [6] a more gradual variation of the electron density at the edge is found energetically favorable. Here the typical length scale for the density drop at the edge is of the order of the depletion length, which is much larger than the magnetic length. In this picture the electrons at the edge can screen the electrostatic confinement potential by a slow density variation and the edge states are therefore compressible. However, this description completely neglects the exchange interaction.

A transition from incompressible to compressible edge states was already qualitatively discussed in Ref. [8], where a spontaneous transition from an unpolarized (e.g. equal occupation for both spin levels) to a polarized (different occupation for different spin levels) Hartree-Fock ground state was found for a critical confinement strength. It was speculated that a development to the electrostatic regime takes place as the confinement strength is decreased. More recently the transition between smoothly and abruptly varying density distributions has been studied by Chamon and Wen [9]. On the basis of few particle exact solutions they predict formation of compressible edge states when the strength of the confinement potential is reduced beyond a certain point. Their approach is difficult to extend to quantum wires or dots with a large number of electrons.

In the present work we interpolate between the different regimes of applicability of both Hartree-Fock and electrostatic pictures by extending the Thomas-Fermi approach used in Ref. [6] to a Thomas-Fermi-*Dirac* like treatment of the exchange effects in strong magnetic fields. First results of the present approach have been published in Ref. [10]. Very recently Ferconi and Vignale [11] have studied the ground state energies and densities of a quantum dot in an arbitrary magnetic field, taking into account exchange-correlation effects by employing a Kohn-Sham scheme of current-density functional theory [12]. For small quantum dots (2 or 3 electrons) their method yields an accuracy better than 3% when compared with exact results.

In Sec. 2.2 we describe our implementation of density-functional theory in strong magnetic fields as applied to quantum wires and derive expressions for the density profile and single-particle potentials of the ground state. In Sec. 2.3 we present results of the numerical calculations and we investigate both the accuracy of our theory and the relation with possible experiments. Two experimentally relevant applications are studied in Sec. 2.4; the

influence of a plane of constant potential parallel to the 2DEG on the electronic ground state and the ground state properties of a quantum dot in a strong magnetic field. Section 2.5 summarizes our conclusions.

2.2 DENSITY-FUNCTIONAL THEORY IN A STRONG MAGNETIC FIELD

2.2.1 THE SYSTEM

Let us consider first a quantum wire of the strictly two dimensional electron gas along the y axis in the xy plane (Fig. 2.1). Perpendicular to the plane a strong uniform magnetic
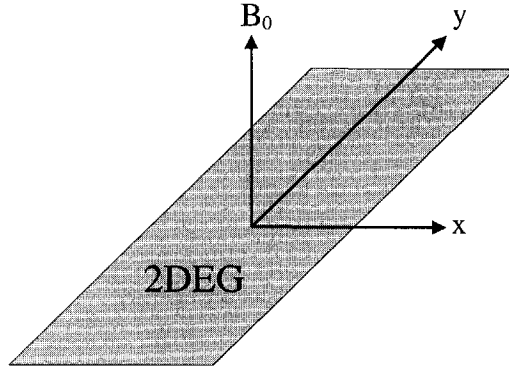
Figure 2.1: *Schematic picture of the system, consisting of a strip of 2DEG in a uniform magnetic field. The wire is confined by a parabolic potential in the x-direction. For details see text.*

field is applied. Also present is a uniform positive background charge which ensures global neutrality. We use periodic boundary conditions in the y-direction and adopt the Landau gauge so that $\mathbf{A}_0 = B_0 x \hat{\mathbf{y}}$ and $\mathbf{B}_0 = B_0 \hat{\mathbf{z}}$. In the high magnetic field limit considered here only the lowest (spin-up and spin-down) Landau levels are occupied.

The wire is confined in the x direction by a parabolic confinement potential:

$$V_{\mathrm{c}}(x) \;=\; \alpha \, \frac{e}{4\pi\epsilon l_B} \, x^2, \tag{2.1}$$

where $\epsilon = \epsilon_0 \epsilon_r$ is the dielectric constant and α is a dimensionless parameter. We will ignore here the difference between the 'bare' magnetic length $l_B = \sqrt{\hbar/eB_0}$ and the magnetic length l which is renormalized by the parabolic confinement potential:

$$l = l_B \sqrt{\frac{\omega_c^2}{\omega_c^2 + \omega_0^2}}, \tag{2.2}$$

where $\omega_c = eB_0/m^*$ is the cyclotron frequency with m^* the effective electron mass and ω_0 characterizes the parabolic confinement potential $\frac{1}{2}m^*\omega_0^2 x^2$. Since we treat the problem

numerically, the assumption of a parabolic form for the confinement is not essential: It is chosen here because it is widely used in the literature. All lengths will be given in units of l_B throughout the chapter unless otherwise indicated.

2.2.2 THEORY

We use density-functional theory in strong magnetic fields to find the electronic ground state of the system [12]. Without a magnetic field, the total energy of the system would be a functional of the electron density only. However, a magnetic field, apart from giving rise to Zeeman splitting, causes orbital currents to flow in the electron gas, even when the system is in thermodynamic equilibrium. As a consequence, the total energy is now a functional of the density $n(\mathbf{r})$, the spin density $\mathbf{s}(\mathbf{r})$ and the paramagnetic current density $\mathbf{j}_p(\mathbf{r})$ [12].

We do not take into account correlation effects, which means that we operate strictly in the integer quantum Hall regime, since correlation is responsible for the energy gaps that cause the fractional quantization. Due to the fact that the correlation part of the energy is disregarded and exchange does not depend on the current density the total energy functional depends only on the total and the spin density or equivalently, since the spin-quantization axis is well defined by the strong magnetic field, on the density of spin up and spin down electrons.

In the Kohn-Sham scheme of density-functional theory the ground state densities n^σ of the interacting electron system are expressed in terms of a set of M^σ Kohn-Sham orbitals $\phi_i^\sigma(\mathbf{r})$:

$$n^\sigma(\mathbf{r}) = \sum_{i=1}^{M^\sigma} |\phi_i^\sigma(\mathbf{r})|^2, \tag{2.3}$$

where $\sigma = \uparrow, \downarrow$ denotes up or down spin respectively and M^σ is the number of electrons with spin σ. These orbitals satisfy the Kohn-Sham equations:

$$\left\{ \frac{-\hbar^2}{2m^*} \nabla^2 + V_{\text{eff}}^\sigma(\mathbf{r}) \right\} \phi_i^\sigma(\mathbf{r}) = \epsilon_i^\sigma \phi_i^\sigma(\mathbf{r}), \tag{2.4}$$

with $V_{\text{eff}}^\sigma(\mathbf{r})$ the effective one-particle potential:

$$V_{\text{eff}}^\sigma(\mathbf{r}) = V_c(\mathbf{r}) + V_H([n]; \mathbf{r}) + V_x^\sigma([n^\uparrow, n^\downarrow]; \mathbf{r}), \tag{2.5}$$

where V_H is the Hartree potential and V_x^σ the exchange potential. Here we have disregarded the exchange-correlation vector potential $\mathbf{A}_{xc}$ which gives only a very small contribution to the total energy [11]. The Kohn-Sham ground state wave function is a Slater determinant of the M^σ lowest Kohn-Sham orbitals:

$$\Phi^\sigma(\mathbf{r}_1, \mathbf{r}_2, ..., \mathbf{r}_{M^\sigma}) = \frac{1}{\sqrt{M^\sigma}} \det \left\{ \phi_j^\sigma(\mathbf{r}_i) \right\}. \tag{2.6}$$

It can be shown (see Sec. 2.3.2) that in the limit of high magnetic fields the mixing between Landau level wave functions vanishes. Consider, e.g., the case of a single occupied, spin resolved Landau level. For large magnetic fields the Kohn-Sham ground state wave function, Eq. (2.6), reduces to a Slater determinant of lowest Landau level wave functions

with integer filling. As a consequence the scheme cannot describe fractional filling in the extreme quantum limit we are interested in. The reason for the failure of this procedure is the fact that the crucial assumption of the Kohn-Sham scheme, namely that the interacting v-representable densities are also non-interacting v-representable [13], breaks down in the high magnetic field limit. Note that this is only the case for T=0 and that the Kohn-Sham scheme at finite temperatures is in fact able to reproduce smoothly varying densities [14].

It is not possible to extend the (T=0) Kohn-Sham scheme to fractional filling factors since in that case the effective potential, $V_{\text{eff}}^{\sigma}(\mathbf{r})$, is no longer a unique functional of the total and spin density. However, at sufficiently high magnetic fields the basis wave functions are known to be just Landau level wave functions. We may then use a variational scheme which allows fractional filling and in which $E[n^{\uparrow}, n^{\downarrow}]$ is a unique functional of the total and spin density.

The equilibrium density distribution $n(x) = n^{\uparrow}(x) + n^{\downarrow}(x)$ which minimizes the total energy E of the system can be found by solving:

$$\frac{\delta E[n^{\uparrow}, n^{\downarrow}]}{\delta n^{\uparrow}(x)} = \frac{\delta E[n^{\uparrow}, n^{\downarrow}]}{\delta n^{\downarrow}(x)} = \mu, \tag{2.7}$$

where μ is the chemical potential and the total energy of the quantum wire is given by:

$$E[n^{\uparrow}, n^{\downarrow}] = T[n] + E_{\text{c}}[n] + E_{\text{H}}[n] + E_{\text{Z}}[n^{\uparrow}, n^{\downarrow}] + E_{\text{x}}[n^{\uparrow}, n^{\downarrow}]. \tag{2.8}$$

The total energy, Eq. (2.8), consists of five contributions: The first term on the right hand side is the kinetic energy which we define as a functional of the total density:

$$T[n] = \sum_{N\sigma} \int_{-\infty}^{\infty} dx \, n_N^{\sigma}(x) \, (N + \frac{1}{2}) \hbar\omega_{\text{c}}, \tag{2.9}$$

where N labels the Landau levels. The densities $n_N^{\sigma}(x)$ are the partial densities for a given spin direction σ and Landau level N. The total electron density is found by summing over all occupied Landau levels and over spin directions: $n(x) = \sum_{N\sigma} n_N^{\sigma}(x)$ and is for sufficiently high magnetic fields given by:

$$n(x) = \sum_{\sigma NX} \nu_{NX}^{\sigma} |\psi_{NX}(x,y)|^2, \tag{2.10}$$

where $X \equiv k_y l_B^2$ is the quantum number of an electron with momentum $\hbar k_y$, the amplitudes $\psi_{NX}(x,y) \sim \phi_{NX}(x) \exp(iXy/l_B^2)$ are the single particle bulk Landau level wave functions and ν_{NX}^{σ} is the local filling factor for electrons with spin σ in Landau level N. For well behaved confinement potentials the partial densities can be deduced from the total densities $n^{\uparrow}$ and $n^{\downarrow}$. For these potentials the total filling factor for a given spin direction, $\nu^{\sigma}(x)$, lying between $N_{\max} - 1$ and $N_{\max}$, always consists of $N_{\max} - 1$ completely filled Landau levels and a partially filled one. This means that the kinetic energy (and also the exchange energy, see Eqs. (2.15) and (2.16)) is still a functional of the *total* and not the partial densities.

The second contribution is the confinement energy which is given by:

$$E_{\text{c}}[n] = \int_{-\infty}^{\infty} dx \, n(x) \, eV_{\text{c}}(x). \tag{2.11}$$

The electrostatic Hartree energy is:

$$E_{\mathrm{H}}[n] = \int_{-\infty}^{\infty} dx \; n(x) \; eV_{\mathrm{H}}[n], \tag{2.12}$$

where the Hartree potential, $V_{\mathrm{H}}[n]$, is itself a functional of the total density. For the strictly two dimensional electron gas (See Ref. [15] for the case of a quasi-two dimensional electron gas) it is given by:

$$V_{\mathrm{H}}[n] = -\frac{e}{2\pi\epsilon l_B} \int_{-\infty}^{\infty} dx' \; n(x') \; \ln|x - x'|. \tag{2.13}$$

The fourth term denotes the Zeeman energy:

$$E_{\mathrm{Z}}[n^{\uparrow}, n^{\downarrow}] = \frac{1}{2} g\mu_B B_0 \int_{-\infty}^{\infty} dx \left\{ n^{\uparrow}(x) - n^{\downarrow}(x) \right\}, \tag{2.14}$$

where g is the bare Landé factor.

Our only concern left is the explicit form of the last term in Eq. (2.8), which is the exchange-energy functional. In the local density approximation (LDA) it reads:

$$E_{\mathrm{x}}[n^{\uparrow}, n^{\downarrow}] = \int_{-\infty}^{\infty} dx \left\{ n^{\uparrow}(x) \; \epsilon_{\mathrm{x}}(n^{\uparrow}(x)) + n^{\downarrow}(x) \; \epsilon_{\mathrm{x}}(n^{\downarrow}(x)) \right\}. \tag{2.15}$$

Here ϵ_{x} denotes the one-particle exchange energy of the homogeneous 2DEG with ground state densities $n^{\uparrow}$ and $n^{\downarrow}$, which is magnetic field dependent: In the absence of a magnetic field, it is proportional to $\sqrt{n}$ [16], but in the magnetic quantum limit considered here, the local exchange energy per electron is:

$$\epsilon_{\mathrm{x}}(n^{\sigma}(x)) = -\frac{e^2}{4\pi\epsilon l_B} \sum_{NN'} c_{NN'} \; n_{N'}^{\sigma}(x), \tag{2.16}$$

where the coefficients $c_{NN'}$ describe the exchange coupling between Landau levels N and N'. They can be found by calculating the exchange energy per particle of an extended N Landau level system [17]. For two occupied levels, e.g., they are $c_{00} = \sqrt{2\pi^3}$, $c_{01} = c_{10} = \sqrt{\pi^3/2}$ and $c_{11} = \sqrt{9\pi^3/8}$.

The local density approximation is clearly only justified when the density variations are small on a characteristic length scale, which in our case is the magnetic length. In practice, however, it often turns out to be a useful and accurate tool even in cases in which this condition is not met [13].

Because we expect the results for higher Landau levels to be qualitatively the same, we will in the following restrict ourselves to the magnetic quantum limit, for which only the lowest Landau level is occupied. In the space of the lowest (spin-polarized) Landau level, the kinetic energy per particle is constant and may be disregarded. The validity of this approximation is discussed in Sec. 2.3.2. The density is in this case given by:

$$n(x) = \frac{1}{2\sqrt{\pi^3}} \sum_{\sigma} \int_{-\infty}^{\infty} dX \; \nu^{\sigma}(X) \; e^{-(x-X)^2}, \tag{2.17}$$

where we have replaced the sum over X in Eq. (2.10) by an integral and substituted the lowest Landau level wave functions. This relation shows that in the extreme quantum limit

there exists a one to one correspondence between the density and the filling factor which enables us to use the latter as the variational function in the determination of the ground state of the system (see Sec. 2.3.1).

The exchange energy per electron in the lowest Landau level ($N = N' = 0$) reduces to:

$$\epsilon_x(n^\sigma) = -\sqrt{2\pi^3} \, \frac{e^2}{4\pi\epsilon l_B} \, n^\sigma(x), \qquad (2.18)$$

e.g. the one-particle exchange energy for a given spin direction is just proportional to the corresponding electron density.

On substituting Eqs. (2.13), (2.17) and (2.18) in Eq. (2.8) for the total energy and performing the functional derivatives, Eqs. (2.7) become:

$$\frac{\delta E[n^\uparrow, n^\downarrow]}{\delta n^\uparrow(x)} = eV_c(x) + eV_H[n] + 2\epsilon_x[n^\uparrow] + \frac{1}{2}g\mu_B B_0 = \mu, \qquad (2.19)$$

$$\frac{\delta E[n^\uparrow, n^\downarrow]}{\delta n^\downarrow(x)} = eV_c(x) + eV_H[n] + 2\epsilon_x[n^\downarrow] - \frac{1}{2}g\mu_B B_0 = \mu. \qquad (2.20)$$

The numerical treatment of these coupled equations and the results will be presented in the next section.

2.3 CALCULATION OF GROUND STATE PROPERTIES

2.3.1 RESULTS

As described above we obtain the ground state occupation numbers by numerically minimizing the total energy with respect to the filling factors, while keeping the total number of electrons constant. We discretize the filling factor and impose the boundary conditions: $0 \leq \nu^\sigma \leq 1$. The numerical algorithm that minimizes the total energy uses a sequential quadratic programming method and is very stable. Numerical integration of the singular integrand in Eq. (2.13) requires some care. By sampling the integrand equidistantly and symmetrically around the divergence, $x = x'$, and by sampling enough points to avoid oscillatory behavior in the resulting integral. An advantage of the present numerical scheme is that it can be very easy generalized to different confinement potentials. It should be noted, however, that the choice of confinement potential is not completely arbitrary. For e.g. a hard wall potential there is a stronger mixing with higher Landau levels near the edges and for such a confinement Eqs. (2.17) and (2.18) may be no longer accurate.

With the approach outlined above we can obtain, to a very good approximation, both the electrostatic solution (by neglecting the exchange term) and the Hartree-Fock solution as calculated by Dempsey *et al.* [8] (by forcing the filling factors to be integer valued). Therefore we expect our approach to give a good description of the intermediate regime between these two extremes.

In Fig. 2.2 ground state occupation numbers obtained with different methods are plotted as a function of the confinement strength α. Fig. 2.2 (a) shows the purely electrostatic solution, the Hartree-Fock solution is plotted in Fig. 2.2 (b) and the solution including exchange in the local density approximation is shown in Fig. 2.2 (c). The small incompressible regions found in the electrostatic solution are caused by Zeeman splitting.

(a)

(b)

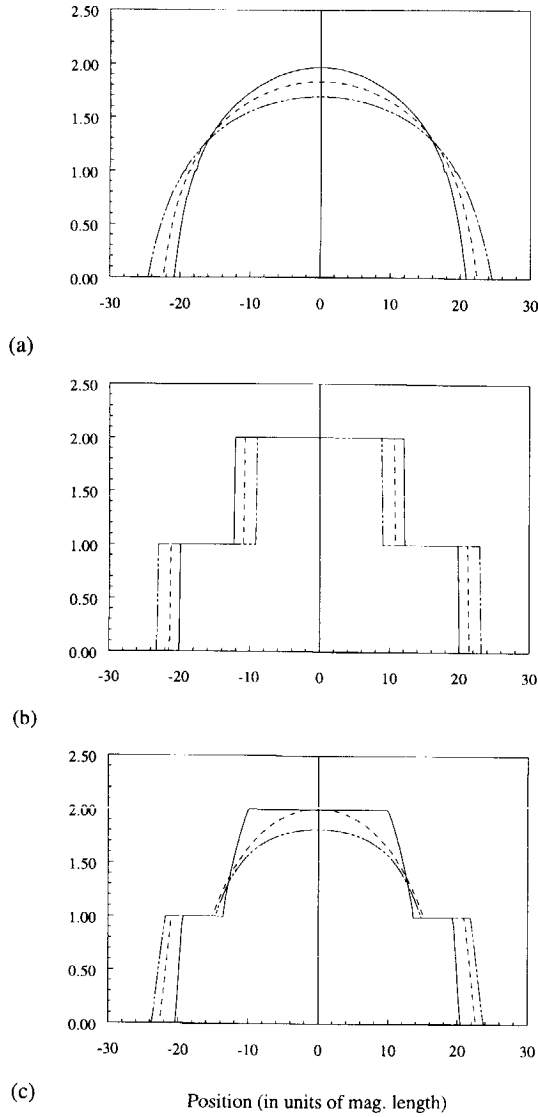(c)   Position (in units of mag. length)

Figure 2.2: *Electronic ground state filling factors, (a) ignoring exchange and in-cluding exchange in (b) the Hartree-Fock approximation and (c) the local density approximation. The filling factors are plotted for confinement strengths $\alpha = 0.047$ (solid line), 0.041 (dashed line) and 0.035 (dashed-dotted line). Calculated for a magnetic field of 7.2 T.*

The calculations were performed using a magnetic field of 7.2 T which for filling factor $\nu = 2$ in the bulk corresponds to a zero-field bulk density of 3.5×10^{11} cm^{-2}. For GaAs the static dielectric constant $\epsilon_r = 12.5$ and the bare Landé factor $|g| = 0.44$. The filling factors are plotted for a constant number of electrons and confinement strengths $\alpha = 0.035, 0.041$ and 0.047 respectively. Converted to energy level spacings of a parabolic confinement potential of the form: $\frac{1}{2}m^*\omega_0^2 x^2$ these values correspond to $\hbar\omega_0 = 3.4$ meV, 3.8 meV and 4.1 meV respectively.

As can be seen from Fig. 2.2 (c) the effect of exchange on the electrostatic solution is a reduction of the compressible regions because it favors integer filling. However, a comparison with Fig. 2.2 (b) shows that for soft confinement potentials the Hartree-Fock approximation no longer holds, e.g. the electrostatic interaction overcomes the tendency of exchange to form an incompressible ground state. Note, however, that the solution for $\alpha = 0.047$ in Fig. 2.2 (c) is almost identical to the corresponding Hartree-Fock solution shown in Fig. 2.2 (b), which shows that for confinement potentials that are strong enough the solution is forced into the integer filling regime, in agreement with the qualitative picture given in Ref. [8]. Note that this transition from incompressible to compressible state is a genuine correlation effect since it corresponds to the mixing of different single-determinant configurations, in spite of our exchange-only potential.

It is clear from Fig. 2.2 (c) that the width of the incompressible region is of the same order of magnitude as the width of the outermost compressible strip, even for the relatively wide strips we consider here (approximately 420 nm for a magnetic field of 7.2 T). This in contrast to the electrostatic description of edge states shown in Fig. 2.2 (a), where the width of the incompressible region is always much smaller than that of the compressible one. However, for soft confinement potentials the solution including exchange does not deviate dramatically from the purely electrostatic one, which obviously implies that the Hartree-Fock approach breaks down in this regime. Only a strong confinement potential can cause incompressible edge channels, although in Fig. 2.2 (c) the confinement is still not strong enough to reduce the splitting to that of the bare Zeeman splitting. In the case of even harder confinement ($\alpha \approx 0.073$, e.g. $\hbar\omega_0 \approx 5.3$ meV) we find that the splitting indeed reduces to this minimum value (not shown).

Note that the entire range from the electrostatic to the (unpolarized) Hartree-Fock regime can be realized in realistic confinement potentials with $\hbar\omega_0$ ranging from 3.4 meV to 5.3 meV. Confinement potentials with level spacings of a few meV have been realized [18, 19] so it should be possible to test these results by experiments. A possible method to stiffen the confinement experimentally is fabricating the 2DEG closer to the surface of the AlGaAs/GaAs heterostructure.

In essence, our method to include exchange is using an position dependent g-factor that depends on the local density. A simple approximation to this method would be to use the enhanced g-factor corresponding to a single occupied spin level [20]. This method does increase the width of the incompressible strip but in general does not reproduce the qualitative and quantitative features obtained with our method [21].

In Fig. 2.3 the calculated one-particle potentials in the wire are plotted for both spin directions. These potentials correspond to the ground state density distribution of Fig. 2.2 (c) with $\alpha = 0.035$ which is also included in the figure. Fig. 2.3 (a) shows the electrostatic potential, which consists of the Hartree and confinement potential. Also plotted are the exchange potential and the total potential for the majority-spin electrons, e.g. electrons occupying
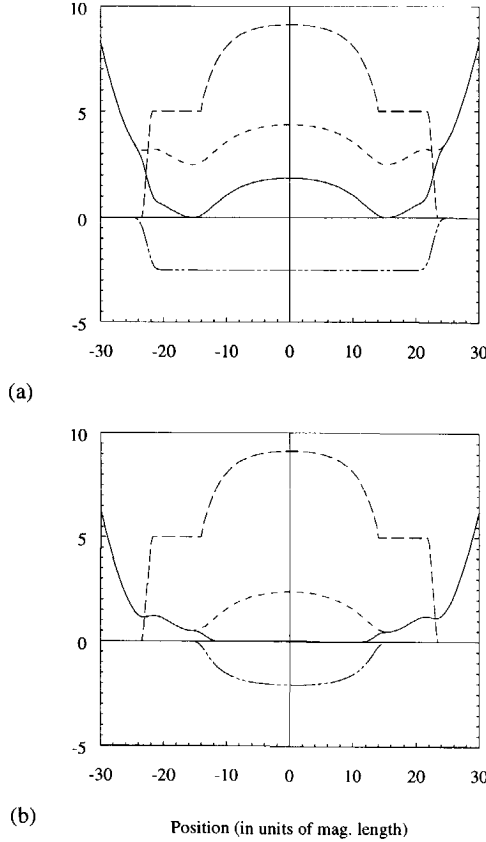
(a)

(b)

Position (in units of mag. length)

Figure 2.3: *One-particle potentials and density distribution for the ground state of Fig. 2(c) with $\alpha = 0.035$ for (a) majority-spin electrons and (b) minority-spin electrons. Plotted are the electrostatic potential consisting of the confinement and the Hartree potential (dashed line), the exchange potential (dashed-dotted line) and the total potential excluding the Zeeman term (solid line). In the regions where the exchange potential is zero the total and Hartree potential coincide. The potentials are offset for clarity and are given in units of $\frac{e}{4\pi\epsilon l_B}$.*

the lowest spin level. In Fig. 2.3 (b) the same can be seen for the minority-spin electrons. In the figures the constant Zeeman term has been omitted for simplicity so that the total potential is just the sum of the electrostatic and exchange potential.

Fig. 2.3 (a) shows that for a majority spin electron the energetically most favorable position is near the edges. This is because these electrons are forced by exchange to form an electrostatically unfavorable density profile in which no screening of the confinement potential is possible, e.g. the density of majority spin electrons is constant in the bulk of

the wire. This in contrast to the minority spin electrons, for which the potential in the bulk is flat. This is due to the fact that these electrons still have the freedom to form a density distribution which can screen the external potential without being influenced much by the exchange interaction.

The typical voltage drop from the edge to the middle of the wire has experimentally realistic values of ≈ 300 mV for the bare confinement potential and ≈ 30 mV for the selfconsistent potential.

We also performed calculations of the widths of compressible and incompressible regions as a function of the confinement strength. The results are visible in Fig. 2.4 where the widths of the outermost incompressible region (I) and innermost compressible region (C) have been plotted as a function of α. If no incompressible strip is present in the middle of the wire, C
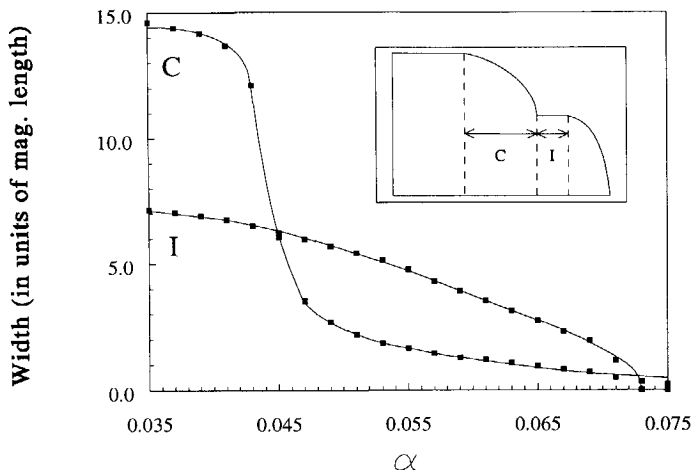

Figure 2.4: *Width of innermost compressible region (C) and outermost incompressible region (I) (see inset), plotted as a function of the confinement strength α. The solid lines are drawn as a guide for the eye.*

is defined as half the width of the total compressible middle region (see inset). In the figure the points do not always lie on the smooth curve which serves as a guide for the eye. This is due to the spacing between sampling points $(0.2 \, l_B)$, which imposes a upper bound on the accuracy of the calculated widths.

The compressible strip shrinks rapidly as the confinement is increased but if the width has reached a value of roughly a few magnetic lengths, the further decrease becomes very slow and in practice we always find a small but finite compressible region. It is clear, however, that a Hartree-Fock treatment should give good results for hard confinements where small compressible regions exist. We recover the spin-polarizing transition of Ref. [8] since the incompressible strip between spin-up and spin-down channels (I in Fig. 2.4) drops to zero at a certain critical value of the confinement strength (neglecting Zeeman splitting). Both the value for the critical confinement strength and the overall shape of the curve agree well with the results of Ref. [8].

An important consequence of exchange on the distribution of electrons for experiments

is the increased separation between the compressible regions. This causes a strong decrease in inter-edge channel scattering because of the reduced overlap of the edge-channel wave functions, which leads to an increase in the spin-flip equilibration length of the edge channels. This in contrast to the assumption of an edge channel separation of the order of one magnetic length in Ref. [22]. Using a typical edge channel separation of a few magnetic lengths in accordance with the present results, Khaetskii's theory [22] would give a much longer equilibration length.

The exchange enhanced channel separation has also consequences for the two-terminal magnetoconductance of a narrow channel or point contact. In Ref. [7], Chklovskii *et al.* discuss the conductance for these systems in the framework of their electrostatic description of the channels. They obtain conductance quantization but, due to the small width of the incompressible regions, the calculated plateau widths are much smaller than those experimentally observed. They attribute this discrepancy between theory and experiment to the presence of disorder. However, we propose as an alternative explanation the electronic exchange interaction which we find to strongly enhance the width of the insulating strips.

2.3.2 ACCURACY

In this subsection we study the accuracy of our theory and how our present results are altered if we take into account realistic features which do not change the qualitative results but are important to describe experimental situations.

First we investigate the validity of Eq. (2.17) for high magnetic fields where mixing with higher Landau levels was disregarded. To this end we use a parabolic confinement $\frac{1}{2}m^*\omega_0^2 x^2$ and a density distribution of the form: $n(x) = \frac{1}{2\pi l^2}\theta(x - W/2)\theta(x + W/2)$, where W is the width of the wire. The 2DEG in the presence of the uniform magnetic field and parabolic confinement potential is our unperturbed system and we treat the Hartree potential as a perturbation. The energy levels of the unperturbed system are $E_{nk} = (n + \frac{1}{2})\hbar\Omega + \hbar^2 k_y^2/2M$, where $\Omega = \sqrt{\omega_c^2 + \omega_0^2}$ is the renormalized cyclotron frequency and M is the renormalized electron mass: $M = m^*(1 + \omega_c^2/\omega_0^2)$. The wave functions are the bulk Landau level wave functions with effective magnetic length $l = l_B\sqrt{\omega_c^2/(\omega_c^2 + \omega_0^2)}$ [17]. According to first order perturbation theory, the ground state wave function, $|\psi\rangle$, of the electron at the edge, with quantum number $X = W/2$, is approximately:

$$|\psi\rangle = |\psi_0\rangle + \frac{\langle\psi_1| eV_H |\psi_0\rangle}{E_0 - E_1}|\psi_1\rangle, \qquad (2.21)$$

where we have used the Hartree potential as the perturbation. A straightforward calculation of the coefficient of $|\psi_1\rangle$ (which of course depends on W) shows that for $20\,l_B \leq W \leq 40\,l_B$, a magnetic field of 5 T and a typical value of $\hbar\omega_0 = 3$ meV for the parabolic confinement, the mixing with the first Landau level wave function is approximately 10% and that this value decreases as $1/\sqrt{B_0}$ with increasing magnetic field. We have to conclude that the dip in the electrostatic, e.g. Hartree and confinement, potential at the edges which is responsible for the spin-polarizing transition and ultimately for the compressible edge state, cannot be compensated by mixing with higher Landau levels, e.g. that our approximation is allowed in the high magnetic field limit considered here. By performing a similar calculation it is possible to show that the mixing due the exchange-correlation potential used by Ferconi and Vignale [11] is only a few percent.

Another approximation which gives rise to quantitative deviations from our theory is the assumption that the electron gas is strictly two dimensional. In reality the electron wave functions also extend in the z-direction and a form factor $F(q)$ in the Coulomb interaction, $V(q) = e^2 F(q)/2\epsilon|q|$, takes this effect into account. Calculations of edge channel splitting including a form factor in the Hartree-Fock approximation have already been calculated by Rijkels and Bauer [15]. By comparison with Ref. [15] we estimate the values of α to decrease by about 0.004 if a form factor would be included into our calculations. This shifts the range of $\hbar\omega_0$ in which both the electrostatic and the Hartree-Fock regime are unreliable to lower energies, e.i. to 3.2 meV-5.1 meV.

2.4 APPLICATIONS

The present theory can be easily generalized to a variety of systems. In the next subsections we consider two special cases, which are experimentally relevant.

2.4.1 BACK GATE

As a first application we have carried out calculations for a system like the one considered in Sec. 2.2.1, but now in the presence of an infinite plane of constant potential at a distance d from the 2DEG, which may represent a real back gate or a plane of not fully depleted donors parallel to the 2DEG. This gate can be easily included into the calculations by adding the potential of a mirror charge distribution of opposite sign located at a distance $2d$ from the electron gas:

$$V_{\mathrm{bg}}(x) = \frac{e}{2\pi\epsilon l_B} \int_{-\infty}^{\infty} dx' \, n(x') \, \ln\sqrt{(x-x')^2 + (2d)^2}. \qquad (2.22)$$

In Fig. 2.5 we have plotted the solutions that minimize the total energy of the system including the back gate as a function of the distance d to the wire for a given number of electrons and a fixed confinement potential.

It is clear from the figure that moving the back gate closer to the 2DEG has the effect of reducing the width of the compressible regions. This is to be expected because the back gate screens the long-range Coulomb interaction in the electron gas, thus effectively reducing the importance of the direct interaction relative to the exchange interaction and thereby forcing the solution for small distances d into the Hartree-Fock regime.

It should be noted that the description of the back gate given here does not apply for a quantum wire defined by a depletion gate. In that case the back gate would also screen the charge on the depletion gates, thus increasingly altering the confinement potential as the back gate is moved closer to the 2DEG. In that case a fully self-consistent calculation is necessary. Furthermore, for our results to be correct, the distance from the gate to the 2DEG should not be too small since in that case also the short-range exchange interaction would be influenced by the gate.

2.4.2 GROUND STATE OF A QUANTUM DOT

A system that is very similar to the strip previously considered is a quantum dot in a high magnetic field, especially when the number of electrons in the dot is large. There are two
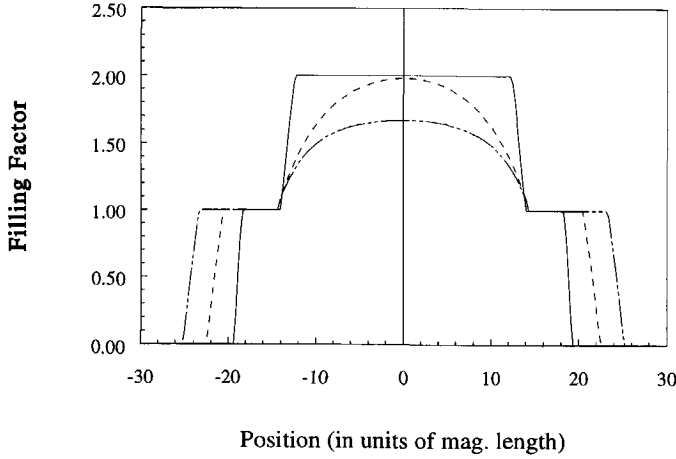
Position (in units of mag. length)

Figure 2.5: *Occupation of the system in the presence of the back gate at a distance $d = \infty$ (dashed-dotted line), $d = 20l_B$ (dashed line) and $d = 10l_B$. The confinement strength $\alpha = 0.035$ and $B = 7.2$ T. (solid line).*

main differences. In the first place we use the symmetric gauge to describe the dot. In this gauge the wave functions in the lowest Landau level, labeled by the quantum number of angular momentum, are $\phi_m(z) = \frac{1}{\sqrt{2\pi}} \frac{z^m}{\sqrt{m!}} e^{-|z|^2/2}$ where $z = \frac{x+iy}{\sqrt{2}}$. The second difference is that because the system is finite the filling factor ν is no longer labeled by the continuous variable X but by the discrete quantum number m. As a consequence the radial symmetric density is now given by:

$$n(r) = \frac{1}{2\pi} \sum_{m\sigma} \frac{\nu_m^\sigma}{m!} \, \exp\left(-\frac{r^2}{2}\right) \left(\frac{r^2}{2}\right)^m, \tag{2.23}$$

where ν_m^σ is the filling factor for a given angular momentum m and spin direction σ. We impose as boundary conditions that $0 \leq \nu_m^\sigma \leq 1$ and that the total charge in one spin level $\sum_m \nu_m^\sigma$ is an integer. Due to the circular symmetry of the dot the Hartree potential is in this case given by:

$$V_{\mathrm{H}}(r) = -\frac{e}{4\pi\epsilon l_B} \int_0^{2\pi} d\phi \int_0^\infty dr' \frac{r'n(r')}{\sqrt{r^2 + r'^2 - 2rr'\cos\phi}}. \tag{2.24}$$

An analysis analogous to the one presented in Sec. 2.3.2 shows that for high magnetic fields (approximately 5 T) the mixing with higher Landau levels due to the Hartree potential and the exchange-correlation potentials used in Ref. [11] is only a few percent. As a consequence, fractional occupation numbers are essential, which cannot be described by the Kohn-Sham scheme of Ref. [11].

We have calculated the ground state of a dot consisting of 40 electrons using a parabolic confinement potential $V_c(r) = \alpha \frac{e}{4\pi\epsilon l_B} r^2$ with varying strength α in a magnetic field of
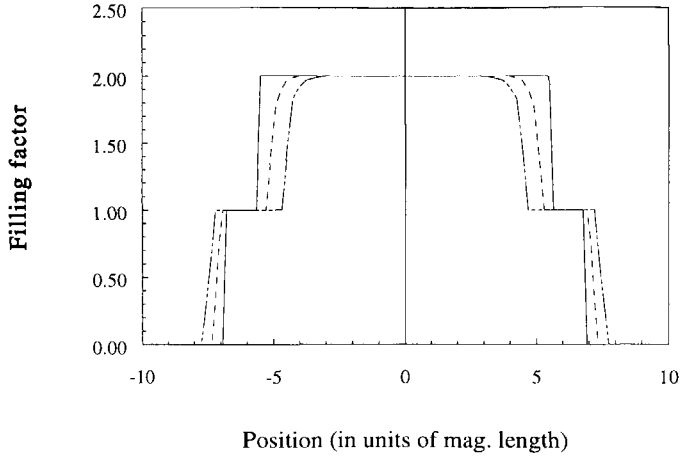
Position (in units of mag. length)

Figure 2.6: *Occupation numbers of a quantum dot consisting of* 40 *electrons for confinement strengths* $\alpha = 0.09$ *(solid line),* 0.08 *(dashed line) and* 0.07 *(dashed-dotted line). The discrete filling factors are positioned at the radii* r_m *and have been connected by lines for clarity.*

5.0 T. To find the ground state for a given magnetic field we vary the distribution of electrons among the occupied spin levels while keeping the total number of electrons constant. The results are plotted in Fig. 2.6. The ground states are similar to those of the strip except for the fact that the middle region is wider. This is due to the fact that the wave functions are centered around the radii $r_m = \sqrt{2m}\, l_B$, where m is the angular momentum index, and not around equidistant points like in the strip.

In Ref. [18] a selfconsistent calculation was performed for the density profile of a quantum dot containing 39 electrons using a modified Hartree form for the electrostatic electron-electron interaction:

$$V_{\text{ee}}(\mathbf{r}, \mathbf{r}') = -\frac{e}{4\pi \epsilon l} \left\{ \frac{1}{\sqrt{|\mathbf{r} - \mathbf{r}'|^2 + \langle \delta z \rangle^2}} - \frac{1}{\sqrt{|\mathbf{r} - \mathbf{r}'|^2 + 4d^2}} \right\}, \tag{2.25}$$

thus taking into account the finite z-extent $\langle \delta z \rangle$ of the wave functions and a back gate at distance d. Again we want to extend these calculations to include exchange but we must keep in mind that a finite $\langle \delta z \rangle$ also reduces the exchange interaction by a form factor:

$$F(\langle \delta z \rangle) = \exp\left(\frac{1}{2}\langle \delta z \rangle^2\right) \text{Erfc}\left(\frac{\langle \delta z \rangle}{\sqrt{2}}\right), \tag{2.26}$$

where $\langle \delta z \rangle$ is given in units of the magnetic length and $\text{Erfc}(x) = 1 - \text{Erf}(x)$ denotes the complementary error function. A calculation using interaction Eq. (2.25) and the local exchange contribution reduced by the form factor Eq. (2.26) gives a ground state which differs from that of McEuen *et al.* in the sense that the widths of the incompressible (compressible) regions are larger (smaller) in our solution.

We have calculated the addition spectrum of dots consisting of 37 and 38 electrons in order to determine the effect of exchange on the inter-level transitions that are responsible for the oscillatory behavior of the addition energy. Here we take into account the fact that the magnetic length is renormalised by the magnetic field, Eq. (2.2), in order to compare the energies at different magnetic fields. The addition energy $\Delta E(N)$ needed for adding an extra electron to a dot of N electrons is:

$$\Delta E(N) = E(N+1) - E(N), \tag{2.27}$$

where $E(N)$ is the total energy given by Eq. (2.8). The results are depicted in Fig. 2.7. It should be mentioned that our results are very close to the Hartree-Fock solutions. This is due to the fact that the combination of the back gate and exchange force the solution into the integer filling regime.

The inset of Fig. 2.7 shows the energy dependence of different dot configurations with magnetic field for a dot containing 39 electrons. The ground state is formed by the configuration with lowest energy. The numbers in the inset represent the number of electrons in the majority (e.g. lowest) spin level for the indicated curve. As the magnetic field increases, the degeneracy of the spin levels is increased and at certain magnetic fields an electron can jump from the upper to the lower level, causing the kinks in the ground state energy. When all electrons are in the lowest spin level no transitions can occur and the curves for both the total and addition energy are smooth.

Recent calculations [9] and measurements [23] indicate that at higher magnetic fields than the ones shown in Fig. 2.7 an edge reconstruction occurs, resulting in an extra kink

B (T)
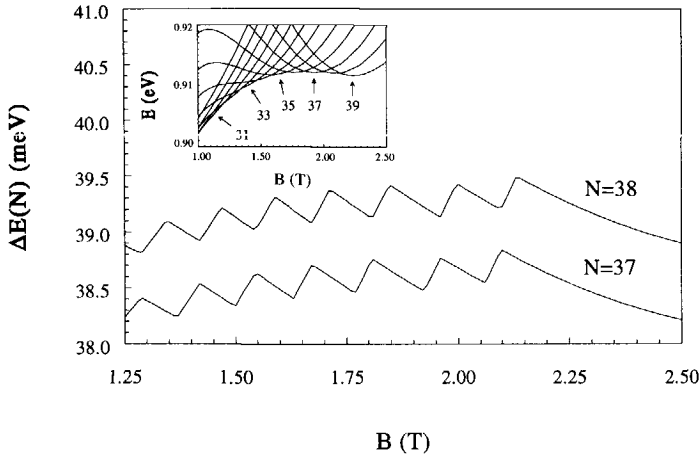
Figure 2.7: *Addition energy for quantum dots of 37 and 38 electrons as a function of magnetic field. The calculation was performed for a confinement strength $\hbar\omega_0 = 1.6$ meV, $d = 100$ nm and $\langle \delta z \rangle = 10$ nm. The inset shows the ground state energies of the different possible configurations of the dot as a function of magnetic field. The numbers represent the number of electrons in the lowest spin level. Only odd numbers are indicated.*

in the curve for the addition energy in the regime where only one spin level is occupied. Performing a calculation with filling factors that are restricted to integer values, we are able to reproduce this feature. However, for the small confinement strength α at which this transition occurs, the fractional-filling solution is not so well converged. In spite of the fact that we find evidence for the edge reconstruction, the numerical accuracy of our solution does not allow decisive conlusions.

In comparison with the results obtained in Ref. [18] the oscillations found in our calculations have a larger period and amplitude by a factor of approximately 1.5. The increase in amplitude of the oscillations can be qualitatively understood in terms of the capacitance model for the island proposed by Evans *et al.* [24] and is due to the increase of the width of the incompressible strip in the picture including exchange. This results in a decrease of the capacitance between the inner and outer compresible regions where the extra electron can be added and hence in an increase in the peak-to-peak amplitude. The larger period can be explained in a similar fashion: Exchange effects reduce the widths of the compressible strips and thus the capacitances C_1 and C_2 between the respective compressible strips and the back gate which results in an increased period of the oscillations compared to the electrostatic treatment of McEuen *et al.*. Compared with their experimental data, the period of the oscillations found in our calculations is about 0.3 T too large whereas their calculations give a period which is 0.25 T too small. However, these values depend sensitively on the calculated ground state density since the total energy, with a typical value around 1 eV, has to be calculated with an absolute accuracy of at least 0.1 meV in order to resolve the oscillations and therefore small numerical deviations from the true ground state would drastically influence the addition energies.

2.5 SUMMARY AND CONCLUDING REMARKS

We have used density-functional theory in strong magnetic fields to investigate the effects of the electron-electron interaction on edge states in the integer quantum Hall regime. We have included exchange in the local density approximation. In this approximation smooth density distributions corresponding to fractional filling at the edges can be treated, which is beyond a Hartree-Fock treatment of edge channels [8]. To describe fractional occupation could otherwise only be achieved by exact diagonalization or configuration interaction calculations [9]. We have found that the width of the edge channels is strongly reduced due to exchange effects and that the width of the incompressible strips is of the order of several magnetic lengths, which should have a strong influence on the spin-flip equilibration length and the two-terminal conductance of a point contact. We predict a range of confinement potentials $\hbar\omega_0$=3.2 meV-5.1 meV in which the entire regime from electrostatic to Hartree-Fock is covered. Furthermore we have calculated ground state properties of the system in the presence of a back gate parallel to the quantum wire. We established an increasingly important role for the exchange interaction as the back gate is closed in on the 2DEG. As a second application we have calculated the ground state of a quantum dot in a strong magnetic field. We found that the results are similar to those found for the quantum wire. We compared addition energies for the dot with the selfconsistent calculations of McEuen *et al.* [18] and found that the oscillations in the addition energies have larger amplitudes and periods in our calculations.

REFERENCES

[1]   B. I. Halperin, Phys. Rev. B **25**, 2185 (1982).

[2]   C. W. J. Beenakker, Phys. Rev. Lett. **64**, 216 (1990).

[3]   A. H. MacDonald, Phys. Rev. Lett. **64**, 220 (1990).

[4]   X. G. Wen, Phys. Rev. Lett. **64**, 2206, (1990).

[5]   A. H. MacDonald, S. R. Eric Yang, and M. D. Johnson, Aust. J. Phys. **46**, 345 (1993).

[6]   D. B. Chklovskii, B. I. Shklovskii, and L. I. Glazman, Phys. Rev. B **46**, 4026 (1992).

[7]   D. B. Chklovskii, K. A. Matveev, and B. I. Shklovskii, Phys. Rev. B **47**, 12605 (1993).

[8]   J. Dempsey, B. Y. Gelfand, and B. I. Halperin, Phys. Rev. Lett. **70**, 3639 (1993).

[9]   C. de C. Chamon and X. G. Wen, Phys. Rev. B, **49**, 8227 (1994).

[10] T. H. Stoof and G. E. W. Bauer, in *High Magnetic Fields in the Physics of Semiconductors*, D. Heiman (ed.), (World Scientific, Singapore, 1996).

[11] M. Ferconi and G. Vignale, Phys. Rev. B **50**, 14772 (1994).

[12] G. Vignale and M. Rasolt, Phys. Rev. Lett. **59**, 2360 (1987); Phys. Rev. B **37**, 10685 (1988).

[13] See, e.g., R. M. Dreizler and E. K. U. Gross, *Density functional theory. An approach to the quantum many-body problem*, (Springer, Berlin, 1990).

[14] It is possible to obtain compressible densities using (infinitesimal) small temperatures because the filling factor is related to the ground state density via a Fermi-Dirac distribution: $\nu(\mathbf{r}) = f(\epsilon(n(\mathbf{r})) - \mu)$.

[15] L. Rijkels and G. E. W. Bauer, Phys. Rev. B **50**, 8629 (1994).

[16] F. Stern, Phys. Rev. Lett. **30**, 278 (1973).

[17] J. M. Kinaret and P. A. Lee, Phys. Rev. B **42**, 11768 (1990).

[18] P. L. McEuen, E. B. Foxman, J. Kinaret, U. Meirav, M. A. Kastner, N. S. Wingreen, and S. J. Wind, Phys. Rev. B **45**, 11419 (1992).

[19] R. C. Ashoori, H. L. Stormer, J. S. Weiner, L. N. Pfeifer, K. W. Baldwin, and K. W. West, Phys. Rev. Lett. **71**, 613 (1993).

[20] J. F. Janak, Phys. Rev. **178**, 1416 (1969); T. Ando and Y. Uemura, J. Phys. Soc. Japan **37**, 1044 (1974).

[21] Calculating the ground state in this manner does increase the width of the incompressible region and it slightly reduces the width of the edge channels but the effects are smaller than in those obtained with our method.

[22] A. V. Khaetskii, Phys. Rev. B **45**, 13777 (1992).

[23] O. Klein, C. de C. Chamon, D. Tang, D. M. Abusch-Magder, U. Meirav, X. G. Wen, M. A. Kastner, and S. J. Wind, Phys. Rev. Lett. **74**, 785 (1995).

[24] A. K. Evans, L. I. Glazman, and B. I. Shklovskii, Phys. Rev. B **48**, 11120 (1993).

3

TIME-DEPENDENT RESONANT TUNNELING VIA TWO DISCRETE STATES

T. H. Stoof and Yu. V. Nazarov

We theoretically investigate time-dependent resonant tunneling via two discrete states in an experimentally relevant setup. Our results show that the dc transport through the system can be controled by applying external irradiation with a frequency which matches the energy difference between the discrete states. We predict resonant phenomena which should be easily observable in experiments.

Time-dependent tunneling phenomena have received increasing attention in recent years. In the early eighties, Büttiker and Landauer studied the tunneling time needed for an electron to traverse a potential barrier [1]. More recent theoretical work focused on the time-dependence of resonant tunneling using an effective Schrödinger equation [2] and on a description of the time-dependent current through mesoscopic structures in terms of non-equilibrium Green's functions [3]. In addition, the considerable improvement in nanofabrication techniques facilitated some interesting experimental studies. Kouwenhoven *et al.* measured the photon-assisted tunneling current through a single quantum dot with an effectively continuous level spectrum due to thermal smearing [4]. Van der Vaart *et al.* studied the dc current through a double dot system with well developed 0D states in each dot and clearly resolved resonances between energy levels in both dots [5]. The sharp resonance features make it very tempting to perform experiments with time-dependent fields. The dc current through such a structure in the presence of oscillating fields may be expected to display interesting new phenomena, not observable in a single dot.

Some time-dependent aspects of resonant tunneling via two wells in layered semiconductor heterostuctures have been studied in Refs. [6, 7]. However, the states in such stuctures are not really discrete and it is plausible to disregard Coulomb blockade effects. This makes it impossible to apply the results of these works to realistic ultrasmall quantum dots.

In this chapter we use the density matrix approach of Ref. [8], in which the resonant states, being true quantum-mechanical many-body states of the two dots, are described by a time-dependent tunneling Hamiltonian. Transitions between non-resonant states of the system are taken into account through a master equation for the density matrix elements. We calculate the photoresponse of the system in several experimentally relevant limits and derive an explicit expression for the shape of the resonant peaks in the case of an external perturbation with arbirary amplitude. Close to resonance the dc current is found to be very sensitive to the oscillating field. The satellite resonances induced by the external oscillating field can be of the same order of magnitude as the main static resonance with an even smaller width.

The system under consideration (Fig. 3.1) consists of two quantum dots A and B in series. The dots are connected by tunnel junctions to two large reservoirs L and R, which are assumed to have continuous energy level spectra and are filled up to their respective Fermi energies. If we neglect all tunneling processes, a system of discrete many-body states is formed in each dot. The best conditions for transport occur when it costs no energy to transfer an electron between the dots, i.e. the energy difference between a state with one extra electron in the left dot and a state with one extra electron in the right dot is zero. In the experiment in Ref. [5] this energy difference could be tuned by an external gate voltage. The current through the system vs. gate voltage consists of a series of peaks corresponding to the resonances between different discrete states. There could be a variety of different transport processes occuring in a resonance point as described in Ref. [8]. We concentrate on the simplest experimentally relevant case, namely when the resonance occurs between the ground states of both dots. We assume that the bias voltage is much larger than the temperature and the energy difference between the states in resonance. Consequently, electrons can only enter the two-dot system from the left and leave it only to the right. Transitions from the left and to the right lead are possible with rates Γ_L and Γ_R, respectively. Here and throughout the chapter units are used such that $\hbar = 1$. We will assume that the voltage applied is such that it is impossible, due to the Coulomb blockade,
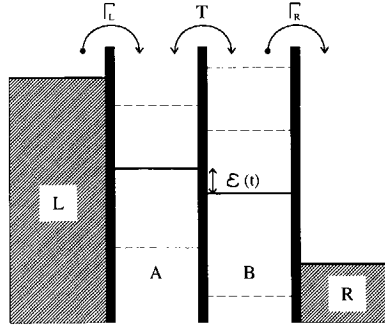
Figure 3.1: *Schematic picture of the system. Two quantum dots A and B are coupled to leads L and R via tunnel junctions. Transitions are possible with rates Γ_L and Γ_R. The tunneling rate between the dots is T and the energy difference between the levels is denoted by $\epsilon(t)$.*

for an electron to tunnel into the system while another electron is still present in either one of the dots. We concentrate on two states only and disregard other states, which is allowed in the neighborhood of the resonance. The system can also be in a third state $|0\rangle$ [9], when there is no extra electron in either one of the dots. The energies of the resonant states, which both lie well between the electrochemical potentials in the left and right lead, initially differ by an amount ϵ_0. Under these conditions the transport through the system depends only very weakly on the bias voltage, but does depend strongly on the gate electrode via the energy difference ϵ_0. We assume that a time-dependent oscillating signal is applied to the gate electrode, so that the time-dependent energy difference becomes: $\epsilon(t) = \epsilon_0 + \tilde{\epsilon}\cos\omega t$, where $\tilde{\epsilon}$ is the amplitude and ω the frequency of the externally applied signal.

The dynamics of the resonant states, $|a\rangle$ and $|b\rangle$, is governed by the time dependent tunneling Hamiltonian $\mathcal{H}(t) = \mathcal{H}_0(t) + \mathcal{H}_T$, where $\mathcal{H}_0$ is given by

$$\mathcal{H}_0(t) = \frac{1}{2}\epsilon(t) \left(\, |a\rangle\langle a| - |b\rangle\langle b| \,\right) \tag{3.1}$$

and $\mathcal{H}_T$ describes the coupling between the dots that introduces mixing between the eigenstates $|a\rangle$ and $|b\rangle$ of the system:

$$\mathcal{H}_T = T \left(\, |a\rangle\langle b| + |b\rangle\langle a| \,\right). \tag{3.2}$$

The average current through the system is given by

$$\langle I \rangle / e = \mathrm{Tr}(\rho \mathcal{I}), \tag{3.3}$$

where $\mathcal{I}$ is the current operator:

$$\mathcal{I} = iT \left(\, |a\rangle\langle b| - |b\rangle\langle a| \,\right), \tag{3.4}$$

and ρ is the density matrix for the two-level system. We describe transitions between different states in the density matrix approach [8]. The equations for the density matrix

elements read:

$$\frac{\partial \rho_{aa}}{\partial t} = +\Gamma_{\rm L}\,\rho_0 + iT\,(\rho_{ba} - \rho_{ab}) \tag{3.5}$$

$$\frac{\partial \rho_{bb}}{\partial t} = -\Gamma_{\rm R}\,\rho_{bb} - iT\,(\rho_{ba} - \rho_{ab}) \tag{3.6}$$

$$\frac{\partial \rho_{ab}}{\partial t} = -\frac{1}{2}\Gamma_{\rm R}\,\rho_{ab} + i\epsilon(t)\,\rho_{ab} + iT\,(\rho_{bb} - \rho_{aa}) \tag{3.7}$$

$$\frac{\partial \rho_{ba}}{\partial t} = -\frac{1}{2}\Gamma_{\rm R}\,\rho_{ba} - i\epsilon(t)\,\rho_{ba} - iT\,(\rho_{bb} - \rho_{aa}), \tag{3.8}$$

where ρ_{aa}, ρ_{bb} and $\rho_0 = 1 - \rho_{aa} - \rho_{bb}$ denote the probabilities for an electron to be in the left dot, the right dot, or in neither dot, respectively, and $\rho_{ab} = \rho_{ba}^*$ are the non-diagonal density matrix elements. In these equations the terms proportional to $\Gamma_{\rm L}$ and $\Gamma_{\rm R}$ describe the transitions to and from the reservoirs between the states $|0\rangle$ and $|a\rangle$ and the states $|b\rangle$ and $|0\rangle$, respectively. All other terms follow from the Liouville equation: $id\rho/dt = [\mathcal{H}, \rho]$. Note that the rates $\Gamma_{\rm L}$ and $\Gamma_{\rm R}$ do not enter the equations in a symmetric way. $\Gamma_{\rm R}$ describes the decay of the resonant states whereas $\Gamma_{\rm L}$ describes the build-up of these resonant states.

The relevant energy scales of the system are the transition rates $\Gamma_{\rm L}$ and $\Gamma_{\rm R}$, the tunneling amplitude T, and the frequency ω and amplitude $\tilde{\epsilon}$ of the applied perturbation. There are three limiting cases for which we can develop an analytical approach to the problem. They are complementary and essentially cover all the interesting physics.

We will first consider the limiting case of a small perturbation amplitude; $\tilde{\epsilon} \ll \omega, T, \Gamma_{L,R}$. Using the fact that $\rho_0 = 1 - \rho_{aa} - \rho_{bb}$, we rewrite Eqs. (3.5)-(3.8) in matrix notation:

$$\frac{\partial \vec{\rho}}{\partial t} = \left(\hat{\Gamma} + \hat{T} + \hat{\epsilon}_0 + \hat{\epsilon}\cos\omega t\right)\vec{\rho} + \vec{c}, \tag{3.9}$$

where $\vec{\rho} = (\rho_{aa}, \rho_{bb}, \rho_{ab}, \rho_{ba})^T$, $\vec{c} = (\Gamma_{\rm L}, 0, 0, 0)^T$ and the matrices $\hat{\Gamma}$, $\hat{T}$, $\hat{\epsilon}_0$ and $\hat{\epsilon}$ correspond to Eqs. (3.5)-(3.8). The stationary solution of these equations without irradiation is

$$\vec{\rho}_0 = -(\hat{\Gamma} + \hat{T} + \hat{\epsilon}_0)^{-1}\vec{c}. \tag{3.10}$$

This determines the shape of the stationary resonant peaks observed by Van der Vaart *et al.* [5]:

$$I_{\rm stat} = \frac{T^2 \Gamma_{\rm R}}{T^2(2 + \Gamma_{\rm R}/\Gamma_{\rm L}) + \Gamma_{\rm R}^2/4 + \epsilon_0^2}. \tag{3.11}$$

The first order correction to the stationary solution is

$$\vec{\rho}_1 = \vec{\rho}_1^{\,+}\exp(i\omega t) + \vec{\rho}_1^{\,-}\exp(-i\omega t), \tag{3.12}$$

with $\vec{\rho}_1^{\,\pm}$ the positive and negative frequency part, respectively:

$$\vec{\rho}_1^{\,\pm} = -(\hat{\Gamma} + \hat{T} + \hat{\epsilon}_0 \mp i\omega\hat{I})^{-1}\frac{\hat{\epsilon}}{2}\vec{\rho}_0, \tag{3.13}$$

$\hat{I}$ being the unit matrix. This contribution contains only oscillatory terms, which average out when calculating the dc current. We therefore also determine the second order correction terms (proportional to $\tilde{\epsilon}^2$) and obtain

$$\vec{\rho}_2 = -(\hat{\Gamma} + \hat{T} + \hat{\epsilon}_0)^{-1}\frac{\hat{\epsilon}}{2}(\vec{\rho}_1^{\,+} + \vec{\rho}_1^{\,-}). \tag{3.14}$$

Using the density matrix elements $\vec{\rho}_2$ we may calculate the photoresponse of the system. This quantity can be easily measured experimentally by slowly modulating the irradiation amplitude [4]. In Fig. 3.2 a plot is given of the photoresponse as a function of ϵ_0 and ω for $\Gamma_L = \Gamma_R = 0.2T$. The figure clearly shows resonant satellite peaks for ω and ϵ_0 satisfying
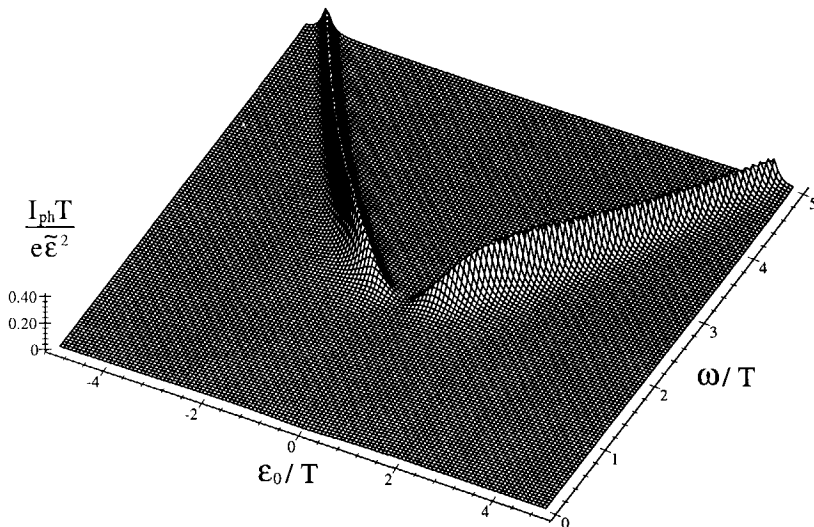

Figure 3.2: *Scaled photoresponse of the system as a function of the energy difference ϵ_0/T between the levels and the frequency ω/T of the applied signal. The plot was made with $\Gamma_L = \Gamma_R = 0.2T$.*

$\omega^2 = \epsilon_0^2 + 4T^2$, i.e. resonant modes occur when the frequency of the applied perturbation matches the renormalized energy difference $\sqrt{\epsilon_0^2 + 4T^2}$ of the two levels. For frequencies below $2T$ there are no satellite peaks because the energy $\hbar\omega$ of the photon is smaller than the energy level spacing. The evolution of a resonant satellite peak is shown in Fig. 3.3, where a current peak for $\omega = 3T$ has been plotted vs. ϵ_0 for different values of $\Gamma_R/T = \Gamma_L/T$. We see that the peak can be seen even at moderately large values of Γ_R/T, but the best resonance conditions occur when $\Gamma_R \ll \max(T, \epsilon_0)$ and $\omega = \sqrt{\epsilon_0^2 + 4T^2}$.

We have developed a second approach which allows us to explore the satellite peak at arbitrary values of irradiation amplitude $\tilde{\epsilon}$ under the conditions mentioned above. Substituting $\vec{\rho} = \vec{\rho}_0 + \vec{\rho}_+(t)\exp(i\omega t) + \vec{\rho}_-(t)\exp(-i\omega t)$ in Eq. (3.9) and neglecting terms proportional to $\exp(\pm 2i\omega t)$ we obtain:

$$\frac{\partial \vec{\rho}_0}{\partial t} = \hat{\Gamma}\vec{\rho}_0 + (\hat{\epsilon}_0 + \hat{T})\vec{\rho}_0 + \frac{\hat{\epsilon}}{2}(\vec{\rho}_+ + \vec{\rho}_-) + \vec{c}, \tag{3.15}$$

$$\frac{\partial \vec{\rho}_+}{\partial t} = \hat{\Gamma}\vec{\rho}_+ + (\hat{\epsilon}_0 + \hat{T} - i\omega\hat{I})\vec{\rho}_+ + \frac{\hat{\epsilon}}{2}\vec{\rho}_0, \tag{3.16}$$

$$\frac{\partial \vec{\rho}_-}{\partial t} = \hat{\Gamma}\vec{\rho}_- + (\hat{\epsilon}_0 + \hat{T} + i\omega\hat{I})\vec{\rho}_- + \frac{\hat{\epsilon}}{2}\vec{\rho}_0. \tag{3.17}$$
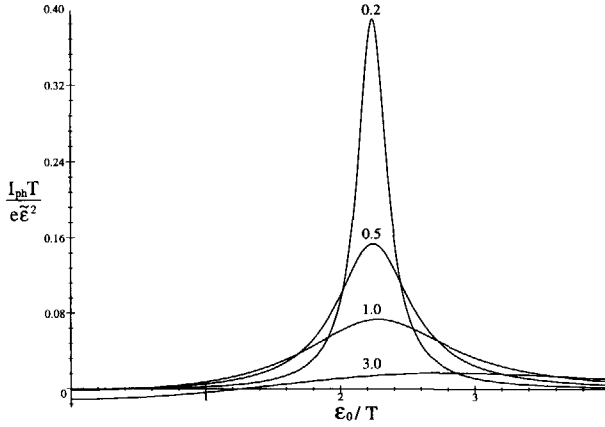
Figure 3.3: *Evolution of a satellite peak for ratios $\Gamma_L/T = \Gamma_R/T = 0.2,\ 0.5,\ 1.0$ and 3.0 respectively. The plots were made for a frequency of $\omega = 3T$.*

Near the resonance point we can approximate the solution $\vec{\rho}$ by an expansion in terms of the eigenvectors of the matrix $\hat{\epsilon}_0 + \hat{T}$: $\vec{\rho}_0 = \alpha_1\vec{v}_1 + \alpha_2\vec{v}_2$, $\vec{\rho}_+ = \alpha_+\vec{v}_+$ and $\vec{\rho}_- = \alpha_-\vec{v}_-$, where $\vec{v}_1$ and $\vec{v}_2$ are the eigenvectors with eigenvalue 0 and $\vec{v}_\pm$ those with eigenvalues $\pm i\sqrt{\epsilon_0^2 + 4T^2}$. We obtain a set of four closed equations for the coefficients $\alpha_{1,2,+,-}$ by taking the inner product of Eq. (3.15) with $\vec{v}_1$ and $\vec{v}_2$, of Eq. (3.16) with $\vec{v}_+$, and of Eq. (3.17) with $\vec{v}_-$. Solving for the stationary solution and calculating the current profile near the resonance point $\epsilon_r = \sqrt{\omega^2 - 4T^2}$ results in a Lorentzian line shape:

$$I/e = \frac{I_{\max}w^2}{w^2 + (\epsilon_0 - \epsilon_r)^2}, \tag{3.18}$$

with height

$$I_{\max} = \frac{\tilde{\epsilon}^2\Gamma_R(\alpha^2 - 4)}{\gamma(\gamma\Gamma_R^2 + \beta\tilde{\epsilon}^2)}, \tag{3.19}$$

and half-width at half maximum

$$w = \frac{\alpha}{2\sqrt{\alpha^2 - 4}}\sqrt{\Gamma_R^2 + \frac{\beta}{\gamma}\tilde{\epsilon}^2}, \tag{3.20}$$

where $\alpha = \omega/T$, $\beta = \Gamma_R/\Gamma_L + 2$, and $\gamma = \alpha^2 + \beta - 4$.

In the limit of small amplitude the height of the current peak scales with the square of $\tilde{\epsilon}$: $I_{\max} = \tilde{\epsilon}^2(\alpha^2 - 4)/\gamma^2\Gamma_R$, whereas the width remains constant: $w = \frac{1}{2}\alpha\Gamma_R/\sqrt{\alpha^2 - 4} \sim \Gamma_R$, consistent with the results presented in Fig. 3.3. At $\alpha = 2$ (corresponding to $\epsilon_0 = 0$) the peak vanishes, as seen in Fig. 3.2. With further increase of $\tilde{\epsilon}$ the current saturates at a value of $I_{sat} = \Gamma_R(\alpha^2 - 4)/\beta\gamma$ which is of the order of the height of the stationary peak.

This saturation occurs at relatively small $\tilde{\epsilon} \sim \Gamma_R$. The width of the peak increases with growing $\tilde{\epsilon}$. At $\tilde{\epsilon} \gg \Gamma_R$ it is proportional to $\tilde{\epsilon}$.

Therefore we have shown that, under good resonance conditions, the current is very sensitive to the external irradiation. A relatively weak irradiation induces a big satellite peak that has a much smaller width than the stationary one.

For small tunneling amplitudes T, provided $\epsilon_0 \gg \Gamma_R$, the height scales with T^2: $I_{\max} = T^2 \tilde{\epsilon}^2 / \Gamma_R \omega^2$, and the half-width reduces to $w = \frac{1}{2}\Gamma_R$. These results agree with the expression for the photon-assisted tunneling current derived below, where we consider our third approach, in which the tunneling amplitude is small compared to all other energy scales in the system; $T \ll \tilde{\epsilon}, \omega, \Gamma_{L,R}$.

First we perform a transformation on the density matrix which leaves the diagonal elements invariant and which changes the non-diagonal elements as follows:

$$
\bar{\rho}_{ab} = \rho_{ab} \exp\left(-i \int_{-\infty}^{t} d\tau\, \epsilon(\tau)\right), \tag{3.21}
$$

This transformation eliminates the explicit time dependence in Eqs. (3.7) and (3.8) and introduces it in the transformed tunneling amplitude. The equations for the non-diagonal density matrix elements now assume the form

$$
\frac{\partial \bar{\rho}_{ab}}{\partial t} = \left(i\epsilon_0 - \frac{1}{2}\Gamma_R\right)\bar{\rho}_{ab} + i\bar{T}(t)\left(\bar{\rho}_b - \bar{\rho}_a\right), \tag{3.22}
$$

with time-dependent tunneling amplitude

$$
\bar{T}(t) = T \exp\left(i \int_{-\infty}^{t} d\tau\, \epsilon(\tau)\right). \tag{3.23}
$$

The equations for $\bar{\rho}_{ba}$ are simply the complex conjugate of Eqs. (3.21), (3.22) and (3.23). For $\bar{\rho}_{ab,\omega}$ in the lowest non-vanishing order in T we obtain:

$$
\bar{\rho}_{ab,\omega} = \frac{i\bar{T}_\omega}{\frac{1}{2}\Gamma_R + i(\omega - \epsilon_0)}. \tag{3.24}
$$

Expanding $\bar{T}(t)$ in a Fourier series;

$$
\bar{T}(t) = T \sum_{n=-\infty}^{\infty} J_n(\tilde{\epsilon}/\omega) \exp\left(-in\omega t\right), \tag{3.25}
$$

and calculating the dc current, Eq. (3.3), results in:

$$
\langle I \rangle / e = T^2 \Gamma_R \sum_{n=-\infty}^{\infty} \frac{J_n^2(\tilde{\epsilon}/\omega)}{\frac{1}{4}\Gamma_R^2 + (n\omega - \epsilon_0)^2}, \tag{3.26}
$$

where J_n is a n'th order Bessel function of the first kind. This equation for the current is similar to the expression found by Tien and Gordon [10] for the photon assisted tunneling current through a superconducting tunnel junction. Note, however, that in the Tien-Gordon case the current has been considered as a function of bias voltage whereas in our case it is a function of ϵ_0, the energy shift of the discrete levels. Analogously, the alternating field is not applied in the bias direction but rather to the gate electrodes.

In Fig. 3.4 the current has been plotted as a function of ϵ_0 and $\tilde{\epsilon}$. The figure clearly shows that the current is composed of a number of satellite peaks each separated by the photon energy $\hbar\omega$. With increasing amplitude $\tilde{\epsilon}$, the number of visible current peaks increases. The peaks all have the same width Γ_R and have heights given by $4T^2 J_n^2(\tilde{\epsilon}/\omega)/\Gamma_R$. In the limit of small amplitude the height of the $n = 1$ satellite peak reduces to $I_{\max} = T^2\tilde{\epsilon}^2/\Gamma_R\omega^2$, identical to our earlier result. Note that Eq. (3.26) for the current no longer contains Γ_L. Because the tunnel rate from lead to dot is much larger than the tunnel rate between the dots, the width of the level is in this case determined by Γ_R and T only.
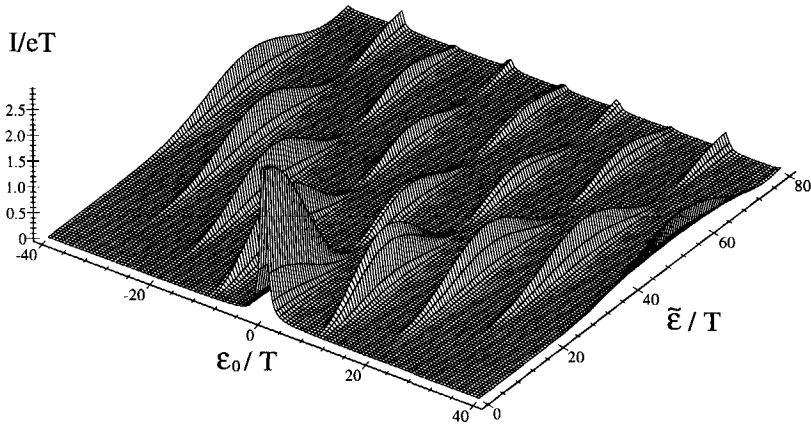

Figure 3.4: *Scaled current through the dots as a function of the energy difference ϵ_0/T between the levels and the amplitude $\tilde{\epsilon}/T$ of the applied signal. The plot was made with $\Gamma_R = T$ and $\omega = 10T$.*

In conclusion, we have presented a complete theoretical picture of the dc transport through a double quantum dot in the presence of external harmonic irradiation. The photoresponse of the system exhibits extra resonant peaks when the frequency of the external irradiation matches the energy difference between the discrete states. At further increase of the irradiation intensity this satellite peak becomes of the same order of magnitude as the main peak, but preserves the much smaller width. At small tunneling amplitudes and large irradiation amplitude extra satellite peaks appear in a pattern similar to that obtained for a Josephson junction by Tien and Gordon [10].

REFERENCES

[1] M. Büttiker and R. Landauer, Phys. Rev. Lett. **49**, 1739 (1982).

[2] I. Bar-Joseph and S.A. Gurvitz, Phys. Rev. B. **44**, 3332 (1991).

[3] N. S. Wingreen, A. P. Jauho, and Y. Meir, Phys. Rev. B **48**, 8487 (1993).

[4] L. P. Kouwenhoven, S. Jauhar, J. Orenstein, P. L. McEuen, Y. Nagamune, J. Motohisha, and H. Sakaki, Phys. Rev. Lett. **73**, 3443 (1994).

[5] N. C. van der Vaart, S. F. Godijn, Yu. V. Nazarov, C. J. P. M. Harmans, J. E. Mooij, L. W. Molenkamp, and C. T. Foxon, Phys. Rev. Lett. **74**, 4702 (1995).

[6] S. A. Gurvitz, Phys. Rev. B **44**, 11924 (1991); the method used has been corrected in S. A. Gurvitz, H. J. Lipkin, and Y. S. Prager, Mod. Phys. Lett. B **8**, 1377 (1994) and S. A. Gurvitz and Y. S. Prager, Phys. Rev. B **53**, 15932 (1996).

[7] A. V. Korotkov, D. V. Averin and K. K. Likharev, Phys. Rev. B **49**, 7548 (1994).

[8] Yu. V. Nazarov, Physica B **189**, 57 (1993).

[9] The notation $|0\rangle$ does not imply that there are no electrons in the dots. It may denote any ground state (N, M) with N electrons in the left dot and M in the right one. The resonance then occurs betveen the states $(N + 1, M)$ ($|a\rangle$) and $(N, M + 1)$ ($|b\rangle$).

[10] P. K. Tien and J. P. Gordon, Phys. Rev. **129**, 647 (1963).

4

A COHERENT DOUBLE-QUANTUM-DOT ELECTRON PUMP

T. H. Stoof and Yu. V. Nazarov

We have calculated the transport characteristics of an electron pump consisting of an asymmetric double quantum dot at zero bias voltage which is subject to electromagnetic radiation. Depending on the energies of the intermediate states in the pumping cycle, electrons can be transferred through the dots incoherently via sequential tunneling or coherently via co-tunneling. The dc transport through the system can be controlled by the frequency of the applied radiation. We describe resonant tunneling peaks in the pumping current that should be observable experimentally.

4.1   INTRODUCTION

A quantum dot can be thought of as an artificial atom with adjustable parameters. It is of more than fundamental interest to study its properties under various circumstances, e.g. by transport experiments (see e.g. Ref. [1]). By considering a double-quantum-dot system, the analogy with real atoms can be stretched to include artificial molecules. The analogue of the covalent bond is then formed by an electron which coherently tunnels back and forth between the two dots. By applying electromagnetic radiation with a frequency equal to the energy difference between the time-independent eigenstates of the double-dot system, an electron can undergo these so-called spatial Rabi oscillations even when the tunneling matrix element between the dots is small [2, 3]. Recently, several time-dependent transport measurements on quantum-dot systems have been reported [4, 5, 6, 7, 8], most of them being of a spectroscopic nature. It has also been suggested to construct devices from quantum dots. Examples of such applications are pumps that transfer electrons one by one by using time-dependent voltages to alternatingly raise and lower tunnel barrier heights [9, 10], or systems in which coupled quantum dots (or quantum wells) are used for quantum-scale information processing [11, 12, 13]. Because the transport mechanism in the abovementioned pumps is determined by sequential tunneling, electrons are pumped incoherently. In this chapter we describe an electron pump that can also transfer electrons coherently, because the electrons are transferred through the system by means of a co-tunneling process. In this case, the system switches coherently between two states each time an electron is pumped through the dots. Alternatively, this process can be seen as coherent transport through a double-quantum-dot qubit.

4.2   PUMPING ELECTRONS WITH RADIATION

The system we consider consists of two weakly coupled quantum dots A and B connected to two large reservoirs L and R by tunnel barriers (see Fig. 4.1). The leads are assumed to have a continuous energy spectrum and the bias voltage is zero. Each individual quantum
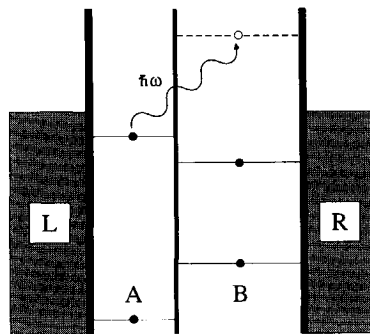

Figure 4.1: *Double-dot system at zero bias voltage. The dots A and B are coupled to the reservoirs L and R by tunnel junctions. An electron in the left dot can tunnel to the right by absorbing a photon.*

dot is in its ground state and in the remainder of this chapter we will only concentrate on the case of transitions between ground states of the dots. Moreover, we assume that the double-dot system is asymmetric in the ground state $|0,0\rangle$, where $|n,m\rangle$ denotes a full many-body state with n extra electrons in the left dot and m in the right dot, respectively. This asymmetry entails that the energy of the state $|1,-1\rangle$ is much higher than the energy of the state $|-1,1\rangle$. In that case an electron can be excited from the left dot into the right one, but the probability of the reverse process occurring can be neglected. By fabricating two dots of different sizes, such an asymmetry can be easily accomplished. The energy difference between the ground state $|a\rangle = |0,0\rangle$ and the excited state $|b\rangle = |-1,1\rangle$ is denoted by ε_0. It can be tuned by an external gate voltage, and throughout this chapter it is assumed to be much larger than the tunneling matrix element between the dots T, i.e. $\varepsilon_0 \gg T$. In this case dc transport through the double dot is blocked.

This situation is changed, however, if we apply electromagnetic radiation to the system. Assume that a time-dependent oscillating signal is present on the gate electrode, so that the time-dependent energy difference between states $|a\rangle$ and $|b\rangle$ becomes $\varepsilon(t) = \varepsilon_0 + \tilde{\varepsilon} \cos \omega t$, where $\tilde{\varepsilon}$ is the amplitude and ω the frequency of the externally applied signal. When the frequency of the applied radiation matches the time-independent energy difference between states $|a\rangle$ and $|b\rangle$, i.e. if $\omega \approx \varepsilon_0$, it is possible for an electron from the left dot to tunnel to the right one. In principle, this electron can now leave the system by tunneling to the right lead, resulting in state $|c\rangle = |-1,0\rangle$. An electron from the left lead can then tunnel to the left dot, thus restoring the ground state. Effectively, an electron has now been transferred from the left electrode to the right one. This transport cycle, $|0,0\rangle \rightarrow |-1,1\rangle \rightarrow |-1,0\rangle \rightarrow |0,0\rangle$, is not the only one. Another possible sequence, in which the system passes the intermediate state $|d\rangle = |0,1\rangle$, is given by $|0,0\rangle \rightarrow |-1,1\rangle \rightarrow |0,1\rangle \rightarrow |0,0\rangle$.

The details of the transport mechanism of a pumping cycle depends on the energies of the intermediate states $|c\rangle$ and $|d\rangle$, as shown in Fig. 4.2. If the energies of the intermediate states are somewhere between those of states $|a\rangle$ and $|b\rangle$, the system relaxes to the ground
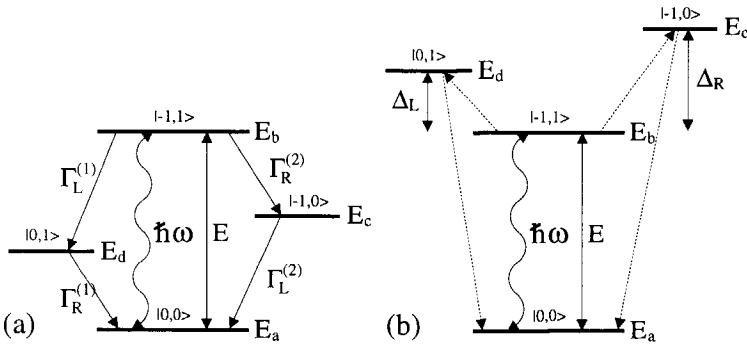
Figure 4.2: *Energy diagrams of the double-dot system in which (a) only incoherent and (b) only coherent tunneling occurs. Indicated are the four possible states of the system and their respective energies:* $|a\rangle = |0,0\rangle$, $|b\rangle = |-1,1\rangle$, $|c\rangle = |-1,0\rangle$, *and* $|d\rangle = |0,1\rangle$, *where the numbers denote the extra electrons in either dot. Also shown are the possible ways in which the system can relax to the ground state.*

state via the sequential (and thus incoherent) tunneling processes described above. As shown in Fig. 4.2 (a), the four tunneling processes are described by the rates $\Gamma_L^{(1)}$, $\Gamma_R^{(1)}$, $\Gamma_L^{(2)}$, and $\Gamma_R^{(2)}$, respectively. Here and throughout this chapter units are used such that $\hbar = 1$. In the opposite case when the energies of the intermediate states are higher than that of state $|b\rangle$, transport via sequential tunneling is blocked. However, transport is still possible via inelastic co-tunneling of electrons [14, 15]. When the system is in state $|b\rangle$, two electrons can tunnel simultaneously, one going from the left reservoir to the left dot and the other going from the right dot to the right electrode. In this process one of the intermediate states is virtually occupied. The necessary energy is provided by relaxing the system to the ground state $|a\rangle$, thereby releasing an energy E. In the following, we will describe these two different mechanisms quantitatively, starting with the sequential tunneling regime.

4.3   THE INCOHERENT MECHANISM

We use the density-matrix approach developed in Refs. [16, 17]. When we disregard tunneling to and from the leads, the Hamiltonian of the two-level system is given by (see also Ref. [2]):

$$\mathcal{H} = \begin{pmatrix} -\frac{1}{2}\epsilon(t) & T \\ T & \frac{1}{2}\epsilon(t) \end{pmatrix}, \tag{4.1}$$

where $\epsilon(t) = \epsilon_0 + \tilde{\epsilon}\cos\omega t$ and T describes the coupling between the dots. We are interested in the particular case where the energy level spacing is large, i.e. $\epsilon_0 \gg T$. Rewriting Eq. (4.1) in the basis of eigenstates of the time-independent ($\tilde{\epsilon} = 0$) Hamiltonian and using the fact that $\tilde{\epsilon} \ll \epsilon_0$, we obtain:

$$\mathcal{H} = \begin{pmatrix} -\frac{1}{2}E & \overline{T}\cos\omega t \\ \overline{T}\cos\omega t & \frac{1}{2}E \end{pmatrix}, \tag{4.2}$$

where $E = \sqrt{\epsilon_0^2 + 4T^2} \approx \epsilon_0$ is the renormalized energy level spacing and $\overline{T} = T\tilde{\epsilon}/E$. From Eq. (4.2) we see that there are small time-dependent matrix elements that cause mixing between the two states. Using the Neumann-Liouville equation of motion for the density matrix; $id\rho/dt = [\mathcal{H}, \rho]$, and including the tunneling to and from the leads, we obtain the equations of motion for the density-matrix elements:

$$\frac{\partial \rho_{aa}}{\partial t} = \Gamma_L^{(2)}\rho_{cc} + \Gamma_R^{(1)}\rho_{dd} + i\overline{T}\cos\omega t(\rho_{ab} - \rho_{ba}), \tag{4.3}$$

$$\frac{\partial \rho_{bb}}{\partial t} = -(\Gamma_L^{(1)} + \Gamma_R^{(2)})\rho_{bb} - i\overline{T}\cos\omega t(\rho_{ab} - \rho_{ba}), \tag{4.4}$$

$$\frac{\partial \rho_{cc}}{\partial t} = \Gamma_R^{(2)}\rho_{bb} - \Gamma_L^{(2)}\rho_{cc}, \tag{4.5}$$

$$\frac{\partial \rho_{ab}}{\partial t} = -\frac{1}{2}(\Gamma_L^{(1)} + \Gamma_R^{(2)} - 2iE)\rho_{ab} + i\overline{T}\cos\omega t(\rho_{aa} - \rho_{bb}), \tag{4.6}$$

$$\frac{\partial \rho_{ba}}{\partial t} = -\frac{1}{2}(\Gamma_L^{(1)} + \Gamma_R^{(2)} + 2iE)\rho_{ab} - i\overline{T}\cos\omega t(\rho_{aa} - \rho_{bb}), \tag{4.7}$$

where ρ_{aa}, ρ_{bb}, ρ_{cc}, and $\rho_{dd} = 1 - \rho_{aa} - \rho_{bb} - \rho_{cc}$ denote the probabilities for an electron to be in the states $|a\rangle$, $|b\rangle$, $|c\rangle$ and $|d\rangle$, respectively, and $\rho_{ab} = \rho_{ba}^*$ are the non-diagonal density-matrix elements, or coherences.

The average current through the system is given by:

$$\frac{I_{\text{pump}}}{e} = \Gamma_R^{(2)}\rho_{bb} + \Gamma_R^{(1)}\rho_{dd}. \tag{4.8}$$

In Fig. 4.3 we have plotted the evolution of a resonant current peak for $\tilde{\varepsilon} = 0.1\varepsilon_0$ and $T = 0.1\varepsilon_0$. The current is plotted as a function of the applied radiation frequency for
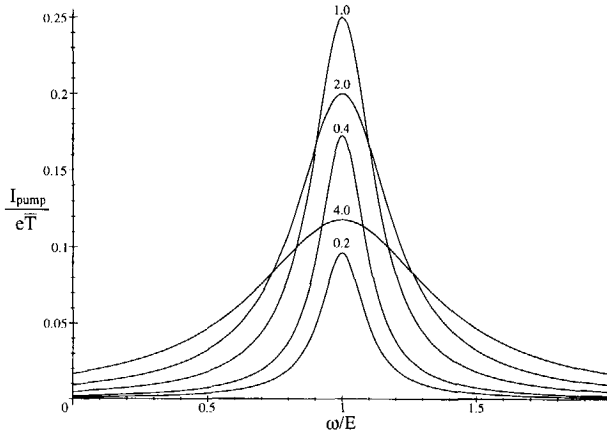

Figure 4.3: *The pumping current as a function of the applied frequency for different values of $\Gamma/\overline{T}$, where we have taken $\Gamma_L^{(1)} = \Gamma_R^{(1)} = \Gamma_L^{(2)} = \Gamma_R^{(2)} = \Gamma$. Calculated for $\tilde{\varepsilon} = 0.1\varepsilon_0$ and $T = 0.1\varepsilon_0$.*

different values of $\Gamma/\overline{T}$, where $\Gamma = \Gamma_L^{(1)} = \Gamma_R^{(1)} = \Gamma_L^{(2)} = \Gamma_R^{(2)}$. The current peak height initially grows with increasing Γ, its width remaining almost constant. The best resonance condition occurs for $\Gamma = \overline{T}$. When Γ increases beyond this value, the height of the peak rapidly decreases while the width increases.

Using an approach developed in Ref. [2], which is valid near resonance, we are able to derive an analytical expression for the shape of the current peak in this regime. We find that the peak is a Lorentzian:

$$\frac{I_{\text{pump}}(\omega)}{e} = \frac{I_{\text{max}}w^2}{w^2 + 4(\omega - E)^2}, \tag{4.9}$$

with height:

$$I_{\text{max}} = \frac{(\Gamma_L^{(1)} + \Gamma_R^{(2)})\overline{T}^2}{\left(\Gamma_L^{(1)} + \Gamma_R^{(2)}\right)^2 + (2 + \alpha)\overline{T}^2}, \tag{4.10}$$

and full width at half maximum:

$$w = \sqrt{\left(\Gamma_L^{(1)} + \Gamma_R^{(2)}\right)^2 + (2 + \alpha)\overline{T}^2}, \tag{4.11}$$

where the dimensionless parameter α is given by:

$$\alpha = \frac{\Gamma_L^{(1)}}{\Gamma_R^{(1)}} + \frac{\Gamma_R^{(2)}}{\Gamma_L^{(2)}}. \tag{4.12}$$

In the limit of small $\overline{T}$, i.e. in the limit of small radiation amplitude $\tilde{\varepsilon}$ and small overlap T, the height of the current peak is proportional to $\overline{T}^2$; $I_{\max} = \overline{T}^2/(\Gamma_L^1 + \Gamma_R^{(2)})$, whereas its width is constant in this limit; $w = \Gamma_L^{(1)} + \Gamma_R^{(2)}$. This concludes the discussion of the incoherent pumping mechanism. We now proceed to describe the coherent transport regime.

4.4   THE COHERENT MECHANISM

In the coherent mechanism, two electrons tunnel simultaneously; one going from the left lead to the left dot, and one from the right dot to the right lead. Because the transport occurs via the virtual occupation of a state with a large electrostatic energy, these two tunneling events cannot be treated independently. The rate at which this co-tunneling process occurs can be calculated analytically. Following Ref. [15], we first consider the amplitude of an elementary two-electron co-tunneling process between initial state $|i\rangle = |b\rangle$ and final state $|f\rangle = |a\rangle$. This amplitude is the sum of two terms corresponding to the virtual occupation of the two intermediate states $|c\rangle$ and $|d\rangle$:

$$\langle i|M|f\rangle = t_L t_R \left(\frac{1}{\Delta_L - \varepsilon_L} + \frac{1}{\varepsilon_R + \Delta_R} \right), \tag{4.13}$$

where $\Delta_L = E_d - E_b$, $\Delta_R = E_c - E_b$, and t_L and t_R denote the matrix elements for tunneling through the left and right barrier, respectively. The energy denominators in Eq. (4.13) are related to the fact that the intermediate states are virtually occupied. The "partial" tunnel rate for a single co-tunneling process is given by:

$$\Gamma_{\text{partial}} = 2\pi|\langle i|M|f\rangle|^2 \delta(\varepsilon_i - \varepsilon_f). \tag{4.14}$$

We obtain the total tunnel rate, Γ_{ct}, by multiplying Eq. (4.14) by the probabilities $f(\varepsilon_L)$ that the state in the left electrode with energy ε_L is filled and $1 - f(\varepsilon_R)$ that there is an unoccupied state in the right reservoir having energy ε_R, and integrating over all reservoir energies:

$$\Gamma_{ct} = \int d\varepsilon_L \int d\varepsilon_R C f(\varepsilon_L)[1 - f(\varepsilon_R)] \left(\frac{1}{\Delta_L - \varepsilon_L} + \frac{1}{\varepsilon_R + \Delta_R} \right)^2 \delta(E + \varepsilon_L - \varepsilon_R), \tag{4.15}$$

where $C = 2\pi|t_L t_R|^2 \nu_L \nu_R$, with ν_L and ν_R the density of states in the left and right electrode, respectively. The delta function in Eq. (4.15) ensures energy conservation for each individual tunneling process. Because the reservoirs are in equilibrium, $f(\varepsilon)$ is given by the Fermi-Dirac distribution function. At zero temperature Eq. (4.15) becomes:

$$\Gamma_{ct} = \frac{2C\left[\ln\left(1 + \frac{E}{\Delta_L}\right) + \ln\left(1 + \frac{E}{\Delta_R}\right)\right]}{\Delta_L + \Delta_R + E} + \frac{CE}{\Delta_L(\Delta_L + E)} + \frac{CE}{\Delta_R(\Delta_R + E)}, \tag{4.16}$$

where we have disregarded the energy dependence of both the tunneling matrix elements $t_{L,R}$ and the densities of states $\nu_{L,R}$. In the limit of large charging energies, $E \ll \Delta_L, \Delta_R$, which we will consider in the remainder of this chapter, Eq. (4.16) reduces to a simple expression:

$$\Gamma_{ct} = 2\pi |t_L t_R|^2 \nu_L \nu_R \left(\frac{1}{\Delta_L} + \frac{1}{\Delta_R} \right)^2 E, \tag{4.17}$$

which is linear in E. In the absence of radiation, the average current through the system is given by:

$$\frac{I_{pump}}{e} = \Gamma_{ct} \rho_{bb}, \tag{4.18}$$

which is zero, since $\rho_{bb} = 0$. In order to calculate the current in the presence of radiation, we therefore need equations for the density matrix elements ρ_{aa} and ρ_{bb} taking into account the radiation-induced co-tunneling processes. In contrast to the situation in the incoherent mechanism, these density matrix elements are the only diagonal ones because the states $|c\rangle$ and $|d\rangle$ are now occupied only virtually. Below, we will use the technique of the closed-time path Green function, reviewed in e.g. Refs. [18, 19] and applied to quantum-dot systems in Ref. [20], to obtain the equations of motion for the density-matrix elements.

To this end we need expressions for the advanced and retarded Green functions of the time-dependent double-dot system in the absence of tunneling. As before, we choose the eigenstates of the time-independent Hamiltonian as the basis for our calculations. The time-dependent Schrödinger equation then becomes:

$$i \frac{d\psi_\alpha(t)}{dt} = (\mathcal{H}_0 + \mathcal{E} \cos \omega t) \psi_\alpha(t), \tag{4.19}$$

with

$$\mathcal{H}_0 = \begin{pmatrix} -\frac{E}{2} & 0 \\ 0 & \frac{E}{2} \end{pmatrix} \text{ and } \mathcal{E} = \frac{\tilde{\varepsilon}}{E} \begin{pmatrix} \frac{-\varepsilon_0}{2} & T \\ T & \frac{\varepsilon_0}{2} \end{pmatrix}. \tag{4.20}$$

Expanding the wave functions $\psi_\alpha(t)$ in harmonics we obtain:

$$\psi_\alpha(t) = e^{-iE_\alpha t} \sum_n \mathbf{c}_\alpha^n e^{-in\omega t}. \tag{4.21}$$

Substituting Eq. (4.21) into the Schrödinger equation (4.19) results in a recursive equation for the coefficients $\mathbf{c}_\alpha^n$, which are two-component vectors:

$$\mathbf{c}_\alpha^n (E_\alpha + n\omega) = \hat{H}_0 \mathbf{c}_\alpha^n + \tfrac{1}{2}\hat{\varepsilon}(\mathbf{c}_\alpha^{n-1} + \mathbf{c}_\alpha^{n+1}), \tag{4.22}$$

where $\alpha = a, b$ pertains to the ground state $|a\rangle$ and the excited state $|b\rangle$, respectively. The retarded Green function, $G_{\beta\alpha}^R(t, t')$, which is proportional to the probability amplitude for the system to evolve from state $|\alpha\rangle$ at time t' to state $|\beta\rangle$ at time t, is then given by:

$$G_{\beta\alpha}^R(t, t') = -i\theta(t - t') \sum_{n,m} d_{\beta\alpha}^{mn} e^{i(E_\beta + m\omega)t - i(E_\alpha + n\omega)t'}, \tag{4.23}$$

where the coefficients $d_{\beta\alpha}^{mn}$ are given by:

$$d_{\beta\alpha}^{mn} = \mathbf{c}_\beta^m \cdot \mathbf{c}_\alpha^n. \tag{4.24}$$

In the case of a small radiation amplitude, $\tilde{\varepsilon} \ll \varepsilon_0$, and near resonance, $\omega \approx E$, it is a good approximation to retain only the $n = 0$ and $n = 1$ terms for $\psi_a(t)$, and the $n = 0$ and $n = -1$ terms for $\psi_b(t)$. This approximation entails that we only take into account single-photon transitions between the states $|a\rangle$ and $|b\rangle$. A comparison between the approximate solution and an exact solution, obtained numerically, showed that this approximation is indeed justified. In the regime considered here, the deviation from the exact solution is less than 1%. The wave functions now become:

$$\psi_a(t) = e^{-iE_a t} \begin{pmatrix} \xi \\ -\zeta e^{-i\omega t} \end{pmatrix}, \tag{4.25}$$

and

$$\psi_b(t) = e^{iE_a t} \begin{pmatrix} \zeta e^{i\omega t} \\ \xi \end{pmatrix}, \tag{4.26}$$

where the coefficients ξ and ζ are given by:

$$\xi = \frac{1}{\sqrt{2}} \frac{E - \omega + \sqrt{(E - \omega)^2 + \overline{T}^2}}{\sqrt{(E - \omega)^2 + \overline{T}^2 + (E - \omega)\sqrt{(E - \omega)^2 + \overline{T}^2}}}, \tag{4.27}$$

and

$$\zeta = \frac{1}{\sqrt{2}} \frac{\overline{T}}{\sqrt{(E - \omega)^2 + \overline{T}^2 + (E - \omega)\sqrt{(E - \omega)^2 + \overline{T}^2}}}. \tag{4.28}$$

At resonance, when $\omega = E$, the coefficients are $\xi = \zeta = \frac{1}{2}\sqrt{2}$. The energy E_a in Eqs. (4.25) and (4.26) is given by:

$$E_a = -E_b = -\tfrac{1}{2}E - \tfrac{1}{2}\sqrt{(E - \omega)^2 + \overline{T}^2}. \tag{4.29}$$

This result has a clear physical interpretation. Due to the application of radiation with frequency ω, the energy of the excited state $|b\rangle$ is shifted from $\frac{1}{2}E$ to $\frac{1}{2}E - \omega$. Because $\omega \approx E$, it is now very close to the energy $-\frac{1}{2}E$ of state $|a\rangle$ and since these states have an overlap matrix element $\frac{1}{2}\overline{T}$, they repel each other. The new energies can be found by diagonalizing the Hamiltonian:

$$\mathcal{H}' = \begin{pmatrix} -\tfrac{1}{2}E & \tfrac{1}{2}\overline{T} \\ \tfrac{1}{2}\overline{T} & \tfrac{1}{2}E - \omega \end{pmatrix}, \tag{4.30}$$

which results in the eigenvalues $-\frac{1}{2}E \pm \frac{1}{2}\sqrt{(E - \omega)^2 + \overline{T}^2}$. The lowest of these energies is just E_a and the corresponding eigenvector directly determines the coefficients ξ and ζ of the wave function $\psi_a(t)$. In a similar fashion we can obtain $E_b = -E_a$ and $\psi_b(t)$.

Using the wave functions Eqs. (4.25) and (4.26), the four elements of the retarded Green function, Eq. (4.23), become:

$$G_{aa}^{R}(t,t') = -i\theta(t-t')e^{iE_a(t-t')}\left[\xi^2 + \zeta^2 e^{i\omega(t-t')}\right], \tag{4.31}$$

$$G_{bb}^{R}(t,t') = -i\theta(t-t')e^{-iE_a(t-t')}\left[\xi^2 + \zeta^2 e^{-i\omega(t-t')}\right], \tag{4.32}$$

$$G_{ab}^{R}(t,t') = -i\theta(t-t')\xi\zeta e^{iE_a(t+t')}\left[e^{i\omega t'} - e^{i\omega t}\right], \tag{4.33}$$

$$G_{ba}^{R}(t,t') = -i\theta(t-t')\xi\zeta e^{-iE_a(t+t')}\left[e^{-i\omega t} - e^{-i\omega t'}\right]. \tag{4.34}$$

Note that $G_{bb}^{R}(t,t') = [G_{aa}^{R}(t,t')]^* = G_{aa}^{R}(t',t)$ and $G_{ba}^{R}(t,t') = [G_{ab}^{R}(t',t)]^*$. The components of the advanced Green function are $G_{\beta\alpha}^{A}(t,t') = [G_{\beta\alpha}^{R}(t',t)]^*$.

Using the advanced and retarded Green functions on the Keldysh contour, we can derive equations of motion for the density-matrix elements [18, 19, 20]. In Fig. 4.4 the four lowest order co-tunneling processes contributing to the time evolution of the density matrix are shown. For the derivation of the expressions corresponding to these diagrams we refer to
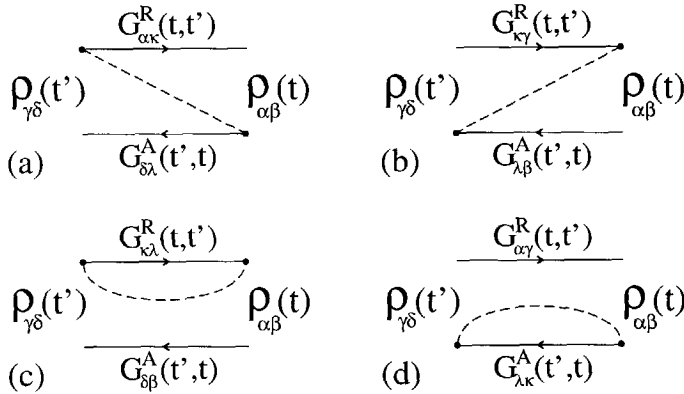

Figure 4.4: *The four lowest order co-tunneling diagrams for the time evolution of the density matrix, where $\alpha,\beta,\gamma,\delta,\kappa,\lambda = a,b$. The dotted line depicts a co-tunneling event. Time increases from left to right.*

Ref. [20]. Because we disregard higher order resonant tunneling processes in our approach, the diagrams only contain a single co-tunneling line. The time points on the upper branch of the contour, going from t' to t, are connected by the retarded Green function $G_{\beta\alpha}^{R}(t,t')$, represented by the full line. Time points on the lower branch, going from t to t', are connected by the advanced Green function $G_{\beta\alpha}^{A}(t',t) = [G_{\beta\alpha}^{R}(t,t')]^*$. The co-tunneling line is taken into account by:

$$V_{ct}(t-t') = \frac{\pm|t_{eff}|^2}{(t-t'\pm i\eta)^2}, \tag{4.35}$$

where $|t_{eff}|^2 = |t_L t_R|^2 \nu_L \nu_R (\frac{1}{\Delta_L} + \frac{1}{\Delta_R})^2$ and the sign in the denominator is positive for diagrams Fig. 4.4 (a) and (c), whereas it is negative for diagrams Fig. 4.4 (b) and (d). The

sign in the numerator is negative for a tunneling line that begins and ends on different branches of the Keldysh contour, Fig. 4.4 (a) and (b), and positive for one that begins and ends on the same branch, Fig. 4.4 (c) and (d). A diagram like e.g. Fig 4.4 (a), which contributes to $\partial \rho_{\alpha\beta}/\partial t$, is calculated as follows:

$$\int_{-\infty}^{t} dt' G_{\alpha\kappa}^{R}(t,t') V_{ct}(t-t') \rho_{\gamma\delta}(t') G_{\delta\lambda}^{A}(t',t). \tag{4.36}$$

Terms describing free propagation without co-tunneling are calculated using the Neumann-Liouville equation of motion. In order to be able to calculate the integral in Eq. (4.36) we use the following Ansatz for the density matrix:

$$\rho(t) = \begin{pmatrix} \rho_{aa} & \rho_{ab}e^{i\omega t} \\ \rho_{ba}e^{-i\omega t} & \rho_{bb} \end{pmatrix}. \tag{4.37}$$

This form, in which only those frequency parts that contribute to the resonant current peak are retained, is known in atomic physics as the rotating wave approximation. We disregarding rapidly oscillating terms because we are only interested in the dc transport properties of the system. The equations of motion for the density-matrix elements then become:

$$\frac{\partial \rho_{bb}}{\partial t} = -i\frac{\overline{T}}{2}(\rho_{ab} - \rho_{ba}) + \xi^2\zeta^2\Gamma_{ct}(1 - 2\rho_{bb}) - (\xi^4 + \zeta^4)\Gamma_{ct}\rho_{bb}, \tag{4.38}$$

$$\frac{\partial \rho_{ab}}{\partial t} = +i\frac{\overline{T}}{2}(1 - 2\rho_{bb}) + i(E - \omega)\rho_{ab} - \frac{\Gamma_{ct}}{2}\rho_{ab}, \tag{4.39}$$

$$\frac{\partial \rho_{ba}}{\partial t} = -i\frac{\overline{T}}{2}(1 - 2\rho_{bb}) - i(E - \omega)\rho_{ba} - \frac{\Gamma_{ct}}{2}\rho_{ba}, \tag{4.40}$$

where $\rho_{aa} + \rho_{bb} = 1$ and where we have used $\omega \approx E$ and $E_a \approx -E/2$ to calculate the dissipative terms. If we use the rotating wave approximation in equations (4.3)-(4.7) for the sequential-tunneling mechanism, the results are very similar to those obtained here. The crucial difference with the equations for the density matrix in the incoherent mechanism, however, is that the tunnel rates in Eq. (4.38) depend on the applied frequency and radiation amplitude via ξ and ζ: They are Lorentzians centered around $\omega = E$ having width $2\overline{T}$. In the absence of irradiation $\xi^2\zeta^2\Gamma_{ct}$ reduces to zero and $(\xi^4 + \zeta^4)\Gamma_{ct}$ to the co-tunnel rate of Eq. (4.17).

We solve for the stationary solution of these equations to calculate the average current through the system which is given by the product of the probability ρ_{bb} to be in the excited state $|b\rangle$ and the total decay rate of state $|b\rangle$:

$$\frac{I_{\text{pump}}}{e} = (\xi^4 + \xi^2\zeta^2 + \zeta^4)\Gamma_{ct}\rho_{bb}. \tag{4.41}$$

In Fig. 4.5 the scaled pumping current is plotted for different values of $\Gamma_{ct}/\overline{T}$. With increasing co-tunnel rate, the scaled peak height first drops rapidly and then decreases slowly to its minimum value, while its width changes only slightly. The peak shape is a Lorentzian of the form Eq. (4.9) with maximum:

$$\frac{I_{\text{max}}}{e} = \frac{3}{16}\frac{4\overline{T}^2 + \Gamma_{ct}^2}{2\overline{T}^2 + \Gamma_{ct}^2}\Gamma_{ct}, \tag{4.42}$$
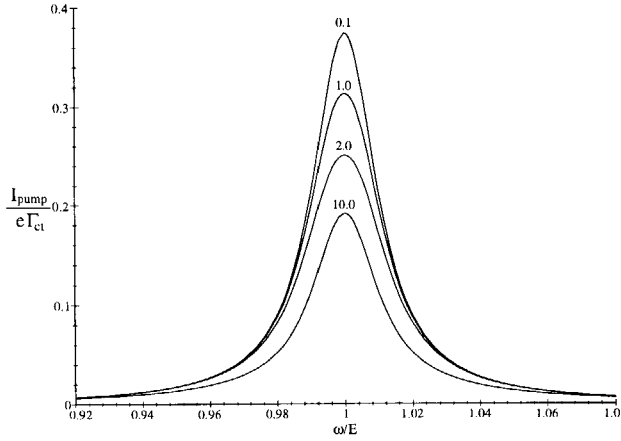
Figure 4.5: *The scaled pumping current in the coherent regime as a function of the applied frequency for different values of* $\Gamma_{ct}/\overline{T}$. *Calculated for* $\tilde{\varepsilon} = 0.1\varepsilon_0$ *and* $T = 0.1\varepsilon_0$.

which reduces to $\frac{3}{8}\Gamma_{ct}$ for small Γ_{ct} and $\frac{3}{16}\Gamma_{ct}$ for large Γ_{ct}. The width of the peak is given by:

$$w = \overline{T}\sqrt{\frac{6(4\overline{T}^2 + \Gamma_{ct}^2)(2\overline{T}^2 + \Gamma_{ct}^2)}{8\overline{T}^4 + \Gamma_{ct}^4}}. \tag{4.43}$$

A comparison with Fig. 4.3 shows that the co-tunnel current peak is much narrower than the incoherent one. Another distinct feature of this co-tunnel peak is the fact that its width changes nonmonotonically with increasing co-tunnel rate Γ_{ct}. For small values of Γ_{ct} the width is equal to $w = \sqrt{6}\ \overline{T} \approx 2.45\ \overline{T}$. It then increases rapidly to reach a maximum of $w = \sqrt{6 + \frac{9}{2}\sqrt{2}}\ \overline{T} \approx 3.52\ \overline{T}$ for $\Gamma_{ct} = 2^{3/4}\ \overline{T} \approx 1.68\ \overline{T}$. On increasing the co-tunnel rate further, the width decreases again to $\sqrt{6}\ \overline{T}$. The width is thus comparatively insensitive to changes in the co-tunnel rate. This is due to the fact that the co-tunnel rates themselves have an intrinsic width $w = 2\overline{T}$, thus restricting the width of the current peak dramatically.

4.5   CONCLUSIONS

In this chapter we considered an electron pump consisting of a double quantum dot subject to radiation. An incoherent and a coherent pumping mechanism was discussed. By deriving equations of motion for the density matrix elements of the double-dot system, we calculated the pumping current in both regimes. Whereas the tunnel rates as a function of the external frequency are constants in the incoherent mechanism, they are Lorentzians in the co-tunnel regime. In both cases the current peak is a Lorentzian, but in the coherent case the peak width is much smaller than in the sequential-tunneling regime and changes nonmonotonically as a function of the co-tunnel rate. Experimental realization of this device would allow

for a systematic study of coherent transport through a solid-state qubit.

REFERENCES

[1] L. P. Kouwenhoven and P. L. McEuen, in *Nano-Science and Technology*, edited by G. Timp, (AIP Press, New York 1996) and references therein.

[2] T. H. Stoof and Yu. V. Nazarov, Phys. Rev. B **53**, 1050 (1996). Chapter 3 of this thesis.

[3] C. A. Stafford and N. S. Wingreen, Phys. Rev. Lett. **76**, 1916 (1996).

[4] L. P. Kouwenhoven, S. Jauhar, K. McCormick, D. Dixon, P. L. McEuen, Yu. V. Nazarov, N. C. van der Vaart, and C. T. Foxon, Phys. Rev. B **50**, 2019 (1994).

[5] L. P. Kouwenhoven, S. Jauhar, J. Orenstein, P. L. McEuen, Y. Nagamune, J. Motohisa, and H. Sakaki, Phys. Rev. Lett. **73**, 3443 (1994).

[6] Y. Nakamura, C. D. Chen, and J. S. Tsai, preprint.

[7] T. H. Oosterkamp, L. P. Kouwenhoven, A. E. A. Koolen, N. C. van der Vaart, and C. J. P. M. Harmans, Phys. Rev. Lett. **78**, 1536 (1997).

[8] T. Fujisawa and S. Tarucha, preprint.

[9] L. P. Kouwenhoven, A. T. Johnson, N. C. van der Vaart, C. J. P. M. Harmans, and C. T. Foxon, Phys. Rev. Lett. **67**, 1626 (1991).

[10] F. W. J. Hekking and Yu. V. Nazarov, Phys. Rev. B **44**, 9110 (1991).

[11] R. Landauer, Science **272**, 1914 (1996).

[12] A. Barenco, D. Deutsch, A. Ekert, and R. Josza, Phys. Rev. Lett. **74**, 4083 (1995).

[13] D. Loss and D. P. DiVicenzo, preprint cond-mat/9701055.

[14] D. V. Averin and A. A. Odintsov, Phys. Lett. A **140**, 251 (1989).

[15] D. V. Averin and Yu. V. Nazarov, Phys. Rev. Lett. **65**, 2446 (1990); in *Single Charge Tunneling* edited by H. Grabert and M. H. Devoret (Plenum, New York, 1992).

[16] Yu. V. Nazarov, Physica B **189**, 57 (1993).

[17] S. A. Gurvitz, H. J. Lipkin, and Y. S. Prager, Mod. Phys. Lett. B **8**, 1377 (1994) and S. A. Gurvitz and Y. S. Prager, Phys. Rev. B **53**, 15932 (1996).

[18] J. Rammer, Rev. Mod. Phys. **63**, 781 (1991).

[19] H. Kleinert, *Path Integrals in Quantum Mechanics, Statistics, and Polymer Physics* (World Scientific, Singapore 1995).

[20] H. Schoeller and G. Schön, Phys. Rev. B **50**, 18436 (1994); J. König, H. Schoeller, and G. Schön, Phys. Rev. Lett. **76** 1715 (1996); J. König, J. Schmid, H. Schoeller, and G. Schön, Phys. Rev B 54, 16820 (1996); J. König, H. Schoeller, and G. Schön, Phys. Rev. Lett. **78**, 4482 (1997).

5

DIFFUSIVE CONDUCTORS AS ANDREEV INTERFEROMETERS

Yu. V. Nazarov and T. H. Stoof

We theoretically study phase-dependent electrical transport in diffusive normal metal-superconductor structures, taking into account (a) the effect of electron-electron interaction in the normal metal and (b) the previously known thermal effect caused by the energy dependence of the diffusivity. Both effects cause changes in the resistance as a function of the phase between two superconductors, but effect (a) is already present at zero temperature, in contrast to effect (b). A detailed theoretical and numerical analysis demonstrates that the mechanism (b) can fully explain recent experiments by Petrashov *et al.* [Phys. Rev. Lett **74**, 5268 (1995)].

What is the resistance of a small normal structure adjacent to a superconductor? Because superconductivity penetrates the structure provided it is short enough, a naive suggestion could be that the resistance vanishes. However, this is not the case. The simplest way to see this is to relate the resistivity to the scattering in the structure [1]. Normal electrons traversing the structure should undergo scattering even if their wave functions are distorted by superconductivity.

If the structure is connected to two superconducting terminals having different phases, the resistance of the structure will depend on the phase difference. This is the physical background of what is called Andreev interferometry. There has been an outburst of interest in this topic recently and different types of Andreev interferometers have been proposed theoretically [2, 3, 4] and realized experimentally [5, 6, 7, 8].

Andreev scattering reveals a significant difference between diffusive conductors, from one side, and tunnel or quasiballistic junctions of the same resistance from another side. Optimal interferometers are composed of tunnel junctions [4, 5], but ballistic and quasiballistic systems also show a big effect [2, 7]. In contrast to this, the standard theory predicts that the zero-voltage, zero-temperature resistance of a diffusive conductor is not affected by penetrating superconductivity [9]. It is slightly modified at finite temperature, when the sample length becomes comparable with the superconducting correlation length in the normal metal, $\xi = \sqrt{\mathcal{D}/\pi T}$, where $\mathcal{D}$ is the diffusivity. At higher temperatures, the resistance returns to its zero-temperature value. This is why the effect of Andreev scattering on the diffusive resistivity is essentially a *thermal* effect. Although this fact is well established and has been confirmed in the frameworks of several independent approaches, a simple physical explanation of this phenomenon is still lacking. Apart from this thermal effect, a small modification may arise from the weak localization correction [10].

However, the recent experiment of Ref. [8] demonstrates a significant phase modulation of the resistivity in small diffusive structures at very low temperatures. The amplitude of the modulation exceeds by several orders of magnitude the one observed in bigger structures and at higher temperatures [6]. The authors of Ref. [8] doubt that their results can be explained by existing theories.

Below we present a novel mechanism that causes a phase-dependent resistance at zero temperature. Because of electron-electron interaction a weak pair potential is induced in the normal metal, which leads to extra Andreev reflection occurring in the structure rather than in the superconductors. The relative resistance change, $\delta R/R$, turns out to be proportional to the interaction parameter in the normal metal, g, and can be of either sign, depending on the sign of g. However, our numerical results show that for the specific structure the magnitude of this effect is too small to explain the data of Ref. [8]. A careful analysis allowed us to conclude that actually the more trivial thermal effect has been observed. The experimental data show excellent agreement with the results of our calculations.

The most adequate theoretical description of the system is provided in the framework of the Keldysh Green function technique elaborated in Ref. [11] for superconductivity. In the diffusive approximation, one first gets equations for the advanced (retarded) Green function, which is a 2×2 matrix depending on coordinate and energy; $\hat{G}(x, \varepsilon)$. The Green function is normalized, $\hat{G}^2 = \hat{1}$, and obeys

$$\partial_x(\mathcal{D}\hat{G}\partial_x\hat{G}) - i[\hat{H}, \hat{G}] = 0. \tag{5.1}$$

where $\mathcal{D}$ is the diffusivity in the normal state, $\hat{H} = \varepsilon\hat{\sigma}_z + i(\text{Re}\Delta(x)\hat{\sigma}_y + \text{Im}\Delta(x)\hat{\sigma}_x)$ and the

$\hat{\sigma}_{xyz}$ are Pauli matrices. We will assume that the temperature is low enough and the size of the normal structure is large enough to satisfy $T, \mathcal{D}/L^2 \ll \Delta_S$, where Δ_S is the energy gap in the superconductors. Then the boundary conditions for $\hat{G}$ take a simple form: $\hat{G} = \hat{\sigma}_z$ in normal reservoirs, and $\hat{G} = \hat{\sigma}_x \sin\phi + \hat{\sigma}_y \cos\phi$ in a superconducting reservoir having phase ϕ.

The Green function $\hat{G}$ determines the characteristics of the energy spectrum of the quasiparticles in the structure. To solve the transport problem, we must know how this spectrum is filled by extra quasiparticles. The equation for the even-in-energy part of the distribution function reads

$$\partial_x(D(\varepsilon, x)\partial_x f(\varepsilon, x)) - \gamma(x)f(\varepsilon) = 0. \tag{5.2}$$

The first term in Eq. (5.2) describes diffusion of quasiparticles with a diffusion coefficient that is influenced by the penetrating superconductivity; $D(\varepsilon) = \mathcal{D}\mathrm{Tr}((\hat{G} + \hat{G}^\dagger)^2)/8$. At zero energy, corresponding to zero temperature, $\hat{G} = \hat{G}^\dagger$ and $D(\varepsilon = 0) = \mathcal{D}$ remains unchanged. The second term describes absorption of quasiparticle excitations into the superconducting condensate, or in other words, conversion of normal into superconducting current. The coefficient γ is proportional to the local value of the pair potential, $\gamma(x) = \frac{-i}{2}\Delta(x)\mathrm{Tr}[i\hat{\sigma}_y(\hat{G}(\varepsilon, x) + \hat{G}(-\varepsilon, x))]$.

In a normal reservoir biased at a voltage V with respect to the superconductors, $f(\varepsilon) = \frac{eV}{2T}\cosh^{-2}(\varepsilon/2T)$. This provides boundary conditions for Eq. (5.2). The current into a reservoir is proportional to the local gradient of f.

The common theoretical approach, see e.g. Refs. [12, 1, 4]), disregards interactions in the normal metal, leading to $\Delta, \gamma \equiv 0$. Since for diffusive conductors this zero-temperature, non-interacting picture does not give the desired resistance change, we concentrate on the effect of Δ in the normal metal. This quantity is given by

$$\Delta = \frac{g}{8i} \int d\varepsilon \tanh\left(\frac{\varepsilon}{2T}\right) \mathrm{Tr}[i\sigma_y(\hat{G}^A - \hat{G}^R)]. \tag{5.3}$$

This is the new feature of the present approach.

Let us first make a simple estimation of the magnitude of the effect. Since it is expected to be small, we solve Eq. (5.2) to first order in γ, which gives a relative resistance change $\delta R/R \simeq \gamma L^2/\mathcal{D}$. At zero energy, $\gamma \simeq \Delta$. In the normal metal, energies in the window $\simeq \mathcal{D}/L^2$ contribute to Δ and therefore $\Delta \simeq g\mathcal{D}/L^2$. This results in a simple estimate for the resistance change,

$$\frac{\delta R}{R} = g\, c(\Phi), \tag{5.4}$$

where c is a dimensionless number depending on the geometry of the structure and on the distribution of the resistivity therein. It is important to note that c depends neither on the structure size nor on the absolute value of the resistance, provided the temperature is low enough; $T \ll \mathcal{D}/L^2$. The effect depends on the normal metal material through g and can be of either sign depending on the sign of g. If the geometry of the structure is well defined, the effect can be used for a direct measurement of the interaction parameter in the normal metal.

At a qualitative level, the effect seems to explain the results of Ref. [8]. Indeed, the phase modulation of the observed resistance at low temperatures was of the order of several percent and appeared material-dependent, including the sign of the resistance change.

This prompted us to make a detailed numerical calculation of the resistance of the specific structure shown in Fig. 5.1, which is very similar to the one used in Ref. [8].
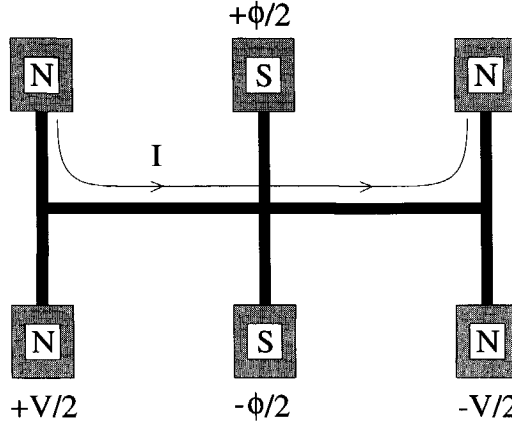

Figure 5.1: *The structure under consideration.*

The structure consists of the current branch, the superconducting branch connected to superconducting reservoirs biased at the phases $-\Phi/2,\Phi/2$ respectively, and the extra branch made for technological reasons. The current flows as indicated by the arrows in Fig. 5.1 and the voltage difference between the left and right voltage lead is measured. Due to the symmetry of the structure, the voltage and f distributions are antisymmetric with respect to the superconducting branch, whereas $\Delta(x)$ and $\hat{G}(x)$ are symmetric. Superconductivity in the structure gets completely suppressed when Φ approaches π.

The one-dimensional differential equations (5.1) and (5.2) must be solved for each branch and the solutions must then be matched in the nodes of the structure. First we calculate $\hat{G}(x,\varepsilon)$ in all points of the structure. Due to the boundary conditions, $\hat{G}$ depends on Φ in each point, which is the origin of the phase dependence. We obtain $\Delta(x)$ by integrating $\hat{G}$ over energy. Then we calculate $\gamma(x)$ and make use of an analytical formula that relates the resistance change to $\gamma(x)$. Details of the calculations will be reported elsewhere [14].

In Fig. 5.2 we have shown the calculated phase dependence normalized to its maximal value at $\delta\phi = 0$, $c(\phi)/c(0)$, together with the experimental data for Ag. The phase dependencies look similar, but the magnitude of the effect cannot be satisfactorily explained. According to the calculation, $c(0) = 0.14$. However, if we take the experimental value $g = 0.04$ for silver [13], we would obtain $\delta R_{\max}/R = -0.006$ whereas the experiment gives $\delta R_{\max}/R = -0.11$. If we do it the other way around and try to fit g from the experimental data, we end up with $g \simeq 0.7$. That would raise silver to the rank of high temperature superconductors.

This forced us to check the possibility that seems to have been rejected by the authors of Ref. [8]. We calculated the effect of Andreev reflection on the resistance neglecting interaction corrections. This effect arises from the energy dependence of the diffusion coefficient in Eq. (5.2). The calculation goes as follows. First we compute, using Eq. (5.1) and the definition of the renormalized diffusion coefficient, the actual energy-dependent diffusion
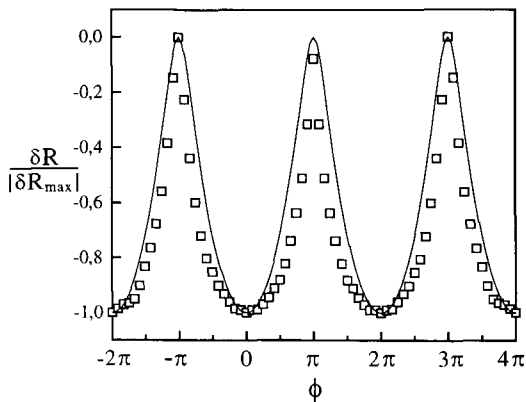
$\frac{\delta R}{|\delta R_{max}|}$

0,0
-0,2
-0,4
-0,6
-0,8
-1,0

-2π $-\pi$ 0 π 2π 3π 4π

ϕ

Figure 5.2: *Normalized phase dependence of the novel effect. Squares correspond to the experimental data of Ref. [8].*

coefficient throughout the structure. As we mentioned above, the zero-energy diffusion coefficient coincides with the one at high energy. The diffusion coefficient in a point separated by a distance d from the nearest superconductor has a maximum at energy $\simeq \mathcal{D}/d^2$. This maximum value exceeds the zero or high energy value by $\simeq \mathcal{D}$. Owing to the boundary conditions for Eq. (5.1), the diffusion coefficient also depends on the phase of the superconductors. Second, we solve Eq. (5.2) neglecting γ. The temperature enters the boundary condition for this equation and determines the energy interval in which the energy and phase dependence of the diffusion coefficient is actually felt by the propagating quasiparticles. Therefore we expect the effect to disappear at both low and high temperatures, exhibiting a minimal resistance at temperatures $\simeq \mathcal{D}/L^2$. In general, for a given geometry, the relative resistance change $\delta R/R$ is a function of L/ξ and ϕ.

Our numerical results are presented in Fig. 5.3. As expected, the effect vanishes at both low and high temperatures. The resistance at $\Phi = 0$ reaches its minimum at $L \approx 3\xi$. We have plotted the normalized phase dependence at $L = 3\xi$ along with the experimental data in Fig. 5.4 and obtain a perfect match. The maximal values of the change are also very close to each other: $(\delta R_{\max}/R)_{\text{theor}} = -0.097$ vs $(\delta R_{\max}/R)_{\text{exp}} = -0.11$. From the estimations given in Ref. [8] we obtain indeed $L/\xi = 2.5 - 3$ at $T = 20$ mK. As we can see in Fig. 5.3, the thermal effect persists at rather high temperatures, in agreement with the long high temperature tail observed in [8]. Unpublished data of the authors of [8] show excellent agreement with the curves plotted in Fig. 5.3 [15]. All this allows us to conclude that the experiment of Ref. [8] can be perfectly described by the existing semiclassical theory of superconducting proximity effect and thus to remedy the apparent discrepancy between theory and experiment.

The remaining discrepancy for metallic samples can be understood if one takes into account the inevitable inhomogeneity of these ultrasmall structures. This point of view is supported by large sample-to-sample fluctuations in the magnitude of the effect [8]. Understanding the results for the Sb samples, which have a rather high resistance, is difficult. However, we notice that all essential features for these samples, such as a small magnitude
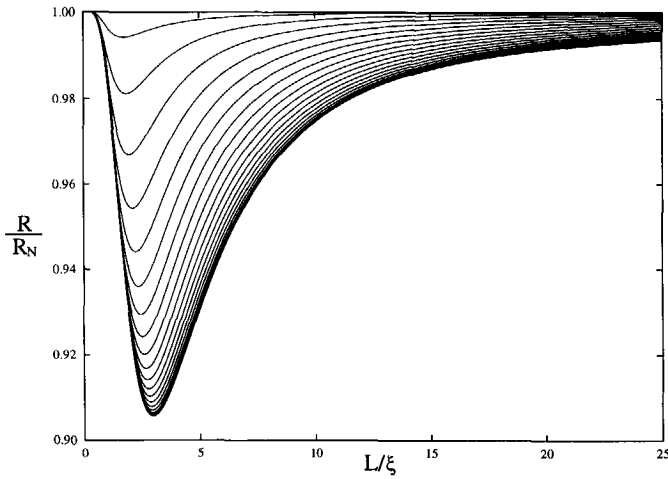
Figure 5.3: *Temperature and phase dependence of the thermal effect. The temperature is incorporated into $\xi^2 = \mathcal{D}/\pi T$. The phase difference changes from 0 for the lowermost curve to π for the uppermost one with step $\pi/20$.*
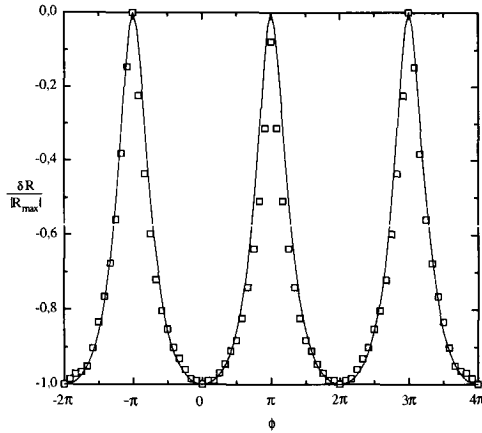
Figure 5.4: *Normalized phase dependence of the thermal effect at $L = 3\xi$. Squares correspond to the experimental data of Ref. [8].*

of the effect, sinusoidal phase dependence, positive sign, and the long high-temperature tail, can be well understood if the structures are not completely diffusive but contain tunnel junctions [4].

In conclusion, we have shown that the results of Ref. [8] can be explained within the existing theoretical framework and that they can be attributed to the thermal effect. Moreover, we have presented a new mechanism that causes a phase-dependent resistance in hybrid normal metal-superconductor structures at zero temperature. Observation of this

effect would allow a direct measurement of the interaction parameter in a normal metal. Our results also show that the observation of the weak localization correction [10] is a more difficult task than it was thought to be. At zero temperature, this correction will be masked by the novel effect we discussed, provided the interaction is not very small. At high temperatures, the correction would become comparable with the tail of the thermal effect at $T > \mathcal{D}R_Q/L^2R$. For the structures used in Ref. [8] this would correspond to unreasonably high temperatures of 20 K.

NOTE ADDED

Shortly after the publication of the results presented in this chapter, an interesting Comment, discussing an effect that may be present in the samples of Ref. [8], appeared [16]. The presence of this effect would influence the shape of the measured oscillations and, consequently, make it more difficult to interpret the experimental results. Let us briefly summarize the arguments of Ref. [16].

In the experimental setup of Ref. [8], the superconducting terminals are separated by a normal metal cross. The distance between the reservoirs is a few times the normal metal coherence length $\xi = \sqrt{D/\pi T}$. Because the superconducting electrodes are the end points of a large superconducting loop, a small circulating supercurrent can flow through the normal metal structure. The supercurrent is assumed to depend on the applied magnetic field by the first harmonic:

$$I_s = I_c \sin\left(2\pi \frac{\Phi_T}{\Phi_0}\right), \tag{5.5}$$

where I_c is the critical current, Φ_T is the total flux through the loop, and Φ_0 is the flux quantum $h/2e$. The circulating supercurrent will induce an extra flux $\mathcal{L}I_s$, where $\mathcal{L}$ is the self inductance of the loop. The total flux through the loop is then implicitly given by:

$$\Phi_T = \Phi_A - \mathcal{L}I_c \sin\left(2\pi \frac{\Phi_T}{\Phi_0}\right), \tag{5.6}$$

where Φ_A is the applied flux.

The response of the loop is determined by the parameter $\alpha = 2\pi \mathcal{L}I_c/\Phi_0$, (see Fig. 5.5). For $\alpha < 1$, the Φ_T-Φ_A curve is single valued and the total flux increases continuously with increasing applied flux, but in a strongly nonlinear fashion when α is close to 1. For $\alpha > 1$, the phase $\phi = 2\pi\Phi_T/\Phi_0$ no longer changes continuously, but jumps when a critical value ϕ_c is reached. As a result, only the range $-\phi_c \leq \phi \leq \phi_c$ can be scanned.

In order to account for the parabolic shape of the observed oscillations, Van Wees et al. assume the resistance change to depend sinusoidally on the phase difference ϕ between the
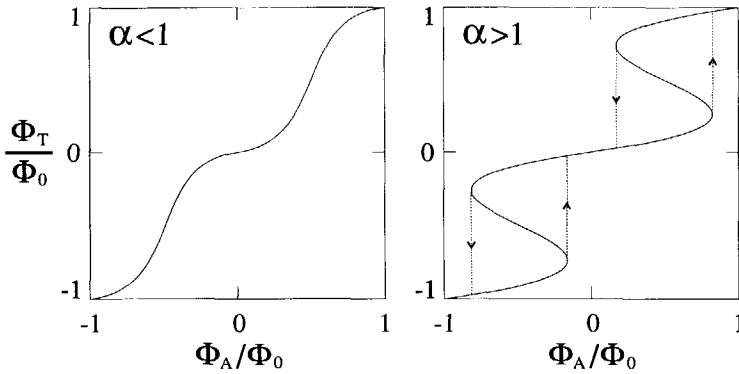
Figure 5.5: *The total flux Φ_T through a superconducting loop as a function of the applied flux Φ_A for $\alpha < 1$ and $\alpha > 1$. For details see text. The figure is copied from Ref. [17].*

superconducting electrodes:

$$\Delta R = -R_0 \cos \phi, \tag{5.7}$$

Hence, a circulating supercurrent does not change the *intrinsic* shape of the oscillations, but merely modifies the total flux through the loop, and thus the phase difference between the superconducting reservoirs. In the presence of a supercurrent, the resistance change becomes non-sinusoidal as a function of the *applied* flux. For small supercurrents ($\alpha < 1$), the cosine becomes broader at the bottom and narrower (but still smooth) at the top. When the supercurrent is large enough ($\alpha > 1$), the resistance is predicted to exhibit hysteretic behavior. In the presence of thermal activation the system may change between adjacent flux states. The resistance modulation should then display the symmetric phase dependence of a "partially scanned cosine" with narrow, sharp peaks at the top.

Recently, Petrashov *et al.* [18] reported experiments on new structures that are similar to the one described above. The phase dependence of the resistance change was measured for different temperatures in the range 1.3 K-4 K. One particular structure clearly showed hysteresis in the resistance change at $T = 1.3$ K, thus unequivocally proving the presence of a relatively large circulating supercurrent. At higher temperatures, the hysteretic behavior disappeared and the oscillations again resembled those in Fig. 5.4. In the same paper, however, measurements on a different but similar sample were presented, where the resistance change did neither exhibit the hysteretic behavior nor the "partially scanned cosine" form, thus showing no evidence for a large ($\alpha > 1$) supercurrent. In contrast, the oscillation's shape and magnitude show a temperature dependence that can be explained adequately by our theory. However, without detailed knowledge of the magnitude of the "supercurrent effect" in these samples, it is not possible to determine whether or not the intrinsic shape of the oscillations agrees with that predicted by our theory.

We would like to acknowledge discussions with Sander den Hartog, Bart van Wees, Alberto Morpurgo, and Teun Klapwijk.

REFERENCES

[1] C. J. Lambert, J. Phys.:Condens. Matter, **3**, 6579 (1991); C. W. J. Beenakker, Phys. Rev. B **46**, 12841 (1992).

[2] H. Nakano and H. Takayanagi, Sol. St. Comm. **80**, 997 (1991); C. W. J. Beenakker, J. Melsen, P. Brouwer, Phys. Rev. B **51**, 13883 (1995); A. Kadigrobov, A. Zagoskin, R. I. Shekhter, and M. Jonson, preprint, 1995; N. K. Allsopp, J. Sanchez Canizares, R. Raimondi, and C. J. Lambert, J. Phys.: Condens. Matter **8**, L377 (1996).

[3] F. W. J. Hekking and Yu. V. Nazarov, Phys. Rev. Lett. **71**, 1625 (1993); A. V. Zaitsev, Phys. Lett. A **194**, 315 (1994);

[4] Yu. V. Nazarov, Phys. Rev. Lett. **73**, 1420 (1994).

[5] H. Pothier, S. Guéron, D. Esteve, and M. H. Devoret, Phys. Rev. Lett. **73**, 2488 (1994).

[6] P. G. N. de Vegvar, T. A. Fulton, W. H. Mallison, and R. E. Miller, Phys. Rev. Lett. **73**, 1416 (1994).

[7] A. Dimoulas, J. P. Heida, B. J. van Wees, T. M. Klapwijk, W. v.d. Graaf, and G. Borghs, Phys. Rev. Lett. **74**, 602 (1995).

[8] V. T. Petrashov, V. N. Antonov, P. Delsing and T. Claeson, Phys. Rev. Lett. **74**, 5268 (1995).

[9] S. N. Artemenko, A. F. Volkov, and A. V. Zaitsev, Sol. St. Comm. **30**, 771 (1979); see also Refs. [1, 4].

[10] B. Z. Spivak and D. E. Khmelnitskii, Pis'ma Zh. Eksp. Teor. Fiz. **35**, 334 (1982) [JETP Lett. **35**, 412 (1982)].

[11] A. I. Larkin and Yu. V. Ovchinninkov, Zh. Eksp. Teor. Fiz. **68**, 1915 (1975) [Sov. Phys. JETP **41**, 960 (1975)]; A. I. Larkin and Yu. V. Ovchinninkov, Zh. Eksp. Teor. Fiz. **73**, 299 (1977) [Sov. Phys. JETP **46**, 155 (1977)];

[12] A. F. Volkov, A. V. Zaitsev, and T. M. Klapwijk, Physica C **210**, 21 (1993).

[13] A .C. Mota, P. Visani, and A. Pollini, Journ. of Low Temp. Phys., **76**, 465 (1989).

[14] T. H. Stoof and Yu. V. Nazarov, Phys. Rev. B **53**, 14496 (1996).

[15] P. Delsing, private communication.

[16] B. J. van Wees, S. G. den Hartog, and A. F. Morpurgo, Phys. Rev. Lett. **76**, 1402 (1996).

[17] A. Barone and G. Paterno, *Physics and Applications of the Josephson Effect* (Wiley, New York, 1981).

[18] V. T. Petrashov, R. Sh. Shaikhaidarov and I. A. Sosnin, in *Correlated Fermions and Transport in Mesoscopic Systems* edited by T. Martin, G. Montambaux, and J. Trân Thanh Vân (Editions Frontères, Gif-sur-Yvette Cedex, France 1996).

6

KINETIC-EQUATION APPROACH TO DIFFUSIVE SUPERCONDUCTING HYBRID DEVICES

T. H. Stoof and Yu. V. Nazarov

We present calculations of the temperature-dependent electrostatic and chemical potential distributions in disordered normal metal-superconductor structures. We show that they differ appreciably in the presence of a superconducting terminal and propose an experiment to measure these two different potential distributions. We also compute the resistance change in these structures due to a recently proposed mechanism which causes a finite effect at zero temperature. The relative resistance change due to this effect is of the order of the interaction parameter in the normal metal. Finally a detailed calculation of the resistance change due to the temperature dependence of Andreev reflection in diffusive systems is presented. We find that the maximal magnitude due to this thermal effect is in general much larger than the magnitude of the novel effect.

6.1   INTRODUCTION

Mesoscopic structures in which normal metal wires or semiconductors are attached to superconductors have received a fair amount of attention in the past few years. In particular devices known as Andreev interferometers, in which two superconducting terminals with different macroscopic phases are present, have been in the focus of interest. The conductance of these structures, in which electrons and holes undergo multiple Andreev reflection depends on the phase difference of the connected superconductors, hence the name Andreev interferometry.

Since the prediction of Andreev reflection [1] the theory of charge transport through N-S junctions has been well established [2, 3, 4]. However, the practical implications of this phenomenon for the sophisticated nano-structures that can nowadays be realized are not always clear. The reason for this is the coherent nature of multiple Andreev reflection which determines the physical behavior of these devices. These new technological developments resulted in the current revival of the topic in mesoscopic physics.

In the last few years a large number of Andreev interferometers have been studied both theoretically [5, 6, 7, 8, 9, 10, 11] and experimentally [12, 13, 14, 15]. Particularly the experiment of Ref. [15] motivated the research presented here. In this experiment, the resistance of a cross shaped diffusive normal metal was measured. The two branches of the cross perpendicular to the current path were in contact with a large superconducting loop. The phase difference between the superconducting end points of the loop could be controlled by a small current through the loop or, alternatively, by applying a magnetic field. The resistance of the structure oscillated non-harmonically as a function of the phase difference by about 10% of the normal state resistance. These results were unexpected because in the conventional theory of the proximity effect, in which electron-electron interactions in the normal metal region are disregarded, the zero-voltage, zero-temperature resistance of a diffusive metal is predicted to be phase-independent [16, 17]. Furthermore, the large amplitude and the observed 2π periodicity ruled out the possibility of a weak localization effect, since the latter was predicted to show a phase-dependence with a fundamental period of π [18, 19]. To this day, resistance oscillations with π periodicity remain unobserved.

Recently we proposed a new mechanism which provides a phase-dependent resistivity in a diffusive conductor at zero temperature [17]. This scheme takes into account the fact that the electron-electron interaction induces a weak pair potential in the normal metal. As a result, Andreev reflection occurs in the entire structure, rather than only at the N-S interfaces. This results in a phase-dependent resistance change which is proportional to the interaction parameter λ in the normal metal and can be of either sign, depending on the sign of λ. Although the experiment of Ref. [15] could be explained in terms of the proximity effect theory and the results were shown to be caused by the finite temperature at which the experiments were performed [17], it would be challenging to observe the resistance oscillations predicted in Ref. [17]. This would also be of practical interest since it would provide the means to directly measure the interaction parameter in the normal metal. However, besides the fact that electron-hole coherence influences the resistance, it also manifests itself in a non-trivial distribution of the electrostatic and chemical potentials in the structure as we will show below.

The remainder of this chapter is organized as follows. In section 6.2 we briefly discuss the influence of phase coherence on transport properties and potential distributions in small

diffusive structures. Section 6.3 contains the theoretical foundation of our calculations. We first review the relevant techniques of the Keldysh formalism for diffusive superconductors and then derive the equations for the Green functions and distribution functions which determine the electric transport properties of the system. The next three sections are devoted to several applications of the theory. We first calculate the temperature-dependent electrostatic and chemical potential distributions in a simple one dimensional structure in section 6.4. A second application is presented in section 6.5, where we calculate the resistance change at zero temperature due to the induced pair potential in the normal metal region for two experimentally relevant geometries. The third and last application is discussed in section 6.6. There we focus our attention on the influence of a finite temperature on the resistance in these structures. Some of the results in sections 6.5 and 6.6 were published in a preliminary form in Ref. [17]. However, here we additionally give a detailed description of the performed calculations. We summarize our conclusions in section 6.7.

6.2 COHERENCE EFFECTS IN ULTRASMALL DISORDERED STRUCTURES

Owing to the advance in nanofabrication techniques over the past years, the fabrication of hybrid metallic superconducting structures with a characteristic size of a few microns or less has nowadays become possible. If these small structures are at a sufficiently low temperature, the quasiparticles in the metal can no longer penetrate into the superconductor due to the large superconducting gap. As a result, the lowest order process that determines the resistance of the system is Andreev reflection, in which an electron is reflected as a hole or, alternatively, in which an electron pair enters the superconductor. This reflection causes electrons and holes in the diffusive metal to be phase coherent over distances of the order of $\xi = \sqrt{\mathcal{D}/T} \gg l$, where $\mathcal{D} = \frac{1}{3}v_\mathrm{F}l$ is the diffusion constant and l is the elastic mean free path.

This phase coherence between electrons and holes drastically alters the physics of transport through such systems. The most striking feature is that the electrostatic potential and nonequilibrium chemical potential are no longer distributed linearly through the sample. The nonlinearity of the electrostatic potential implies a nonuniform resistivity distribution and consequently a non-local resistance of the structure. This nonlocality is a fundamental feature of the coherent nature of Andreev reflection. Moreover, at finite temperatures the transport properties of the system cease to be distributed uniformly over all energies. Hence, a calculation of these quantities, to which the main part of this chapter will be devoted, must first consider them at each energy individually and then integrate over all energies.

Another manifestation of the phase coherence in the normal metal is the difference in the distribution functions of the electrostatic and chemical potentials. In a normal system both would be equal, but this changes when one of the leads is brought into the superconducting state. Whereas the former is simply determined by the distribution of charge in the system, the latter can only be defined for small perturbations from equilibrium, i.e. when the quasiparticle energies are much smaller than the superconducting gap. To show how this definition comes about we consider the normal current through a disordered N-I-S junction. Zhou, Spivak, and Zyuzin showed that for small quasiparticle energies ε this current can be

written in the following way: [20]

$$j(\varepsilon, x_N) = t \left\{ f_T(\varepsilon, x_S) - f_T(\varepsilon, x_N) \right\} F(\varepsilon, x_N, x_S), \tag{6.1}$$

where t is the transparency of the tunnel barrier, x_N and x_S denote the normal-metal side and superconducting side of the barrier, F is some function of ε, x_N and x_S, and f_T is the nonequilibrium distribution function. This equation shows that at low temperatures the nonequilibrium chemical potential can be associated with the distribution function and consequently that it is a measurable quantity. As will be discussed in section 6.4, the electrostatic potential decreases faster than linear in the vicinity of the superconductor due to the decreased density of states near the N-S interface. In contrast, the chemical potential changes only a little in the presence of a superconducting terminal and consequently the ratio of the electrostatic and chemical potential vanishes near the superconductor.

A possible experimental setup to measure the difference between the electrostatic and chemical potential is drawn in Fig. 6.1. The figure shows a diffusive wire connecting two reservoirs (not shown) in the presence of two different probes. The voltage probe measures the chemical and the capacitance probe the electrostatic potential. As shown in Fig. 6.1 (b), the voltage probe consists simply of a metallic lead separated from the wire by a thin oxide layer. The latter is indicated by the dark shaded region. The capacitance probe is slightly more complicated. In principle one could use a single metallic gate separated by a thick oxide layer to reduce tunneling from lead to wire. However, because such a gate would not only couple capacitively to the charge in the wire directly underneath the tip but also strongly to the surroundings, we propose a slightly different method: A small metallic island is deposited on the edge of the wire as indicated in the figure. This island is weakly coupled to two extra leads through which a current can flow. In this case the electrostatic potential capacitively induces a charge on the island, thus very sensitively changing the measured
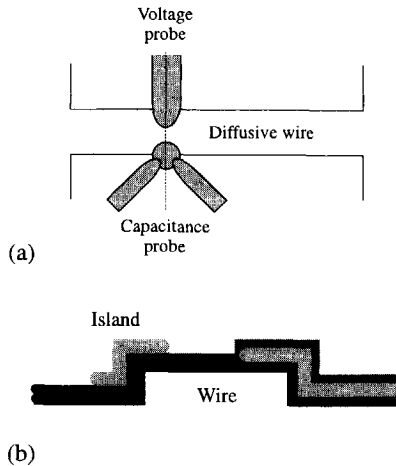

Figure 6.1: *Schematic setup of an experiment to measure the electrostatic and chemical potential: (a) Top view. (b) Cross section along the dashed line in (a). For details see text.*

Coulomb threshold. Both probes can be calibrated since they should measure the same potentials if both reservoirs are in the normal state. If one of the reservoirs is brought into the superconducting state, both potentials should change. If one would attach different probes along the wire it would be possible to measure the potential landscapes in the wire. In section 6.4 we will return to this subject in a more quantitative fashion, but we will now first discuss the necessary theory.

6.3 METHOD

6.3.1 KINETIC EQUATIONS FOR THE DISTRIBUTION FUNCTION IN THE DIRTY LIMIT

To describe the system we use the nonequilibrium Green function method first derived by Keldysh [21] and later further developed for superconductivity by Larkin and Ovchinnikov [22]. Although this framework is rather formal it has one big advantage over e.g. the scattering approach. As was mentioned above the resistance of the structure is nonlocal. However, using the Keldysh technique it is possible to express scattering processes in the structure as well as other relevant physical quantities, like the resistance, in terms of local Green functions in coincident points. This property of the formalism simplifies the calculations considerably. To establish notation and to remind the reader of the basic theory we briefly review the essential ingredients of the Keldysh formalism and the quasiclassical approximation for diffusive superconductors. For more extensive reviews we refer to e.g. Refs. [23] and [24].

In this formalism the Green function is given by the (4×4) matrix

$$\check{G} = \left(\begin{array}{cc} \hat{G}^{\mathrm{R}} & \hat{G}^{\mathrm{K}} \\ 0 & \hat{G}^{\mathrm{A}} \end{array} \right), \tag{6.2}$$

where $\hat{G}^{\mathrm{A}}, \hat{G}^{\mathrm{R}}$, and $\hat{G}^{\mathrm{K}}$ are the advanced, retarded, and Keldysh Green function which are (2×2) matrices in Nambu space given by [25]

$$\hat{G}^{\mathrm{A}}(1, 1') = \left(\begin{array}{cc} G^{\mathrm{A}}(1, 1') & F^{\mathrm{A}}(1, 1') \\ F^{\mathrm{A}\dagger}(1, 1') & -G^{\mathrm{A}}(1', 1) \end{array} \right), \tag{6.3}$$

and analogous equations for $\hat{G}^{\mathrm{R}}$ and $\hat{G}^{\mathrm{K}}$. Throughout this chapter the symbol "check" will be used to denote (4×4) matrices and "hat" for (2×2) matrices. The normal and anomalous Green function are given by:

$$
\begin{align}
G^{\mathrm{R}}(1, 1') &= -i\theta(t_1 - t_{1'})\langle[\psi(1), \psi^\dagger(1')]_+\rangle, \tag{6.4} \\
G^{\mathrm{A}}(1, 1') &= i\theta(t_{1'} - t_1)\langle[\psi(1), \psi^\dagger(1')]_+\rangle, \tag{6.5} \\
G^{\mathrm{K}}(1, 1') &= -i\langle[\psi(1), \psi^\dagger(1')]\rangle, \tag{6.6} \\
F^{\mathrm{R}}(1, 1') &= -i\theta(t_1 - t_{1'})\langle[\psi(1), \psi(1')]_+\rangle, \tag{6.7} \\
F^{\mathrm{A}}(1, 1') &= i\theta(t_{1'} - t_1)\langle[\psi(1), \psi(1')]_+\rangle, \tag{6.8} \\
F^{\mathrm{K}}(1, 1') &= i\langle[\psi^\dagger(1), \psi^\dagger(1')]\rangle, \tag{6.9}
\end{align}
$$

where $\psi(1) = \psi(t_1, \mathbf{r}_1)$ is the electron field operator.

We proceed by introducing the center-of-mass and relative coordinates $\mathbf{r} = \frac{1}{2}(\mathbf{r}_1 + \mathbf{r}_{1'})$ and $\mathbf{r}' = \mathbf{r}_1 - \mathbf{r}_{1'}$ and by Fourier transforming the Green function with respect to the relative coordinate: $\check{G}(\mathbf{r}, \mathbf{p}) = \int d\mathbf{r}' \exp(-i\mathbf{p}\mathbf{r}')\, \check{G}(\mathbf{r} + \frac{1}{2}\mathbf{r}', \mathbf{r} - \frac{1}{2}\mathbf{r}')$. We apply the quasiclassical approximation, which is based on the fact that the Fermi energy in the system is much larger than all other energy scales. This means that all relevant physical quantities vary spatially on a length scale that is much larger than the Fermi wavelength. In this case it is useful to introduce the so-called quasiclassical Green function $\check{g}$ which is integrated over $\xi_{\mathbf{p}} = \frac{\mathbf{p}^2}{2m} - \mu$:

$$\check{g}(\mathbf{r}, \hat{p}, t_1, t_{1'}) = \frac{i}{\pi} \int d\xi_{\mathbf{p}} \check{G}(\mathbf{r}, \mathbf{p}, t_1, t_{1'}). \tag{6.10}$$

Here $\hat{p}$ in the left hand side denotes the fact that the momentum dependence of the quasiclassical Green function is restricted to dependence on the direction of $\mathbf{p}$ only. In this approximation the magnitude of the momentum is fixed at $|\mathbf{p}| = p_{\mathrm{F}}$. This quasiclasissical Green function satisfies the normalization condition

$$\int dt_{1''} \check{g}(t_1, t_{1''}) \check{g}(t_{1''}, t_{1'}) = \check{1} \delta(t_1 - t_{1'}). \tag{6.11}$$

In the case of a superconductor with short elastic mean free path, i.e. in the diffusive regime, it is feasible to expand the Green function to first order in spherical harmonics: [26]

$$\check{g} = \check{g}_s + \mathbf{p}\check{g}_p, \quad \mathbf{p}\check{g}_p \ll \check{g}_s, \tag{6.12}$$

where the functions $\check{g}_s$ and $\check{g}_p$ no longer depend on the direction of $\mathbf{p}$. Using the normalization condition (6.11) we find an expression for $\check{g}_p$, which is then substituted back into Eq. (6.12). The thus obtained Green function is then averaged over all angles of $\mathbf{p}$. In the stationary case, the Green function depends on the time difference $\tau = t_1 - t_{1'}$ only. Performing the Fourier transform with respect to this time difference, we obtain the equation of motion for the Green function $\check{g}_\varepsilon = \int d\tau \check{g}_s(\tau) \exp(i\varepsilon\tau)$ (we drop the index "s" from now on) [27]

$$- \mathcal{D}\nabla \left(\check{g}_\varepsilon \nabla \check{g}_\varepsilon \right) + i[\check{H}, \check{g}_\varepsilon] + i[\check{\Sigma}, \check{g}_\varepsilon] = 0, \tag{6.13}$$

$$\check{g}_\varepsilon^2 = \check{1}, \tag{6.14}$$

where $\mathcal{D} = \frac{1}{3} v_{\mathrm{F}} l$ is the diffusivity, l is the elastic mean free path, $\check{H} = e\varphi\check{1} + \varepsilon\check{\sigma}_z - \check{\Delta}$ and $\check{\Delta}$ and $\check{\sigma}_z$ are given by:

$$\check{\Delta} = \begin{pmatrix} \hat{\Delta} & 0 \\ 0 & \hat{\Delta} \end{pmatrix}, \hat{\Delta} = \begin{pmatrix} 0 & \Delta \\ -\Delta^* & 0 \end{pmatrix}, \tag{6.15}$$

where Δ is the pair potential in the metal and

$$\check{\sigma}_z = \begin{pmatrix} \hat{\sigma}_z & 0 \\ 0 & \hat{\sigma}_z \end{pmatrix}, \hat{\sigma}_z = \begin{pmatrix} 1 & 0 \\ 0 & -1 \end{pmatrix}. \tag{6.16}$$

In Eq. (6.13) elastic non spin-flip impurity scattering has been taken into account in the Born approximation, causing the presence of the elastic mean free path l in the diffusion constant [24]. Hence, the self energy matrix $\check{\Sigma}$ in Eq. (6.13), which has the same structure

as the Green function (6.2), takes into account processes like spin-flip scattering and the inelastic scattering of electrons with phonons and (magnetic) impurities.

The general expression for the electrostatic potential φ in Eq. (6.13), which follows from electroneutrality in the metal, is [24, 20]

$$\varphi(x) = -\frac{1}{8e} \int_{-\infty}^{\infty} d\varepsilon \ \text{Tr} \ \hat{g}_{\varepsilon}^{\text{K}}(x). \tag{6.17}$$

Throughout the chapter the electrostatic potential is assumed to be time-independent.

The advanced and retarded Green functions determine the dispersion of the quasiparticles. However, to solve a transport problem we need to know how the energy spectrum is filled by extra quasiparticles when the system is driven out of equilibrium. This is determined by the Keldysh component $\hat{g}^{\text{K}}$ of $\check{g}$, which can be expressed in the advanced and retarded ones using two distribution functions: [22, 23, 24]

$$\hat{g}_{\varepsilon}^{\text{K}} = \hat{g}_{\varepsilon}^{\text{R}} \hat{f} - \hat{f} \hat{g}_{\varepsilon}^{\text{A}} \tag{6.18}$$

$$\hat{f} = f_{\text{L}} \hat{1} + f_{\text{T}} \hat{\sigma}_z. \tag{6.19}$$

In a spatially slowly varying electro-magnetic field, the equations for the two distribution functions are (dropping collision integrals because they account for inelastic scattering processes, and time derivatives because we seek to find stationary solutions only):

$$\mathcal{D}\nabla \text{Tr} \left\{ \nabla f_{\text{L}}(\hat{1} - \hat{g}_{\varepsilon}^{\text{R}} \hat{g}_{\varepsilon}^{\text{A}}) \right\} + \mathcal{D}\nabla \left(f_{\text{T}} j_{\varepsilon} \right) = 0 \tag{6.20}$$

$$\mathcal{D}\nabla \text{Tr} \left\{ \nabla f_{\text{T}}(\hat{1} - \hat{\sigma}_z \hat{g}_{\varepsilon}^{\text{R}} \hat{\sigma}_z \hat{g}_{\varepsilon}^{\text{A}}) \right\} + \mathcal{D}\nabla f_{\text{L}} j_{\varepsilon} + 2i f_{\text{T}} \text{Tr} \left\{ (\hat{g}_{\varepsilon}^{\text{R}} + \hat{g}_{\varepsilon}^{\text{A}}) \hat{\Delta} \right\} = 0 \tag{6.21}$$

where $j_{\varepsilon} = \text{Tr} \hat{\sigma}_z \{ \hat{g}_{\varepsilon}^{\text{R}} \hat{\partial} \hat{g}_{\varepsilon}^{\text{R}} - \hat{g}_{\varepsilon}^{\text{A}} \hat{\partial} \hat{g}_{\varepsilon}^{\text{A}} \}$.

To close the set of equations we finally need an equation for the pair potential in the normal metal region. This expression for Δ can be derived from the selfconsistency relation:

$$\hat{\Delta}(\mathbf{r}) = \frac{\lambda}{4i} \int d\varepsilon \left\{ \hat{g}_{\varepsilon}^{\text{K}}(\mathbf{r}, \hat{p}, \tau) \right\}_{\text{o.d}} = \frac{\lambda}{4i} \int d\varepsilon \tanh \left(\frac{\varepsilon}{2T} \right) \left\{ \hat{g}_{\varepsilon}^{\text{R}} - \hat{g}_{\varepsilon}^{\text{A}} \right\}_{\text{o.d}}, \tag{6.22}$$

where $\lambda = gN(0)$ is the interaction parameter, g, times the density of states at the Fermi level, $N(0)$. The subscript o.d. denotes the off-diagonal part.

This concludes the derivation of the distribution functions. We now have a closed system of equations that in principle must be solved selfconsistently. In the next section we will discuss specific circumstances that allow for a simplification of the equations, enabling us to solve them perturbatively.

6.3.2 Approximations

In this section we discuss the assumptions and approximations that enable us to simplify the theory. We subsequently derive the final set of equations that we will use.

We start by noting that Eq. (6.13) for the Green function still contains the self energy matrix $\check{\Sigma}$. However, because we are only interested in the case where the phase breaking length is much larger than the system size, it is reasonable to disregard inelastic scattering processes and hence, we neglect $\check{\Sigma}$ from now on. Eq. (6.13) then reduces to [17]

$$\mathcal{D}\nabla \left(\check{g}_{\varepsilon} \nabla \check{g}_{\varepsilon} \right) - i[\check{H}, \check{g}_{\varepsilon}] = 0. \tag{6.23}$$

We now have equations for the diagonal components $\hat{g}^{A}_{\varepsilon}$ and $\hat{g}^{R}_{\varepsilon}$ of the Green function (6.2).

We parametrize the advanced Green function in the following way:

$$\hat{g}^{A}_{\varepsilon} = \begin{pmatrix} \cos\theta & ie^{i\phi}\sin\theta \\ -ie^{-i\phi}\sin\theta & -\cos\theta \end{pmatrix}, \tag{6.24}$$

thus ensuring that $\hat{g}^{2}_{\varepsilon} = \hat{1}$. In general ϕ and θ are complex and depend on energy and position. In a structure with two superconducting terminals, $\hat{g}^{A}_{\varepsilon}$ will depend on the phase *difference* $\phi_1 - \phi_2$ between the two superconductors. However, if only one superconducting reservoir is present, the resistance of the structure will not depend on the absolute phase and we can put $\phi = 0$.

For sufficiently small quasiparticle, thermal and Thouless energies; $\varepsilon, k_{B}T, \mathcal{D}/L^{2} \ll \Delta_{S}$, where Δ_{S} is the energy gap in the superconductor, the advanced Green function can be written in the following way: [22]

$$\hat{g}^{A}_{\varepsilon} = \frac{-1}{\sqrt{(\varepsilon - i\delta)^{2} - |\Delta|^{2}}} \begin{pmatrix} \varepsilon & \Delta \\ -\Delta^{\star} & -\varepsilon \end{pmatrix}, \tag{6.25}$$

where δ is an infinitesimally small positive number. Using this representation for $\hat{g}^{A}_{\varepsilon}$ it is easy to derive boundary conditions for Eq. (6.23). In a normal reservoir $\Delta = 0$ and $\hat{g}^{A}_{\varepsilon} = -\hat{\sigma}_{z}$. In a superconducting terminal having phase ϕ, $\Delta = |\Delta_{S}|e^{i\phi}$ and the Green function satisfies $\hat{g}^{A}_{\varepsilon} = \hat{\sigma}_{x}\sin\phi + \hat{\sigma}_{y}\cos\phi$.

It is also possible to simplify Eq. (6.20) for the distribution functions considerably: In the case of a negligible supercurrent $I_{s} = \int j_{\varepsilon}d\varepsilon$ the equations for the two distribution functions decouple, reducing f_{L} to its equilibrium value $f_{L} = \tanh(\frac{\varepsilon}{2T})$ and leaving us with a single equation for f_{T} which can be cast into the form of a diffusion equation [17]:

$$\nabla\left(D(\varepsilon, \mathbf{r})\nabla f_{T}(\varepsilon, \mathbf{r})\right) - \gamma(\varepsilon, \mathbf{r})f_{T}(\varepsilon, \mathbf{r}) = 0, \tag{6.26}$$

where the first term describes diffusion of quasiparticles with an effective diffusion coefficient

$$D(\varepsilon, \mathbf{r}) = \frac{\mathcal{D}}{4}\mathrm{Tr}\{\hat{1} - \hat{\sigma}_{z}\hat{g}^{R}_{\varepsilon}\hat{\sigma}_{z}\hat{g}^{A}_{\varepsilon}\} = \frac{\mathcal{D}}{8}\mathrm{Tr}\{(\hat{g}^{A}_{\varepsilon} + \hat{g}^{A\dagger}_{-\varepsilon})^{2}\}, \tag{6.27}$$

that is modified by the penetrating superconductivity. Here we have used the identity $\hat{g}^{R}_{\varepsilon} = -\hat{\sigma}_{z}\hat{g}^{A}_{-\varepsilon}\hat{\sigma}_{z}$, which relates the advanced and retarded Green functions. The second term describes absorption of quasiparticles in the superconducting condensate with a coefficient $\gamma = \frac{i}{2}\mathrm{Tr}\{(\hat{g}^{R}_{\varepsilon} + \hat{g}^{A}_{\varepsilon})\hat{\Delta}\}$. In the absence of external fields γ is proportional to the local value of the pair potential, since in that case we can always choose Δ to be real, and we obtain

$$\gamma(\mathbf{r}, \varepsilon) = -\frac{i}{2}\Delta(\mathbf{r})\mathrm{Tr}\{i\hat{\sigma}_{y}(\hat{g}^{A}_{-\varepsilon} + \hat{g}^{A}_{\varepsilon})\}. \tag{6.28}$$

The boundary conditions for Eq. (6.26) follow from expanding $\tanh(\frac{\varepsilon + eV}{2T})$ to first order in V. This determines the boundary condition for f_{T}. In a normal reservoir that is biased at a (small) voltage V with respect to a superconducting lead, the distribution function is $f_{T} = (\frac{eV}{2T})\cosh^{-2}(\frac{\varepsilon}{2T})$.

In most theoretical approaches, see e.g. Refs. [3, 4, 10, 27], electron-electron interactions in the normal metal are disregarded, leading to $\Delta, \gamma = 0$. However, as shown in Ref. [17],

including the effect of these interactions produces a change in the resistance. We thus need Eq. (6.22) for Δ, which after a straightforward calculation can be rewritten as:

$$\Delta = \frac{\lambda}{8i} \int d\varepsilon \, \tanh\left(\frac{\varepsilon}{2T}\right) \text{Tr}\left\{i\hat{\sigma}_y(\hat{g}_\varepsilon^{\text{A}} - \hat{g}_\varepsilon^{\text{R}})\right\}. \tag{6.29}$$

We now have all the necessary ingredients to calculate the various non-equilibrium transport properties of the system. The next section will be devoted to two of these properties, namely the electrostatic and chemical potential distributions.

6.4 ELECTROSTATIC VERSUS CHEMICAL POTENTIAL

As a first example of the theory of section 6.3 we calculate the electrostatic and the chemical potential in the 1D wire of Fig. 6.2 (a). As was shown above, the former is determined by the distribution of electric charge in the wire. The latter determines the magnitude of the current that flows through the sample. The system consists of a diffusive normal metal wire of length L attached on the left to a normal metal reservoir and on the right to a superconducting terminal. The normal lead is biased at a small voltage V with respect to the superconductor. The normal reservoir is situated at $x = 0$.
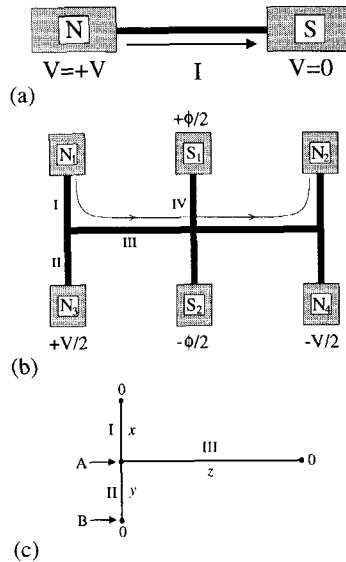

Figure 6.2: *(a) The simplest possible system, consisting of a diffusive normal metal wire of length L, that is connected on the left to a normal reservoir and to the right to a superconducting one. (b) An example of a more complicated structure. The branches I, II and IV have length L', branch III has length L. For further details see text. (c) The coordinates on the branches. The origins are indicated for each branch.*

Using Eq. (6.18) for the Keldysh component and Eq. (6.24) for the Green function we obtain

$$\varphi(x) = \frac{1}{e} \int_0^\infty d\varepsilon \, f_{\rm T}(x,\varepsilon) \cos(\theta(x,\varepsilon)). \tag{6.30}$$

In Fig. 6.3 we have calculated the potential distribution in the normal metal for different values of L/ξ, i.e. for different temperatures. In the limiting cases of low and high temperatures, the potential can be calculated analytically:

$$\varphi(x) = V \left(1 - \frac{x}{L} \right) \cos \left(\frac{\pi x}{2L} \right), \; T \to 0, \tag{6.31}$$

$$\varphi(x) = V \left(1 - \frac{x}{L} \right), \; \frac{\mathcal{D}}{L^2} \ll k_{\rm B} T \ll \Delta_{\rm S}. \tag{6.32}$$

Fig. 6.3 shows that the potential distribution changes with temperature from a non trivial one which is influenced strongly by the penetrating superconductivity to the expected linear dependence for high temperatures (but still $k_{\rm B}T \ll \Delta_{\rm S}$). This behavior is caused by the
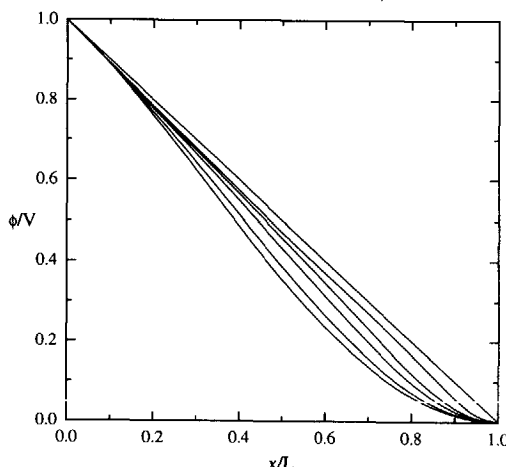

Figure 6.3: *Electrical potential distribution in the wire of Fig. 6.2 (a) as a function of temperature. Going from bottom to top, the curves correspond to values of $L/\xi = 0$, 1.0, 1.5, 2.0, 4.0, and ∞. The temperature is proportional to $(L/\xi)^2$.*

fact that the density of states vanishes in the vicinity of the superconductor. Hence, the charge distribution which causes the electrostatic potential also vanishes in this region. The most important consequence of the nonlinear voltage distribution across the sample is the fact that the resistance at a certain point is no longer local, but depends on the distribution of resistivity in the entire structure. This is a direct consequence of the coherent nature of Andreev reflection as was discussed above.

The chemical potential, which is simply proportional to the energy integrated distribution function, is much less sensitive to changes in temperature. The zero and high temperature distributions are the same and are given by

$$\mu_0(x) = V \left(1 - \frac{x}{L} \right). \tag{6.33}$$

In Fig. 6.4 we have plotted the deviation of the chemical potential from this zero temperature solution. First of all we note that the change is very small. The maximum change at first
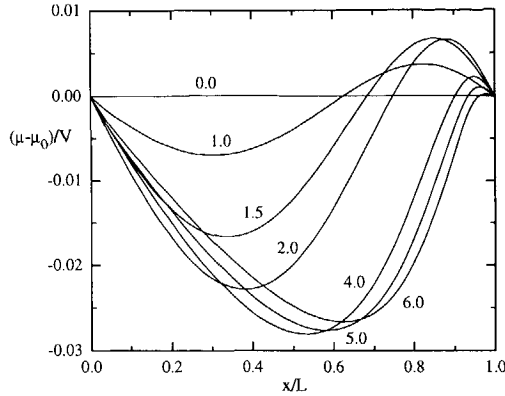

Figure 6.4: *Change in the chemical potential for the wire of Fig. 6.2 (a) relative to the (linear) zero temperature distribution as a function of temperature. The labels near the curves indicate the value of L/ξ.*

increases rapidly with increasing temperature. However, beyond a certain temperature, $L/\xi \approx 4$, the maximum starts decreasing slowly. For high temperatures, the solution returns to the linear distribution. Thus we see that the electrostatic and chemical potential are only equal in the case of high temperatures, when both reduce to the trivial linear dependence that is also exhibited in the case of two normal terminals.

To indicate more clearly the difference between electrostatic and chemical potential, we have plotted the ratio of the two for different temperatures in Fig. 6.5. The electrostatic and chemical potential differ most at low temperatures and near the superconductor. However, in the vicinity of the normal reservoir they are almost equal and the extent into the wire at which they are equal increases at higher temperatures. In the high temperature limit they both reduce to the same linear distribution, as was shown above.

6.5   THE INTERACTION EFFECT

6.5.1   THE RESISTANCE OF A 1D WIRE

In this section we calculate the resistance change at zero temperature due to the penetration of the pair potential into the normal metal region. We first consider the wire of Fig. 6.2 (a) and then address more general geometries. In order to simplify the equations later on, the superconducting end of the wire is now located at $x = 0$ and the normal end at $x = L$.

We first solve Eq. (6.23) for $\hat{g}^{A}$ numerically to zeroth order in Δ and φ:

$$\mathcal{D}\nabla\left(\hat{g}_{\varepsilon}^{A}\nabla\hat{g}_{\varepsilon}^{A}\right) - i\varepsilon[\hat{\sigma}_z ; \hat{g}_{\varepsilon}^{A}] = 0, \tag{6.34}$$
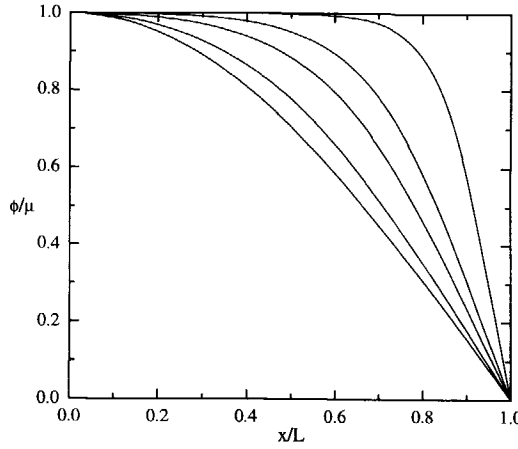
Figure 6.5: *The ratio of electrostatic and chemical potential as a function of temperature. Going from bottom to top, the curves correspond to values of $L/\xi = 0$, 1.0, 1.5, 2.0, and 4.0.*

where $\varphi = 0$ (zero voltage limit) and Δ has been disregarded since it is small in the normal metal region because of its proportionality to the interaction parameter λ. We then solve Eq. (6.26) to first order in γ. At zero temperature, $D(\varepsilon, x) = \mathcal{D}$, and we write $f_T = f_0 + f_1$ with $f_1 \ll f_0$. Then $f_0 = c(\varepsilon)\frac{x}{L}$ and $f_1'' = \frac{\gamma}{\mathcal{D}} f_0$, with $c(\varepsilon) = \frac{eV}{4T} \cosh^{-2}(\frac{\varepsilon}{2T})$. Using the fact that $\int_0^L f_1'(x')dx' = 0$ ($f_1(0) = f_1(L) = 0$) we find

$$f_0'(L) = \frac{c(\varepsilon)}{L}, \tag{6.35}$$

$$f_1'(L) = \frac{c(\varepsilon)}{\mathcal{D}L^2} \int_0^L x^2 \gamma(x) dx. \tag{6.36}$$

The current in a normal piece of metal is proportional to the local gradient of f. Since everywhere in the diffusive wire there is an induced pair potential it is not possible to calculate the current in this way somewhere in the middle of the wire. We must calculate it at the normal reservoir, where the pair potential is forced to vanish. The current flowing out of the normal reservoir (and hence the conductance G of the system) is therefore proportional to $f'(L)$. Noting that $\frac{\delta R}{R} = -\frac{\delta G}{G}$ we obtain for the relative resistance change:

$$\frac{\delta R}{R} = -\frac{f_1'(L)}{f_0'(L)} = -\frac{1}{\mathcal{D}L} \int_0^L dx \; x^2 \; \gamma(x), \tag{6.37}$$

where γ is given by

$$\gamma(x) = 2\Delta(x) \sin(\theta(\varepsilon = 0, x)). \tag{6.38}$$

Thus the relative resistance change is proportional to the interaction parameter λ and its sign depends on the sign of λ. Here we use the convention that λ is positive for attractive effective interactions in the metal. Furthermore, the resistance change depends sensitively

on the precise geometry of the structure, as will be shown in more detail in the next section. A measurement of this resistance change would allow one to directly measure λ. Calculating the relative resistance change for the wire of Fig. 6.2 (a) gives

$$\frac{\delta R}{R} = -1.38\lambda, \tag{6.39}$$

independent of $\mathcal{D}$ and L. For silver, the estimated value of the interaction parameter is $\lambda = +0.04$ [28], and therefore the resistance of a silver wire in contact with a superconductor is reduced by 5.5% with respect to its normal state value.

6.5.2 GENERALIZATION TO ARBITRARY GEOMETRIES

The results obtained above are readily generalized for arbitrary structures containing a number of normal reservoirs, two superconducting ones and a number of diffusive wires connecting them. To illustrate how the resistance change for such systems is calculated we consider the geometry shown in Fig. 6.2 (b). This is a structure similar to the one we used recently [17] to model the experimental setup of Ref. [15]. In the experiment a current was applied along the path indicated by the arrow going from normal lead N_1 to normal lead N_2. The voltage was measured between the opposite normal reservoirs N_3 and N_4. The superconductors have a phase difference ϕ. In principle Eqs. (6.23) and (6.26) should be solved in each branch of the structure and the solutions matched in every nodal point. However, it is possible to reduce this geometry to a one dimensional one due to the symmetry of the geometry: The voltage and f_{T} distributions are antisymmetric with respect to the line $S_1 - S_2$ in Fig. 6.2 (b) whereas Δ and the Green function $\hat{g}_\varepsilon$ are symmetric. This allows us to consider only the three elementary branches I, III, and IV in the calculation of $\hat{g}_\varepsilon$.

For the calculation of the resistance change we need only consider the branches I and II, each having a length L', and III which has a length L. As depicted in Fig. 6.2 (c) we use coordinates x, y and z to denote the position on branch I, II and III, respectively. with the origins as indicated. The zeroth order solution of Eq. (6.26) is

$$f_0 = \begin{cases} L + L' - x & \text{(I)}, \\ L & \text{(II)}, \\ z & \text{(III)}. \end{cases} \tag{6.40}$$

Integrating $f_1'' = \frac{\gamma}{\mathcal{D}} f_0$ in each branch gives

$$f_1' = \begin{cases} c_1 + \int_0^x dx' \, (L + L' - x') \, \frac{\gamma(x')}{\mathcal{D}} & \text{(I)}, \\ c_2 + \int_0^y dy' \, L \, \frac{\gamma(y')}{\mathcal{D}} & \text{(II)}, \\ c_3 + \int_0^z dz' \, z' \, \frac{\gamma(z')}{\mathcal{D}} & \text{(III)}. \end{cases} \tag{6.41}$$

Here the integration constant $c_1 = 0$ because the current in point $x = 0$ is fixed and $c_2 = 0$ because there is no current in branch II. Note that the situation here is different from the one in section 6.5.1. There we calculated the change in current at fixed voltage whereas in this case we calculate the voltage change at fixed current. Consequently the resistance

change is now given by $\frac{\delta R}{R} = \frac{\delta V}{V} = \frac{f_1(B)}{f_0(B)}$. In the nodal point A we have $f_1'(x = L') + f_1'(y = L') + f_1'(z = L) = 0$ and this gives

$$c_3 + \int_0^L dz \frac{z\gamma(z)}{\mathcal{D}} + \int_0^{L'} dy \frac{L\gamma(y)}{\mathcal{D}} + \int_0^{L'} dx \frac{(L + L' - x)\gamma(x)}{\mathcal{D}} = 0. \tag{6.42}$$

The distribution function f_1 in point A is now given by

$$f_1(A) = c_3 \int_0^L dz + \int_0^L dz \int_0^z dz' \frac{z'\gamma(z')}{\mathcal{D}} = c_3 L + \int_0^L dz \frac{Lz - z^2}{\mathcal{D}} \gamma(z). \tag{6.43}$$

Analogously we find for $f_1(B)$:

$$f_1(B) = f_1(A) - \int_0^{L'} dy \int_0^y dy' \frac{Ly'\gamma(y')}{\mathcal{D}} = f_1(A) - \int_0^{L'} dy \frac{y^2 - LL'}{\mathcal{D}} \gamma(y). \tag{6.44}$$

Using Eq. (6.42) to eliminate the first two terms in expression (6.43) for $f_1(A)$ we calculate the resistance change:

$$\frac{\delta R}{R} = \int_0^{L'} dy \left(\frac{y^2}{L} - L - L' \right) \frac{\gamma(y)}{\mathcal{D}} - \int_0^L dz \frac{z^2 \gamma(z)}{\mathcal{D}L} - \int_0^{L'} dx \frac{(L + L' - x)\gamma(x)}{\mathcal{D}}. \tag{6.45}$$

The relative resistance change depends on the phase difference ϕ between the superconductors through γ, which in its turn depends on ϕ via the boundary conditions imposed on $\hat{g}_\varepsilon$. Note that although branch IV does not enter the calculation of the resistance change, its length does influence the Green function, hence γ, and thus also the resistance of the structure.

Before discussing the results of a calculation for an experimentally relevant geometry, it is instructive to look at the (slightly unrealistic) case of constant γ to investigate the qualitative behavior of the system. In this case the resistance change reduces to

$$\frac{\delta R}{R} = \frac{\gamma L^2}{\mathcal{D}} \left(\frac{1}{3}\alpha^3 - \frac{3}{2}\alpha^2 - 2\alpha - \frac{1}{3} \right) \text{ with } \alpha = \frac{L'}{L} \tag{6.46}$$

which shows that, since $\gamma \sim \lambda \frac{\mathcal{D}}{L^2}$, the relative resistance change is proportional to the interaction parameter and independent of the absolute values of L, L' and $\mathcal{D}$. Only the ratio of L and L' is important. In this simple case the largest effect would be obtained for $\alpha = 3.56$. We can get an idea how sensitive the resistance change is to the details of the geometry by comparing the cross structure ($L' = 0$) with the structure in which $L' = L$. It is easily calculated that the resistance change is higher in the latter case by a factor of 10.5, showing that a relatively small change in geometry causes a major modification of the resistance change. In a realistic computation the modification due to these side branches is not so dramatic, but is still about a factor 3.

The result of such a realistic calculation is depicted in Fig. 6.6 where the scaled resistance change has been plotted for the Andreev interferometer of Fig. 6.2 (b) with $L_I = L_{II} = L_{III} = L_{IV} = L$. This layout is similar to the one we used in Ref. [17] to model the experimental setup of Petrashov *et al.*

There are two main differences with the previous results for the one dimensional wire. The first is the dependence of the resistance change on the phase difference ϕ between the
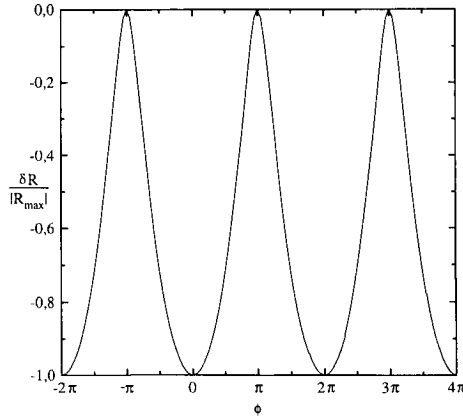
Figure 6.6: *The scaled resistance change due to the interaction effect of the structure shown in Fig. 6.2 (b) with $L_I = L_{II} = L_{III} = L_{IV} = L$. The magnitude of the effect is 0.9%.*

superconductors with oscillation period 2π. The effect has its largest (negative) value for zero phase difference and vanishes for a phase difference of π, when superconductivity in the current branch (branches I, II, and their mirror images) is completely suppressed. The second difference is the magnitude of the effect. In the one dimensional case this was 5.5%. Here it is 0.9% (for silver). Although this value is proportional to the interaction parameter and strongly depends on the length of the branches I and II, as was established above, a more important reason in this case is that the superconductors are not in the current path. As a consequence, the pair potential in branches I and II is smaller than in the one dimensional case, leading to a weaker effect. In general, the magnitude of the interaction effect is smaller than the influence of a finite temperature on the resistance. This latter phenomenon is the subject of the next section.

6.6   THE THERMAL EFFECT

6.6.1   THE TEMPERATURE-DEPENDENT RESISTANCE OF A 1D WIRE

As was shown recently by the authors [17], the experimental results of Ref. [15] could be explained by the temperature-dependent proximity effect. In this case no pair potential is induced in the normal metal region by the electron-electron interaction but coherence occurs as a result of the finite extent $\xi = \sqrt{\mathcal{D}/T}$ at which the superconductivity penetrates into the normal metal. Although the implications of this effect for complex structures are not always immediately apparent, the mechanism itself is not new. It was already studied in the middle seventies [16] and is in fact the phenomenon of Andreev reflection in diffusive metals. In spite of the fact that the effect has been known for a long time, a clear physical picture is still lacking.

To describe this effect we disregard the second term in Eq. (6.26) but we now take into ac-

count the fact that at finite temperatures the effective diffusion coefficient is no longer simply a constant but that it depends on energy and position: $D(\varepsilon, x) = \frac{\mathcal{D}}{8} \text{Tr}\{(\hat{g}_\varepsilon^A(x) + \hat{g}_{-\varepsilon}^{A\dagger}(x))^2\}$. The diffusion coefficient reduces to $\mathcal{D}$ for low and high energies. For energies $\varepsilon \approx \mathcal{D}/L^2$ it exhibits a maximum which is about twice as large as the zero energy value. The temperature enters the boundary conditions for Eq. (6.26), but more importantly it determines the energy window in which the quasiparticles experience the energy dependence of the diffusion coefficient. Therefore the resistance change should vanish at both low and high temperatures and have a minimum for quasiparticle energies $\varepsilon \approx \mathcal{D}/L^2$.

As in the previous section, we will first calculate this effect for the one dimensional structure of Fig. 6.2 (a) and then extend the treatment to more general structures, using the geometry of Fig. 6.2 (b) as an example. The normal lead is now situated at $x = 0$ and the superconducting one at $x = L$. The procedure is as follows: We first integrate the diffusion equation for f_T twice, which gives $f_T(x, \varepsilon) = a(\varepsilon) \int_0^x D^{-1}(x', \varepsilon) dx' + b(\varepsilon)$. The integration constants may still depend on ε and are determined by the boundary conditions $f_T(0, \varepsilon) = \frac{eV}{2T} \cosh^{-2}(\frac{\varepsilon}{2T})$ and $f_T(L, \varepsilon) = 0$. This gives

$$f_T(x, \varepsilon) = \frac{eV}{2T} \cosh^{-2}\left(\frac{\varepsilon}{2T}\right) \left(1 - \frac{m(x, \varepsilon)}{m(L, \varepsilon)}\right) \tag{6.47}$$

with

$$m(x, \varepsilon) = \frac{1}{L} \int_0^x D^{-1}(x', \varepsilon) dx'. \tag{6.48}$$

As before, the current flowing out of the normal contact is proportional to $f_T'(0, \varepsilon)$ and hence we obtain for the normalized conductance $\frac{G}{G_N}$:

$$
\begin{aligned}
\frac{G}{G_N} &= \frac{1}{2\mathcal{D}T} \int_0^\infty d\varepsilon \, m^{-1}(L, \varepsilon) \cosh^{-2}\left(\frac{\varepsilon}{2T}\right) \\
&= \frac{\xi^2}{2L^2\mathcal{D}} \int_0^\infty d\tilde{\varepsilon} \, m^{-1}(L, \varepsilon) \cosh^{-2}\left(\frac{\tilde{\varepsilon}\xi^2}{2L^2}\right),
\end{aligned} \tag{6.49}
$$

where we have used $T = \mathcal{D}/\xi^2$ and scaled the energy with the Thouless energy $\tilde{\varepsilon} = \varepsilon L^2/\mathcal{D}$. Note that the $\cosh^{-2}(\frac{\varepsilon}{2T})$ part of the integrand defines the energy interval in which the quasiparticles feel the energy dependence of $m^{-1}(L, \varepsilon)$, as mentioned above. Eq. (6.49) shows that the normalized conductance depends on the ratio $L/\xi \sim \sqrt{T}$ only (the factor $[\mathcal{D}m(L, \varepsilon)]^{-1}$ is dimensionless and does not depend on temperature). In Fig. 6.7 the temperature dependence of the normalized resistance, $\frac{R}{R_N} = \frac{G_N}{G}$, is plotted. As expected, the effect vanishes at $T = 0$ and for $T \to \infty$. The maximum magnitude of the temperature effect is material independent and in general larger than that of the interaction effect; 10% vs. 5.5% for the particular case of a silver wire. Although the high temperature tail like the one of Fig. 6.7 was already observed in Ref. [15], the low temperature reentrant behavior of the resistance had, until recently [30], not yet been measured.

6.6.2 TEMPERATURE EFFECT IN ANDREEV INTERFEROMETERS

A generalization of this theory to more complicated structures should take into account how a resistance measurement is actually done. In the case of the experiment of Ref. [15]
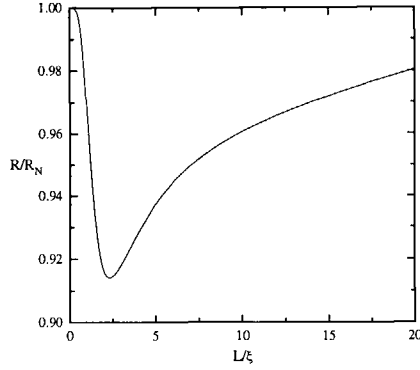
Figure 6.7: *Temperature dependence of the normalized resistance of the structure shown in Fig. 6.2 (a). The temperature is proportional to $(L/\xi)^2$.*

a current was applied between N_1 and N_2 whereupon the voltage between N_3 and N_4 was measured (see Fig. 6.2). As a consequence, there is no current in branch II nor in its mirror image attached to reservoir N_4. To calculate the resistance of this complex structure we proceed as follows: We start by noting that the current is conserved for each quasiparticle energy ε. This implies that $\mathcal{I}_I(\varepsilon) + \mathcal{I}_{II}(\varepsilon) = \mathcal{I}_{III}(\varepsilon)$. We now apply standard circuit theory for every quasiparticle energy (we use the fact that due to the antisymmetry of the voltage distribution the voltage is zero in the middle of the structure):

$$\mathcal{V}_1(\varepsilon) = \mathcal{I}_I(\varepsilon)\mathcal{R}_I(\varepsilon) + \mathcal{I}_{III}(\varepsilon)\mathcal{R}_{III}(\varepsilon), \qquad (6.50)$$

$$\mathcal{V}_3(\varepsilon) = \mathcal{I}_{II}(\varepsilon)\mathcal{R}_{II}(\varepsilon) + \mathcal{I}_{III}(\varepsilon)\mathcal{R}_{III}(\varepsilon), \qquad (6.51)$$

where $\mathcal{V}_i(\varepsilon) = \frac{V_i}{2T}\cosh^{-2}(\frac{\varepsilon}{2T})$ and the indices on $\mathcal{V}$ refer to the respective reservoirs and the indices on $\mathcal{I}$ and $\mathcal{R}$ refer to the appropriate branches. The proportionality constants $\mathcal{R}_{I,II,III}(\varepsilon)$ in the different branches can be deduced from the 'resistance' of the branches connecting two reservoirs:

$$\mathcal{R}_{ij}(\varepsilon) = \frac{f_i(\varepsilon) - f_j(\varepsilon)}{f_i'(\varepsilon) - f_j'(\varepsilon)}, \qquad (6.52)$$

where i and j label the reservoirs at which the distribution functions are evaluated.

Using the current conservation condition, Eq. (6.50) can be cast into the form of a matrix equation $\vec{\mathcal{V}}(\varepsilon) = \mathcal{R}(\varepsilon)\vec{\mathcal{I}}(\varepsilon)$, where $\mathcal{R}(\varepsilon)$ is a (2×2) matrix relating the voltage and current vectors $\vec{\mathcal{V}}(\varepsilon) = (\mathcal{V}_1(\varepsilon), \mathcal{V}_3(\varepsilon))^{\mathrm{T}}$ and $\vec{\mathcal{I}}(\varepsilon) = (\mathcal{I}_I(\varepsilon), \mathcal{I}_{II}(\varepsilon))^{\mathrm{T}}$. Inverting the matrix equation and integrating over all energies gives $\vec{I} = G\vec{V}$, where $\vec{V} = (V_1, V_3)^{\mathrm{T}}$, $\vec{I} = (I_I, I_{II})^{\mathrm{T}}$, and G is the conductance matrix which is given by $G = \frac{1}{2T}\int_0^\infty d\varepsilon \mathcal{R}^{-1}(\varepsilon)\cosh^{-2}(\frac{\varepsilon}{2T})$. We now impose the boundary condition mentioned above on the currents in branches I and II: $\vec{I} = (I, 0)^T$. This gives a relation between V_1 and V_3 in terms of the matrix elements of G; $V_1 = -\frac{G_{22}}{G_{21}}V_3$, which in turn must be used to calculate the experimentally measured resistance of the structure: $R = \frac{2V_3}{I} = 2(G_{12} - \frac{G_{11}G_{22}}{G_{21}})^{-1}$. The resistance depends again on the phase difference between the two superconducting reservoirs because of the boundary conditions imposed on the Green function.

In Fig. 6.8 we have plotted the results of this calculation for the previously used geometry of Fig. 6.2 (b) with $L_I = L_{II} = L_{IV} = L$ and $L_{III} = 2L$. This particular calculation was done for the value of $L/\xi = 3$ which gave the biggest effect. Also shown are the experimental results of Ref. [15].
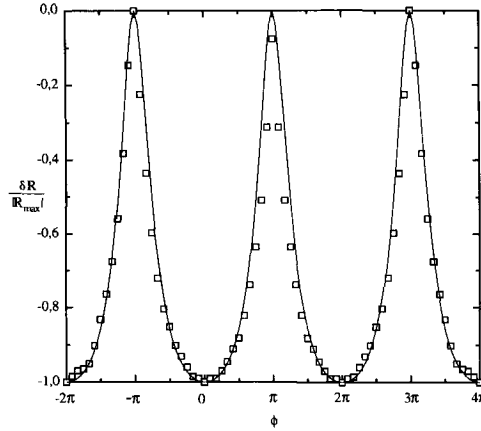

Figure 6.8: *Scaled resistance change due to the thermal effect of the structure shown in Fig. 6.2 (b) with $L_I = L_{II} = L_{IV} = L$ and $L_{III} = 2L$ for $L/\xi = 3$. The magnitude of the effect is 9.7%. The squares are the experimental data of Ref. [15].*

Again we find 2π periodic oscillations like in Fig. 6.6, but although the phase dependence looks similar there are some distinct differences. First of all the shape of the oscillations is different, especially near the minima, where the thermal effect produces less narrow peaks than the interaction effect. The amplitude of the thermal oscillations is material independent whereas that of Fig. 6.6 is proportional to the interaction parameter of the metal. Moreover, the maximal magnitude of the oscillations, 9.7% in this particular case, are in general much larger in the thermal effect, which makes observation of the previously discussed oscillations more difficult.

We obtain an excellent fit with the experimental data in Fig. 6.8, where the magnitude of the oscillations is about 11%. However, a decisive check on our theory would be provided by the observation of the temperature dependence of the resistance like the one plotted Fig. 6.7 for the system considered here. Indeed, unpublished data by the authors of Ref. [15] also show a remarkable agreement [29] with our calculations [17]. Moreover, very recently the observation of this reentrant behaviour has been claimed by an independent experimental group [30].

6.7 SUMMARY

We have performed calculations of the distribution of the electrostatic and nonequilibrium chemical potential in a one dimensional disordered superconducting hybrid wire. We showed

that the two behave differently as a function of temperature and that they are in fact only equal in the high temperature limit. We have proposed an experimental setup to measure these different potential distributions. We have also presented a computation for this wire using a recently developed [17] mechanism, that causes the resistance of a diffusive superconducting hybrid structure to change at zero temperature. The latter is in contrast with the well known thermal mechanism of Andreev reflection in diffusive metals, where the resistance change vanishes for low temperatures. In addition to this new result we have given a detailed account of the calculation performed in Ref. [17] for the experimental setup of Ref. [15]. Since the relative resistance change due to the novel mechanism is proportional to the interaction parameter in the normal metal, observation of this effect would allow a direct measurement of this physical quantity. Furthermore, we have shown how to calculate the resistance of an arbitrary Andreev interferometer using finite-temperature proximity effect theory. Because the finite temperature effect generally causes a much larger resistance change, this is the correct theory to describe an experiment like the one performed in Ref. [15].

REFERENCES

[1] A. F. Andreev, Sov. Phys. JETP **19**, 1228 (1964); **24**, 1019 (1967).

[2] G. E. Blonder, M. Tinkham, and T.M. Klapwijk, Phys. Rev. B **25**, 1415 (1982).

[3] C. J. Lambert, J. Phys.: Condens. Matter, **3**, 6579 (1991).

[4] C. W. J. Beenakker, Phys. Rev. B **46**, 12841 (1992).

[5] H. Nakano and H. Takayanagi, Sol. St. Comm. **80**, 997 (1991).

[6] F. W. J. Hekking and Yu. V. Nazarov, Phys. Rev. Lett. **71**, 1625 (1993).

[7] A. V. Zaitsev, Phys. Lett. A **194**, 315 (1994).

[8] A. Kadigrobov, A. Zagoskin, R. I. Shekhter, and M. Jonson, Phys. Rev. B **52**, 8662 (1995).

[9] N. K. Allsopp, J. Sanchez Canizares, R. Raimondi, and C. J. Lambert, J. Phys.: Condens. Matter **8**, L377 (1996).

[10] Yu. V. Nazarov, Phys. Rev. Lett. **73**, 1420 (1994).

[11] A. Volkov, N. Allsopp, and C. J. Lambert, J. Phys.: Condens. Matter **8**, L45 (1996).

[12] P. G. N. de Vegvar, T. A. Fulton, W. H. Mallison, and R. E. Miller, Phys. Rev. Lett. **73**, 1416 (1994).

[13] H. Pothier, S. Guéron, D. Estève, and M. H. Devoret, Phys. Rev. Lett. **73**, 2488 (1994).

[14] A. Dimoulas, J. P. Heida, B. J. van Wees, T. M. Klapwijk, W. v.d. Graaf, and G. Borghs, Phys. Rev. Lett. **74**, 602 (1995).

[15] V. T. Petrashov, V. N. Antonov, P. Delsing and T. Claeson, Phys. Rev. Lett. **74**, 5268 (1995).

[16] S. N. Artemenko, A. F. Volkov, and A. V. Zaitsev, Sol. St. Comm. **30**, 771 (1979).

[17] Yu. V. Nazarov and T. H. Stoof, Phys. Rev. Lett. **76**, 823 (1996).

[18] B. Z. Spivak and D. E. Khmelnitskii, JETP Lett. **35**, 412 (1982) [Pis'ma Zh. Eksp. Teor. Fiz. **35**, 334 (1982)].

[19] B. L. Altshuler, D. E. Khmelnitskii, and B. Z. Spivak, Sol. St. Comm. **48**, 841 (1983).

[20] F. Zhou, B. Spivak, and A. Zyuzin, Phys. Rev. B **52**, 4467 (1995).

[21] L. V. Keldysh, Sov. Phys. JETP **20**, 1018 (1964) [Zh. Eksp. Teor. Fiz. **47**, 1515 (1964)].

[22] A. I. Larkin and Yu. V. Ovchinnikov, Sov. Phys. JETP **41**, 960 (1975) [Zh. Eksp. Teor. Fiz. **68**, 1915 (1975)]; Sov. Phys. JETP **46**, 155 (1977) [Zh. Eksp. Teor. Fiz. **73**, 299 (1977)].

[23] A. Schmid, in *Nonequilibrium Superconductivity, Phonons and Kapitza Boundaries* Proceedings of the NATO Advanced Study Institute, Acquafredda di Marathea, Italy (1980).

[24] J. Rammer and H. Smith, Rev. Mod. Phys. **58**, 323 (1986).

[25] A. A. Abrikosov, L. P. Gorkov, and I. E. Dzyaloshinski, *Methods of Quantum Field Theory in Statistical Physics*, Dover, New York, (1963).

[26] K. D. Usadel, Phys. Rev. Lett. **25**, 507 (1970).

[27] A. F. Volkov, A. V. Zaitsev, and T. M. Klapwijk, Physica C **210**, 21 (1993).

[28] A. C. Mota, P. Visani, and A. Pollini, Journ. of Low Temp. Phys. **76**, 465 (1989).

[29] P. Delsing, private communication.

[30] H. Courtois, private communication.

7

FLUX EFFECT IN SUPERCONDUCTING HYBRID AHARONOV-BOHM RINGS

T. H. Stoof and Yu. V. Nazarov

We have extended the circuit theory of Andreev conductance [Phys. Rev. Lett. **73**, 1420 (1994)] to diffusive superconducting hybrid structures that contain an Aharonov-Bohm ring. The electrostatic potential distribution in the system is predicted to be flux-dependent with a period of the superconducting flux quantum $\Phi_0 = h/2e$. When at least one tunnel barrier is present, the conductance of the system oscillates with the same period.

unaltered but now apply to the transformed š and a fifth rule is needed to prescribe the boundary condition in the ring:

(v) Going around once in an Aharonov-Bohm ring, the spectral vector at the end of the loop is rotated by an angle 2χ around the z-axis with respect to the spectral vector at the beginning of the loop. The same holds for the spectral current.

We now have all the necessary ingredients to calculate the conductance of the structures depicted in Fig. 7.1. Network (a) consists of two diffusive wires that connect a normal and
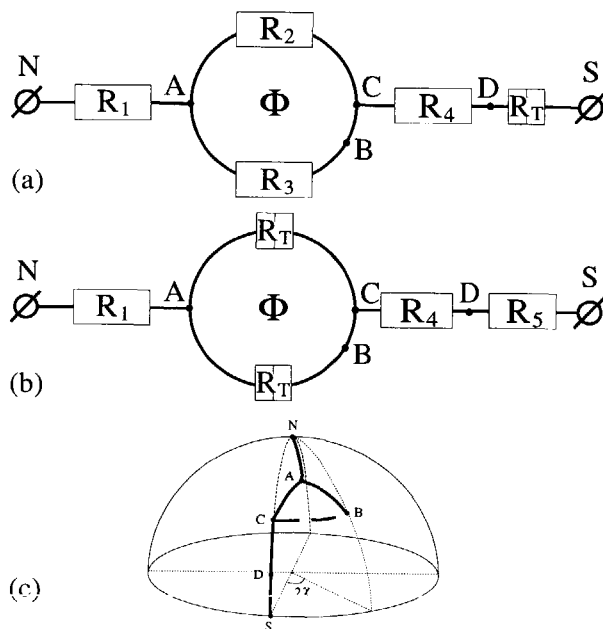

Figure 7.1: *(a) and (b) The networks under consideration. R_T is a tunnel junction and all other elements are diffusive resistors. (c) The circuits mapped onto a hemisphere.*

a superconducting terminal to a diffusive Aharonov-Bohm ring. Since a natural place for a tunnel barrier is at the N-S interface, we also included it in the circuit. Fig. 7.1 (b) shows a SQUID-like device, consisting of a ring with a tunnel junction in each branch that is connected to the reservoirs by two diffusive wires. We consider here a geometry with a single superconducting terminal only because we want study the effects caused by the applied flux rather than those due to Andreev interference. In Fig. 7.1 (c) we have mapped the circuits onto a hemisphere to indicate the position of the spectral vectors. Because only one superconducting terminal is present, its macroscopic phase is arbitrary and we choose it to be zero. As can be seen from this picture we have chosen the point B in the ring as the point where the spectral vector and current are discontinuous, indicated schematically by the dashed line.

Since the spectral vectors $\mathbf{s}_B$ and $\mathbf{s}_C$ are related by Eq. (7.4), we need only compute the positions of the points A, C and D, which are determined by spectral current conservation in the nodes (rule (iv)):

$$\sum_A \mathbf{I} \;=\; \mathbf{s}_A \times \left(\mathbf{s}_N \frac{C_{AN}}{R_1} + \mathbf{s}_C \frac{C_{AC}}{R_2} + \mathbf{s}_B \frac{C_{AB}}{R_3} \right) = \mathbf{0}, \tag{7.5}$$

$$\sum_C \mathbf{I} \;=\; \mathbf{s}_C \times \left(\mathbf{s}_A \frac{C_{CA}}{R_2} + \mathbf{s}_D \frac{C_{CD}}{R_4} \right) + \mathbf{I}_{BC} = \mathbf{0}, \tag{7.6}$$

$$\sum_D \mathbf{I} \;=\; \mathbf{s}_D \times \left(\mathbf{s}_C \frac{C_{DC}}{R_4} + \frac{\mathbf{s}_S}{R_T} \right) = \mathbf{0}, \tag{7.7}$$

where $C_{IJ} = \arccos(\mathbf{s}_I \mathbf{s}_J)/\sqrt{1 - (\mathbf{s}_I \mathbf{s}_J)^2}$ and the current $\mathbf{I}_{BC} = \Omega \, (\mathbf{s}_B \times \mathbf{s}_A) \, C_{BA}/R_3$, where Ω is a matrix that rotates the spectral current over an angle -2χ according to rule (v). The physical current, however, is conserved in every node because a uniform rotation of the spectral current leaves the physical current invariant. Note that the spectral current leaving point A is not equal to the spectral current arriving in C. This is a consequence of the gauge transformation we have used. Knowing the spectral vectors in the three points we are able to compute the resistance of the structure:

$$R_{\text{tot}} = R_1 + \frac{R_2 R_3}{R_2 + R_3} + R_4 + \frac{R_T}{\cos \alpha_{DS}}, \tag{7.8}$$

where $\cos \alpha_{DS} = \mathbf{s}_D \mathbf{s}_S$ is the renormalization factor for tunnel conductivities according to rule (i).

Let us now first turn to a discussion of what we call the electro-flux effect. Consider the geometry of Fig. 7.1 (a) without the tunnel junction. In this case the total resistance of the network is not affected by the applied flux since the resistance of diffusive elements is not renormalized. However, the electrostatic potential distribution in the structure is still flux-dependent. To see this we look at the zero-temperature expression for the electrostatic potential [13]:

$$\varphi(x, \Phi) = \frac{1}{4e} \text{Tr} \, \hat{G}^K = \zeta(x) \cos \theta(x, \Phi), \tag{7.9}$$

where $\hat{G}^K$ is the Keldysh component of the Green function and $\zeta(x)$ is the quasiparticle distribution function that measures the deviation from equilibrium [3]. At zero temperature, $\zeta(x)$ is a linear function of position and its slope is proportional to the voltage drop across a resistive element. The factor $\cos \theta(x, \Phi)$ in (7.9) is just the z-component of the spectral vector, which at zero temperature is equal to the quasiparticle density of states. From the fact that Eq. (7.9) involves the flux-dependent $\theta(x, \Phi)$ it is obvious that also the electrostatic potential will depend on the flux through the ring.

Fig. 7.2 shows this electro-flux effect at different points in the structure. Here we have considered a structure with a total length of $3L$ and the wires have lengths NA = AC = CS = L. Fig. 7.2 clearly shows that the electro-flux effect is largest in the middle of the structure and vanishes in the end points of the structure. This new effect is reminiscent of the electrostatic Aharonov-Bohm effect, in which the phase of an electron in a ring is influenced by an applied transverse electric field [14]. However, in a sense the electrostatic Aharonov-Bohm effect is just the opposite of the electro-flux effect because in the latter case
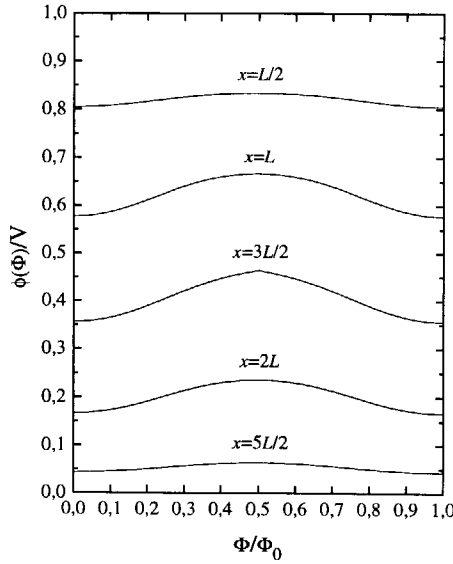
Figure 7.2: *Electrostatic potential as a function of flux for different points along the structure. Calculated for $R_1 = R_4 = R$ and $R_2 = R_3 = 2R$.*

the electrostatic potential in the ring is modified by changing the phase of the quasiparticles with a magnetic field. Using a SET-transistor it should in principle be possible to measure the local electrostatic potential in a given point. One could then measure the change in potential as a function of the applied flux. For a more detailed description of such an experiment see Ref. [7].

In the last part of this chapter we discuss the flux-dependent conductance of several circuits that may be experimentally relevant. In Fig. 7.3 we have plotted the conductance of three different systems as a function of the applied flux for different values of the resistances in the circuit. The conductance has been normalized to its zero-flux value. Panels (a) and (b) show the results for the system of Fig. 7.1 (a). In panel (a) $R_1 = R_2 = R_3 = R_4 = R$ and in panel (b) $R_2 = R_3 = R_4 = R$ and $R_1 = R_T$. The different curves correspond to different values of R_T/R. Fig. 7.3 (c) shows the case in which the diffusive resistor R_1 and the tunnel barrier R_T in Fig. 7.1 (a) have been interchanged and the remaining panel shows the conductance of the SQUID-like device of Fig. 7.1 (b) with $R_4 = R_5 = R$ and $R_1 = R_T$.

Let us first consider the circuit of Fig. 7.1 (a). The panels (a) and (b) show that, in this case, applying a flux through the ring decreases the conductance. This is easily understood with the aid of Fig. 7.1 (c). When a flux is applied, all points A, C and D are 'pulled' towards the north pole of the hemisphere, thus increasing the angle α_{DS} between the spectral vectors $\mathbf{s}_D$ and $\mathbf{s}_S$. Eq. (7.8) then shows that this increases the resistance relative to the zero-flux value.

It is also clear that an increase of the resistance of both the tunnel junction R_T and the interface resistance R_1 causes a bigger effect on the conductance. This because in case (a) point D is much closer to the north pole of the structure than in case (b), where it is
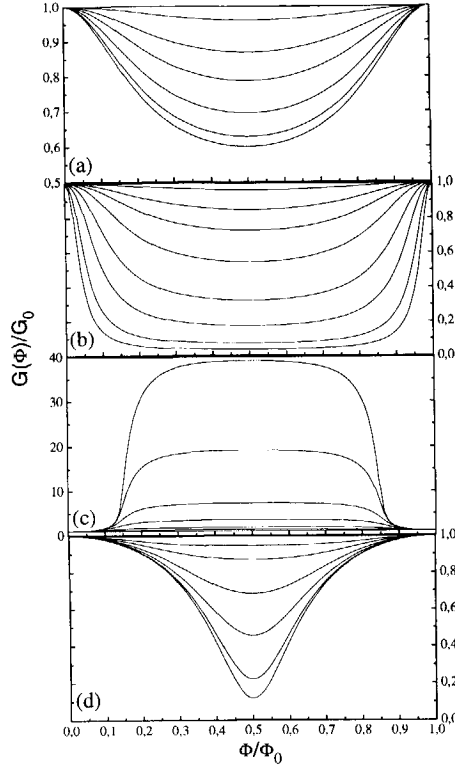
Figure 7.3: *Normalized conductance versus applied flux. Panels (a) and (b) correspond to the structure of Fig. 7.1 (a), panel (c) to the same circuit with R_1 and R_T interchanged and (d) to the SQUID-like device of Fig. 7.1 (b). From small to large amplitude the different curves correspond to: (a) $R_T/R = 1, 2, 3, 5, 10, 100$; (b) $R_T/R = 1, 2, 3, 5, 10, 20, 100$; (c) $R_T/R = 1, 3, 5, 10, 20, 50, 100$; (d) $R_T/R = 3, 5, 10, 20, 50, 100$.*

somewhere in the middle between N and S. Applying a flux will have a much larger effect on the renormalization factor $\cos \alpha_{DS}$ in case (b) than in case (a). Whereas the maximal reduction in conductance in case (a) is less than a factor of 2, it is almost a factor of 30 in case (b). In the limit of large R_1 and R_T our results agree with those obtained in Ref. [2].

Although Fig. 7.3 (a) and (b) might give the impression that the conductance always decreases when a flux is present, this is not generally the case. It is also possible to increase it, e.g. in systems with a single tunnel barrier between the normal contact and the ring. When all diffusive resistors are kept constant and only the tunnel resistance is varied, the conductance is increased dramatically. As shown in Fig. 7.3 (c) the maximum increase is a factor of 40 for a tunnel barrier that has a 100 times bigger resistance than the diffusive resistors in the network.

In the SQUID-like structure of Fig. 7.1 (b), the results are qualitatively the same as

those shown in Fig. 7.3 (b). Similar considerations as the ones used above show that the conductance reduction is largest when both the resistance R_1 and the tunnel resistances in the ring are large. There is, however, a striking difference in shape of the curves. Whereas in panel 7.3 (b) the minimum becomes broader on increasing the resistances, the opposite is occurring in panel 7.3 (d) where a sharp peak develops. The characteristic shapes of the curves displayed in Fig. 7.3 should be observable experimentally. The flux induced by the current in the loop can be shown to be proportional to the small parameter $(\xi_\Delta/L)^2$, where $\xi_\Delta = \sqrt{D/\Delta}$ is the superconducting coherence length, and we therefore disregarded this contribution.

In conclusion, we have generalized the circuit theory of Andreev conductance of Ref. [3] to networks that include an Aharonov-Bohm ring penetrated by a magnetic flux. We have given the complete set of altered circuit-theory rules and used them to calculate the flux-dependent resistance of several experimentally relevant structures. Under the right conditions these devices are very sensitive to the applied flux. We have predicted an electro-flux effect in these circuits, which entails that the electrostatic potential distribution in the structure can be altered by varying the applied magnetic flux through the ring. It should be possible to observe this effect experimentally.

References

[1] See e.g. H. Nakano and H. Takayanagi, Sol. St. Comm. **80**, 997 (1991); A. V. Zaitsev, Phys. Lett. A **194**, 315 (1994); A. Kadigrobov *et al.* Phys. Rev. B **52**, 8662 (1995).

[2] F. W. J. Hekking and Yu. V. Nazarov, Phys. Rev. Lett. **71**, 1625 (1993)

[3] Yu. V. Nazarov, Phys. Rev. Lett. **73**, 1420 (1994).

[4] P. G. N. de Vegvar *et al.*, Phys. Rev. Lett. **73**, 1416 (1994); H. Pothier *et al.*, Phys. Rev. Lett. **73**, 2488 (1994); A. Dimoulas *et al.* Phys. Rev. Lett. **74**, 602 (1995); V. T. Petrashov et al, Phys. Rev. Lett. **74**, 5268 (1995).

[5] A. F. Andreev, Sov. Phys. JETP **19**, 1228 (1964); **24**, 1019 (1967).

[6] Yu. V. Nazarov and T. H. Stoof, Phys. Rev. Lett. **76**, 823 (1996).

[7] T. H. Stoof and Yu. V. Nazarov, Phys. Rev. B. **53**, 14496 (1996).

[8] A. F. Volkov, A. V. Zaitsev, and T. M. Klapwijk, Physica C **210**, 21 (1993).

[9] B. Z. Spivak and D. E. Khmelnitskii, JETP Lett. **35**, 412 (1982) [Pis'ma Zh. Eksp. Teor. Fiz. **35**, 334 (1982)]; B. L. Altshuler, D. E. Khmelnitskii, and B. Z. Spivak, Sol. St. Comm. **48**, 841 (1983).

[10] V. T. Petrashov *et al.*, Phys. Rev. Lett. **70**, 347 (1993); V. T. Petrashov *et al.*, JETP Lett. **60**, 606 (1994) [Pis'ma Zh. Eksp. Teor. Fiz. **60**, 589 (1994)]. H. Courtois *et al.*, Phys. Rev. Lett. **76**, 130 (1996). S. G. den Hartog *et al.*, preprint.

[11] L. V. Keldysh, Sov. Phys. JETP **20**, 1018 (1964) [Zh. Eksp. Teor. Fiz. **47**, 1515 (1964)].

[12] A. I. Larkin and Yu. V. Ovchinnikov, Sov. Phys. JETP **41**, 960 (1975) [Zh. Eksp. Teor. Fiz. **68**, 1915 (1975)]; Sov. Phys. JETP **46**, 155 (1977) [Zh. Eksp. Teor. Fiz. **73**, 299 (1977)].

[13] F. Zhou, B. Spivak, and A. Zyuzin, Phys. Rev. B **52**, 4467 (1995); See also Ref. [7] and references therein.

[14] T. H. Boyer, Phys. Rev. D **8**, 1679 (1973); S. Datta *et al.*, Appl. Phys. Lett. **48**, 487 (1986); S. Washburn *et al.*, Phys. Rev. Lett. **59**, 1791 (1987).

SUMMARY

This thesis deals with the theoretical investigation of electrical transport properties of several mesoscopic systems. It is possible to discern two regions of interest. The first part of the thesis is concerned with the physics of semiconductor structures. In particular, we study edge channels in wide quantum wires of the two-dimensional electron gas in the integer quantum Hall regime and time-dependent transport in a double quantum dot. The second part of the thesis is devoted to normal metal-superconducting hybrid systems in the diffusive regime. Each topic is introduced briefly in the first chapter.

Chapter two deals with the ground state properties of semiconductor quantum dots and wires in a quantizing magnetic field. Using density-functional theory in high magnetic fields we are able to take into account both the direct Coulomb and exchange interaction in the two-dimensional electron gas (2DEG). A simple numerical scheme is devised in which exchange is included in a local density approximation. We calculate the ground state electron density distribution for both wires and dots as a function of the confinement potential. We show that exchange plays a significant role in reducing the width of the compressible regions that are obtained from a purely electrostatic calculation. The transition from the incompressible edge channels of the Hartree-Fock picture to the broad, compressible strips predicted by electrostatics occurs within a narrow but experimentally accessible range of confinement strengths. In addition, we use our numerical scheme to study the effect of a back gate on the density distribution and find that exchange becomes increasingly important when the gate gets close to the 2DEG. We proceed to calculate the addition energy of a quantum dot as a function of magnetic field and compare them with previously performed self-consistent Hartree calculations. We find that both the amplitude and period of the Coulomb blockade oscillations are increased by the exchange interaction.

In chapter three we discuss transport properties of a double-quantum dot system in the presence of electromagnetic irradiation. For a large bias voltage, the current through the system is calculated as a function of the applied gate voltage. Using a density-matrix formulation, the photoresponse of the system is shown to exhibit extra resonant peaks when the frequency of the applied irradiation matches the renormalized energy difference between the two discrete resonant states. If the irradiation amplitude is increased, the height of this satellite peak becomes of the order of the main peak. However, its width remains much smaller. For small inter-dot tunneling and large irradiation amplitude, extra satellite peaks appear in a pattern that is very similar to that in Josephson junctions subject to a time-dependent bias voltage.

In chapter four we once again consider a double quantum dot, but this time in the absence of a bias voltage. By applying electromagnetic radiation it is, under certain circumstances, possible to use the system as an electron pump. Depending on the energies of the intermediate states of a pumping cycle, it is possible to transport electrons through the system both incoherently and coherently. For both cases we derive the equations of motion for the density matrix elements and calculate the resonant current through the system as a function of the applied radiation frequency.

The three remaining chapters of this thesis are concerned with nonequilibrium meso-scopic superconductivity in the diffusive regime. Chapter five describes a new Andreev interferometer that is based on the pair potential induced in the normal metal region by electron-electron interaction. As a result of this induced pair potential, quasiparticles undergo Andreev reflection throughout the entire structure, before they interfere. A measurement of this effect would allow a direct determination of the interaction parameter in the normal metal. Moreover, a recent experiment is described in terms of the classic proximity-effect theory, thereby explaining the experimental results as a thermal effect.

Using the quasiclassical Green-function approach, a detailed description is given of both the thermal and interaction mechanisms for Andreev interferometers of arbitrary geometry in chapter six. In addition, we discuss in detail the difference between the electrostatic and chemical potential distribution in these hybrid structures. In general, both potentials differ appreciably and only coincide in the high temperature limit. We finally propose an experiment to measure the difference between the two potentials.

In the final chapter we extend Nazarov's circuit theory of Andreev conductance by including Aharonov-Bohm rings into the network. We calculate flux-dependent resistances of several different devices. The electostatic potential in an Aharonov-Bohm ring is predicted to be flux-dependent, even for a completely diffusive device without tunnel junctions.

SAMENVATTING

Dit proefschrift beschrijft theoretisch onderzoek naar de elektrische transporteigenschappen van een aantal mesoscopische systemen. De interesse ging hierbij uit naar twee verschillende onderzoeksgebieden. Het eerste deel van het proefschrift houdt zich bezig met de fysica van halfgeleiderstructuren. We bestuderen hierin randkanalen in brede quantumdraden van een tweedimensionaal elektrongas dat zich in het integrale quantumhallregime bevindt alsmede tijdsafhankelijk transport in een dubbele quantumdot. Het tweede deel is gewijd aan hybride structuren van normale metalen en supergeleiders in de diffuse limiet. In het eerste hoofdstuk worden bovenstaande onderwerpen kort geïntroduceerd.

Hoofdstuk twee behandelt de grondtoestandseigenschappen van halfgeleider quantumdots en -draden in een zeer hoog magneetveld. Gebruikmakend van dichtheidsfunktionaaltheorie in hoge magneetvelden kunnen we zowel de direkte Coulomb- als de exchangewisselwerking in het tweedimensionale elektrongas (2DEG) in rekening te brengen. Een eenvoudige numerieke methode wordt ontwikkeld waarin de exchangewisselwerking in een lokale dichtheidsbenadering wordt verdisconteerd. We berekenen de elektronendichtheidsverdeling van draden en dots in de grondtoestand als funktie van de opsluitpotentiaal en laten zien dat de exchangewisselwerking een belangrijke rol speelt in het versmallen van de compressibele gebieden die zijn verkregen uit een zuiver elektrostatische berekening. Bovendien voorspellen we dat de overgang van de incompressibele randkanalen uit de Hartree-Fockbeschrijving naar de brede, compressibele gebieden zoals die worden voorspeld door de elektrostatica, optreedt in een nauw, maar experimenteel toegankelijk gebied van opsluitingssterkten. Verder gebruiken we onze numerieke methode om de invloed van een evenwijdige gate op de dichtheidsverdeling te bestuderen. Het blijkt dat het belang van de exchangewisselwerking toeneemt indien de gate zich dichter bij het 2DEG bevindt. Tenslotte wordt de additieenergie van een quantumdot als funktie van het magneetveld berekend en vergeleken met al eerder uitgevoerde zelfconsistente Hartreeberekeningen. Zowel de amplitude als de periode van de Coulombblokkadeoscillaties nemen toe als gevolg van de exchangewisselwerking.

Hoofdstuk drie bespreekt de transporteigenschappen van een dubbele quantumdot in aanwezigheid van elektromagnetische straling. Voor het geval van een grote spanning over het systeem wordt de stroom door de dots als funktie van de aangelegde gatespanning berekend. Gebruikmakend van een dichtheidsmatrixbeschrijving laten we zien dat de fotorespons van het syteem extra resonante pieken vertoont wanneer de frequentie van de gebruikte straling overeenkomt met het gerenormeerde energieverschil tussen de twee discrete, resonante toestanden. Wanneer het stralingsvermogen toeneemt, wordt de hoogte van de satelietpiek van de orde van de hoofdpiek, terwijl zijn breedte veel kleiner blijft. In het geval van kleine interdottunneling en groot stralingsvermogen verschijnen er extra satelietpieken, analoog aan die in een Josephsonjunctie waarover een tijdsafhankelijke spanning wordt aangelegd.

In hoofdstuk vier beschouwen we wederom een dubbele quantumdot, maar nu in de afwezigheid van een spanning over het systeem. Onder bepaalde omstandigheden is het mogelijk om door middel van electromagnetische straling de dubbele dot als elektronenpomp te laten fungeren. Afhankelijk van de energieen van de toestanden die worden doorlopen

in een pompcyclus, is het mogelijk om elektronen zowel incoherent als coherent door het systeem te transporteren. Voor beide gevallen leiden we de bewegingsvergelijkingen voor de dichtheidsmatrixelementen af en berekenen we de resonante stroom door het systeem als functie van de aangelegde stralingsfrequentie.

De overige drie hoofdstukken in dit proefschrift houden zich bezig met mesoscopische non-equilibriumsupergeleiding in de diffuse limiet. Hoofdstuk vijf beschrijft een nieuw soort Andreevinterferometer die is gebaseerd op de door elektron-elektronwisselwerking geïnduceerde paarpotentiaal in het normale metaal. Ten gevolge van deze paarpotentiaal Andreevreflecteren quasideeltjes in de gehele struktuur voordat ze interfereren. Een meting van dit effect zou een directe bepaling van de interactieparameter van het normale metaal mogelijk maken. Verder wordt een recent experiment beschreven in het kader van de nabij-heidseffecttheorie. De experimentele resultaten worden verklaard als een temperatuureffect.

Gebruikmakend van quasiklassieke Greense funkties, wordt in hoofdstuk zes een beschrij-ving gegeven van zowel het temperatuurs- als het wisselwerkingsmechanisme voor Andreev-interferometers met een arbitraire geometrie. We bespreken in detail het verschil tussen de elektrostatische en -chemische potentiaalverdeling in deze hybride strukturen. In het alge-meen verschillen beide potentialen nogal en vallen ze alleen samen bij hoge temperaturen. Tenslotte beschrijven we een experiment waarmee het verschil tussen beide potentialen zou kunnen worden aangetoond.

In het laatste hoofdstuk breiden we Nazarov's netwerktheorie voor Andreevgeleiding uit door Aharonov-Bohmringen in het circuit op te nemen. We berekenen hiermee fluxafhanke-lijke weerstanden van een aantal verschillende netwerken. De elektrostatische potentiaal in een Aharonov-Bohmring is fluxafhankelijk, zelfs voor het geval van een diffuse struktuur zonder tunneljuncties.

CURRICULUM VITAE

Theo Stoof

24-02-1970	Geboren te Eindhoven.
1980-1988	Atheneum B aan het Sint Joriscollege te Eindhoven.

1988-1993 Studie Natuurkunde aan de Technische Universiteit Eindhoven.
- Experimentele stage in de vakgroep Lage Temperaturen.
  Onderwerp: *Elektronen op vloeibaar helium.*
- Theoretische stage in de vakgroep Theoretische Natuurkunde.
  Onderwerp: *Gebonden toestanden in halfgeleider heterostructuren.*
- Afstudeeropdracht in de vakgroep Theoretische Natuurkunde.
  Onderwerp: *GW berekening van de bandgap in silicium.*

1993-1997 Promotieonderzoek aan de Technische Universiteit Delft in de
vakgroep Theoretische Natuurkunde van prof. G. E. W. Bauer.
  Onderwerp: *Transport van wisselwerkende elektronen in*
              mesoscopische systemen.

Aug. 1997- In dienst van Unisource Business Networks te Den Haag.

LIST OF PUBLICATIONS

1 *Dielectric theory of the stopping power of fast ions in crystals*
   T. M. H. E. Tielens, G. E. W. Bauer, and T. H. Stoof
   Physical Review B **49**, 5741 (1994), Rapid Communication

2 *The influence of exchange on edge states in the integer quantum Hall regime*
   T. H. Stoof and G. E. W. Bauer
   in *High Magnetic Fields in the Physics of Semiconductors*, edited by D. Heiman,
   World Scientific, Singapore (1995)

3 *Density-functional theory of quantum wires and dots in a strong magnetic field*
   T. H. Stoof and G. E. W. Bauer
   Physical Review B **52**, 12143 (1995)

4 *Density-functional theory of quantum dots in the high magnetic field limit*
   T. H. Stoof and G. E. W. Bauer
   Solid State Electronics **40**, 349 (1996)

5 *Time-dependent resonant tunneling via two discrete states*
   T. H. Stoof and Yu. V. Nazarov
   Physical Review B **53**, 1050 (1996)

6 *Diffusive conductors as Andreev interferometers*
   Yu. V. Nazarov and T. H. Stoof
   Physical Review Letters **76**, 823 (1996)

7 *Kinetic equation approach to diffusive superconducting hybrid devices*
   T. H. Stoof and Yu. V. Nazarov
   Physical Review B **53**, 14496 (1996)

8 *Flux effect in superconducting hybrid Aharonov-Bohm rings*
   T. H. Stoof and Yu. V. Nazarov
   Physical Review B **54**, 772 (1996), Rapid Communication

9 *Andreev interference in diffusive conductors*
   T. H. Stoof and Yu. V. Nazarov
   in *Correlated Fermions and Transport in Mesoscopic Systems*, edited by T. Martin,
   G. Montambaux and J. Trân Thanh Vân, Editions Frontières, Gif-sur-Yvette Cedex,
   France (1996)

10 *A coherent double-quantum-dot electron pump*
   T. H. Stoof and Yu. V. Nazarov
   Submitted to Physical Review Letters